Study of Photovoltaic Effect in Lead-free Ferroelectric Perovskite Oxides

TING HO FUNG

MPhil
The Hong Kong Polytechnic University
2019

The Hong Kong Polytechnic University

Department of Applied Physics

Study of Photovoltaic Effect in Lead-free Ferroelectric Perovskite Oxides

TING Ho Fung

A thesis submitted in partial fulfillment of the requirements

for the degree of Master of Philosophy

August 2017

Certificate of Originality

I hereby declare that this thesis is my own work and that, to the best of my knowledge and belief, it reproduces no material previously published or written, nor material that has been accepted for the award of any other degree or diploma, except where due acknowledgement has been made in the text.

____________________ (Signature)

Ting Ho Fung (Name of candidate)

Abstract

$K_{0.5}Na_{0.5}NbO_3$ (KNN) ceramics and KNN ceramics doped with 0.25 mol% MnO_2 (KNN-Mn) or 1 mol% CuO (KNN-Cu) have successfully been fabricated by a solid-state reaction method. All the samples are well densified into an orthorhombic perovskite structure. MnO_2 and CuO act as sintering aids for enhancing the densification. CuO can also reduce the sintering temperature by 50°C. The grain size of the KNN ceramic is 1.4 μm on average, whereas the grain sizes of the KNN-Mn and KNN-Cu ceramics are reduced by 0.4 μm on average. The optical properties of the ceramics have been studied based on their transmittance and diffuse reflectance spectra, and their bandgaps have been estimated by Tauc's relation. Our results show that the bandgap of the KNN-Mn ceramic is slightly larger than that of the KNN ceramic. This should be attributed to the increase in the electronegativity difference between the B-site ions and oxygen arisen from the partial substitution of Mn3+ for Nb5+. Probably owing to the ineffective substitution of Cu2+ for the B-site Nb5+, the KNN-Cu ceramic exhibits a similar bandgap with KNN. The effects of the measurement methods, transmission or diffuse reflection, on the estimation of bandgap have been studied. It has been found that the bandgaps estimated by the transmission method are dependent on the sample thickness. Owing to the stepper change in transmittance, the estimated bandgap for thinner samples are larger. Moreover, the bandgaps estimated by the transmission method are generally lower than those obtained from the diffuse reflection method. The direct bandgaps of KNN and KNN-Mn estimated using the transmittance spectra are 3.16 eV and 3.21 eV, respectively, while their indirect bandgaps are 3.14 eV and 3.19 eV, respectively. On the other hand, the direct bandgaps of KNN, KNN-Mn and KNN-Cu estimated using the diffuse reflectance spectra are 3.34 eV, 3.41 eV and 3.35 eV, respectively, and their indirect bandgaps are 3.13 eV, 3.22 eV and 3.26 eV, respectively. The differences between the bandgaps estimated from the transmittance and diffuse reflectance spectra have been discussed based on their theoretical assumptions.

The ferroelectric photovoltaic properties of the samples have been studied. It has been shown that the direction of the short-circuit current is opposite to the net polarization or the poling field, while no short-circuit current is observed in unpoled samples under illumination. Also, the higher the poling field, the larger the net polarization, and then the stronger the depolarization field is. As a result, the observed I_{sc} increases with the poling field because of the higher efficiency in separating and drifting the opposite charges. It is suggested that the driving force of the short-circuit current is attributed to the net polarization. As confirmed by a controlled experiment, the short-circuit current is originated from the photo-excited electron-hole pairs. It is note that the observed I_{sc} increases rapidly to a maximum value once the sample is illuminated, but it decreases gradually with time and becomes saturated afterwards. The variations of the observed I_{sc} is confirmed not contributing by the thermal effect. The repeatability of the observed I_{sc} has also been evaluated. The observed I_{sc} exhibits similar variations with time in each cycle that consists of 20-min illumination and 40-min darkness, but decreases slightly in the consecutive cycles. However, after keeping the sample short-circuited and in the dark for a long time (e.g., 85 hours), the I_{sc} increases and reaches almost the same maximum level as in the first illumination cycle, suggesting that the reduction in I_{sc} is reversible. Charged carriers may temporarily be trapped at the sample-electrode interfaces during the illumination, and the release of the trapped charges is a very slow process that requires a long period (85 hours) to complete.

The photocurrent responses of the KNN-Mn and KNN-Cu ceramics have also been studied. Similar to KNN, the observed I_{sc} for both the ceramic samples exhibit similar variations with time. However, their maximum values are much lower than that of KNN, only about 30%. It is interesting to note that, despite the difference in the maximum level they reached at the beginning of illumination, they all saturate at almost the same level. The greater I_{sc} observed in KNN may due to its higher defect density. Charges may temporarily be trapped in the defects when the sample is stored short-circuited and in the dark. Under the illumination, the trapped charges are excited and released slowly, and thus contributing to the observed I_{sc}. After the release of most of the trapped charges, the I_{sc} becomes saturated and reaches a level similar to those for KNN-Mn and KNN-Cu. As all the ceramics have similar bandgaps, the saturated I_{sc} should then reflect to the photovoltaic effect. More investigation is needed to further understand the phenomenon.

Acknowledgement

First, I would like to give a big thank to my chief supervisor, Prof. K. W. Kwok for his endless support and valuable advice during my research study. I have learnt so much that it facilitates my career after my study.

I would also like to thank for the technical support provided by the Materials Research Centre (MRC).

Last but not least, I appreciate the advices, inspiration and support from my colleagues and friends, and the understanding from my family.

Table of Contents

List of Figure

List of Table

Chapter 1 Introduction

1.1 Motivation and Objective of Research

Since the discoveries of piezoelectric effect by J. and P. Curie in 1880[1] and ferroelectricity by J. Valasek in 1920[2], various types of ferroelectric materials have been widely studied and used in different applications, such as ferroelectric memories [3, 4], transducers [5]and actuators [6]. Most of the applications adopt the piezoelectric effect and the ferroelectric properties of ferroelectric materials. There are relatively few researches or applications focused on the photovoltaic effect of ferroelectric perovskite oxides, although it have been already over half a century since the first discovery of photovoltaic effect in ferroelectric perovskite oxides [7]. Researchers have not paid attentions on the ferroelectric photovoltaic effect mainly because of its low photocurrent output, i.e. short-circuit current, and low photo-electric power conversion efficiency. The mechanism of ferroelectric photovoltaic effect is intrinsically different from that of other photovoltaic effect, e.g. the photovoltaic effect of p-n junction in semiconductor. The higher-than-bandgap open-circuit voltage and the switchable short-circuit current in ferroelectric perovskite oxides are the most attractive aspects and make it distinct from other photovoltaic materials, which will be introduced in latter chapter.

In recent years, many countries, such as UK, Canada and China, have enacted more stringent carbon emission restrictions [8-10]. Using clean energy is one of the ways to reduce carbon emission. However, it is still too pricey for the commercialized silicon solar energy comparing with fossil energy [11]. These two factors provide incentives for researchers to extensively investigate and study a new generation of solar cells over the past decade. Ferroelectric perovskite oxides have been considered as one of the potential candidates of new-generation solar cells because of their low-cost fabrication and the potential of exceeding the power conversion efficiency limit of silicon-based solar cells due to their larger-than-bandgap output voltage [12].

Among the researches on ferroelectric perovskite oxides, lead-based perovskite oxides have been widely studied because of their relatively high photoelectric conversion efficiency and large remnant polarization [13-19]. However, there is over 60 wt% lead contained in lead-based ferroelectric perovskite oxides. It is highly volatile during high-temperature sintering and thus causes severe environmental pollution. In 2014, the Waste Electrical and Equipment Directive (WEEE) has been enacted for restricting the use of hazardous materials, including lead, in the manufacture of electronic devices [20]. So, investigating lead-free ferroelectric perovskite oxides is seemingly inevitable.

There are some potential candidates for lead-free ferroelectric perovskite oxides in ferroelectric photovoltaic applications, such as bismuth ferrite ($BiFeO_3$), bismuth sodium titanate ($Bi_{0.5}Na_{0.5}TiO_3$) and potassium sodium niobate ($K_{0.5}Na_{0.5}NbO_3$ or KNN). Attracted by the relatively low bandgap, bismuth ferrite has been extensively studied in recent years [21-23]. But researches have overlooked the others, which provide greater remnant polarization despite having larger bandgap [24-28].

Potassium sodium niobate has drawn the least attention and there are very few researches focused on its ferroelectric photovoltaic effect. Some studies have found that, after material engineering, KNN has superior properties and is comparable to the-state-of-art lead-based perovskite oxides[28]. Therefore, KNN may also be a good candidate that has potential to achieve good photovoltaic properties. In this study, the KNN-based perovskite oxides have been fabricated and their ferroelectric photovoltaic responses have been investigated with the use of interdigital transducer (IDT) electrodes.

1.2 Outline of Thesis

To demonstrate and study the ferroelectric photovoltaic effect in KNN-based perovskite oxides is the main objective of this thesis. The introduction is followed by the literature review in Chapter 2, which includes the fundamental knowledge of ferroelectricity, the comparison between the photovoltaic mechanisms in semiconductors and ferroelectric perovskite oxides and the-state-of-art researches on ferroelectric photovoltaic effect.

The detailed fabrication procedures of KNN-based perovskite oxides are described in Chapter 3, as well as the characterization of their dielectric, piezoelectric, ferroelectric and optical properties.

Chapter 4 reports the ferroelectric photovoltaic effect of KNN-based perovskite oxides. It provides a detailed device fabrication process, the experiment method, results and discussion.

Finally, Chapter 5 concludes the study of this thesis and proposes suggestions for future works.

CHAPTER 2 Literature Review

2.1 Introduction

Ferroelectric photovoltaic effect is distinct from the photovoltaic effect in semiconductor p-n junctions. Its unique mechanism allows ferroelectric perovskite oxides to generate an output voltage that is higher than its bandgap as well as a switchable current along the polarization direction when illuminated with photons of energy higher than its bandgap. In this Chapter, the ferroelectric photovoltaic effect will be introduced and compared with the photovoltaic effect in semiconductor p-n junction. Before that, the fundamental concept of ferroelectricity will be introduced, which is important for understanding the ferroelectric photovoltaic effect. Finally, the state-of-the-art researches will be reviewed for introducing the ongoing researches in the field of ferroelectric photovoltaic effect.

2.2 Ferroelectricity

Ferroelectricity, or ferroelectric effect, is the ability of a certain material of which the spontaneous polarization can be reoriented by applying an electric field higher than its coercive field (E_c) at temperature below its Curie temperature (T_C). The effect was discovered by J. Valasek in 1921 [2]. The ferroelectric properties can be evaluated via a hysteresis loop (or PE-loop) measurement. Ferroelectric materials, in most cases, have a perovskite structure [29]. It is noted that there are not many perovskites are ferroelectric [30]. In this chapter, we will discuss the ferroelectricity in perovskite oxides only for the sake of simplicity.

In the following sections, the perovskite structure will be first introduced with the concept of Curie Temperature. Domains and Domain walls will then be introduced and followed by the most important feature of ferroelectricity – hysteresis loop. Finally, the relations between dielectric, piezoelectric, pyroelectric and ferroelectric will be introduced.

2.2.1 Perovskite structures and Curie Temperature

Perovskite structure is commonly seen in ferroelectric materials such as barium titanate (BTO), potassium niobate (KNO), bismuth ferrite (BFO) and lead titanate (PTO). It is in the form of ABX_3, where A and B are the atoms at position (0, 0, 0) and position (1/2, 1/2, 1/2) of the unit cell, respectively, and X sit at position (1/2, 1/2, 0), (1/2, 0, 1/2) and (0, 1/2, 1/2) of the unit cell. A and B are usually positively charged ions, and X is oxygen for perovskite oxide [29, 31].

Perovskite structure can be in the form of cubic, tetragonal, orthorhombic or rhombohedral. The cubic form exists when the temperature is above the Curie temperature (T_C), while the other forms exist only when the temperature is below T_C [32]. The cubic structure, illustrated in Figure 2.1a, is centrosymmetric and does not produce any (spontaneous) polarization while the tetragonal, orthorhombic and rhombohedral structures produce spontaneous polarizations contributed by the off-centered B ions and off-set O ions. The tetragonal structure is illustrated as an example in figure 2.1b.

The B site ion in the perovskite structure always tends to sit at the lowest internal energy position. As illustrated in figure 2.1c, when $T > T_C$, there exists only one minimum state at the center of cubic. At lower temperatures ($T < T_C$), the energy profile distorts and two off-center minimum states occur, which correspond to the position below or above the tetragonal center as illustrated in figure 2.2d. The B site ion will be located at either one of the off-center minima when it is free of external influences, e.g. electric field and mechanical force. The A site ions will be distorted. The charges correspond to the A site ion, B site ion and O ion thus produce a spontaneous polarization. Reorienting the spontaneous polarization requires a sufficient energy to move the B site ion across the energy barrier to the opposite side [32, 33].

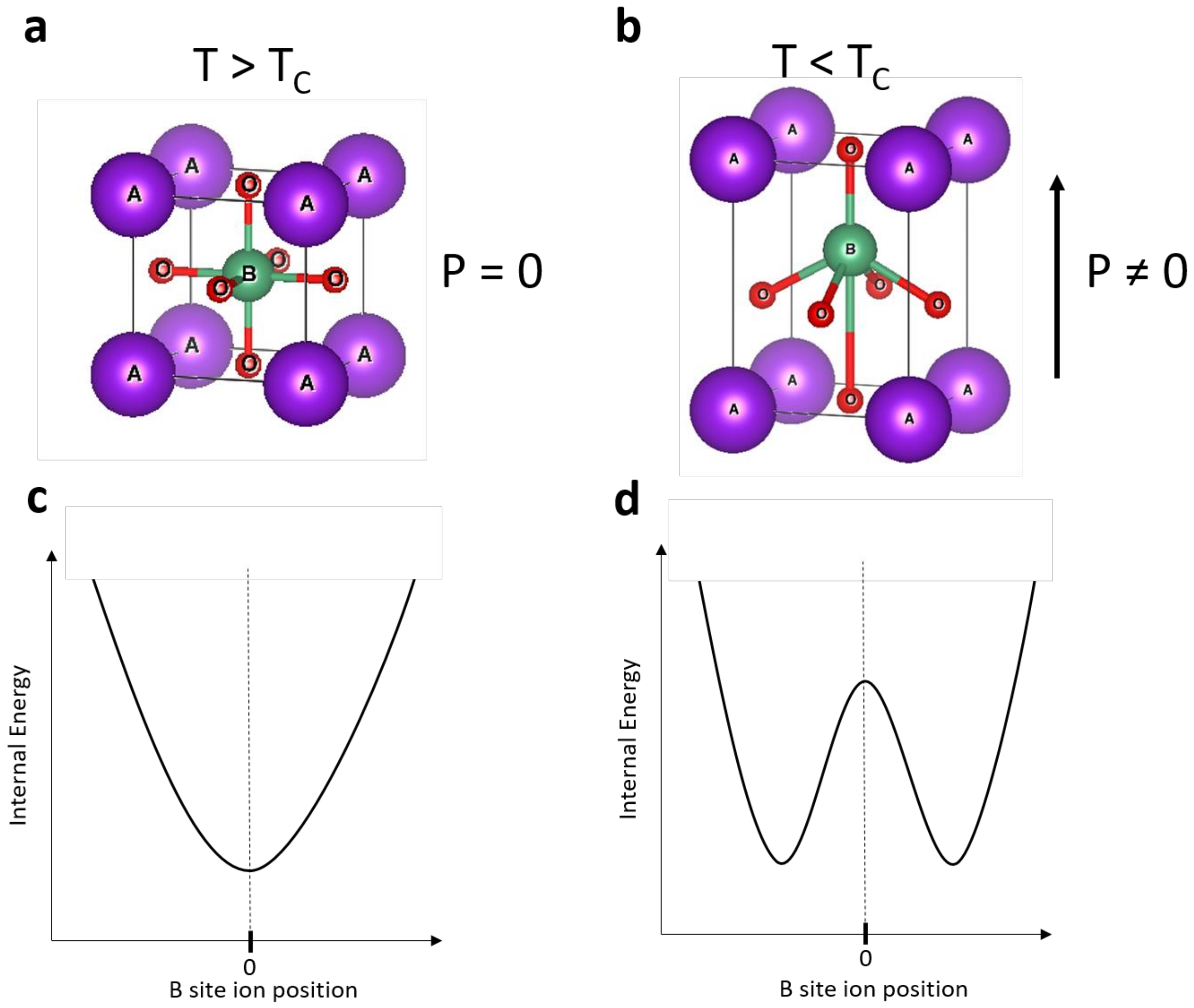

Figure 2.1 a) A typical perovskite structure in cubic phase with temperature higher than Curie Temperature, b) A perovskite structure in tetragonal phase exhibit an electric dipole due to its off-centered B-site atom at temperature lower than Curie Temperature, c) and d) the corresponding internal energy profile of cubic structure and tetragonal structure, respectively.

2.2.2 Domains and Domain Walls

A domain in ferroelectric ceramics or thin films is defined as a region in which all the spontaneous polarizations are oriented in the same direction. The regions between domains are defined as domain walls. The spontaneous polarization in a domain induces positive and negative surface charges on its head side and tail side. The electric field formed by the surface charges is defined as the depolarization field, E_{de}. The depolarization field can be strong and makes the formation of single-domain ferroelectric crystal impossible [29, 34]. By forming multiple and small domains, the depolarization field can be reduced and the material becomes energetically stable.

For example, in a tetragonal structure, there are two types of domain walls, 90° wall and 180° wall, as illustrated in figure 2.2. The walls separating two domains with their polarization oriented perpendicularly are 90° walls and those separating domains with polarizations oriented in the opposite directions are 180° walls. The depolarization field can be reduced by both 180° walls and 90° walls, while 90° walls may additionally reduce elastic energy [29].

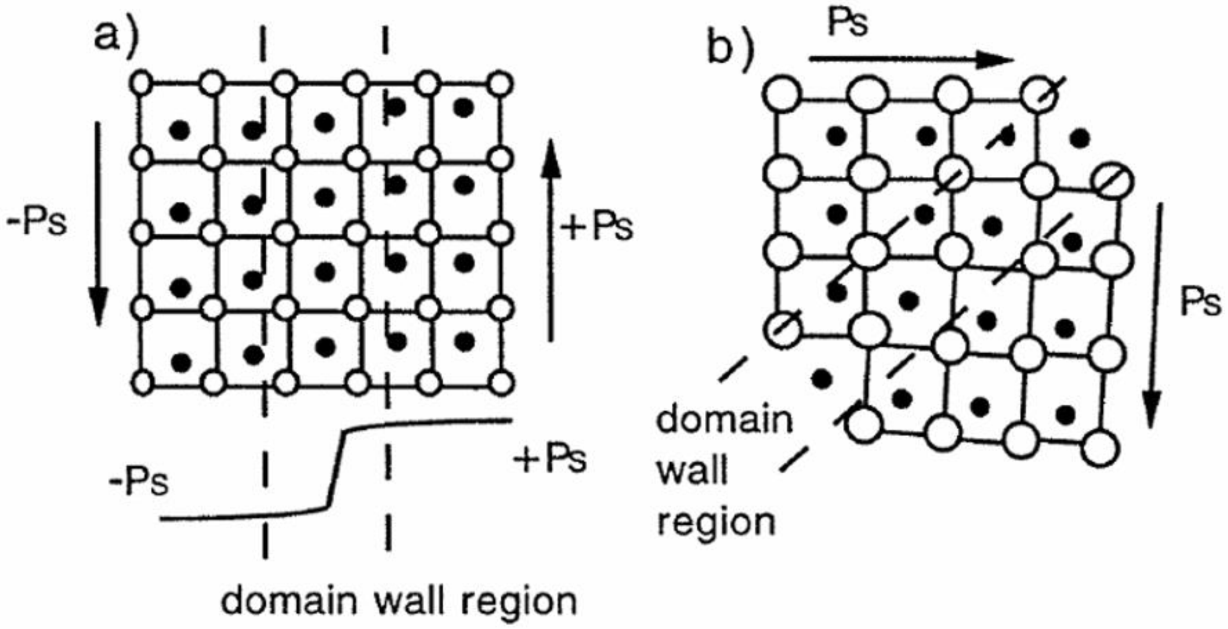

Figure 2.2 Two types of domain walls, a) 180° walls and b) 90° walls. The domain wall region is the area between two dashed line [29].

At temperatures above T_C, the perovskite is in cubic phase and the distance between the B site ion and its six neighboring O ions are equal. There are 6 possible directions for the B site ion to move, with equal probabilities, as the material is cooled through T_C. The domain formation is governed by electrical and mechanical constraints. Usually, the material is subjected to a combination of electrical and mechanical constraints in cooling through the T_C, and thus leading to a complex structure containing a combination of 180° walls and 90° walls. As illustrated in figure 2.3, when the perovskite cubic phase transforms to a tetragonal phase in cooling through T_C, 90° walls are created to reduce elastic energy whereas 180° walls are created to minimize the depolarization field [29].

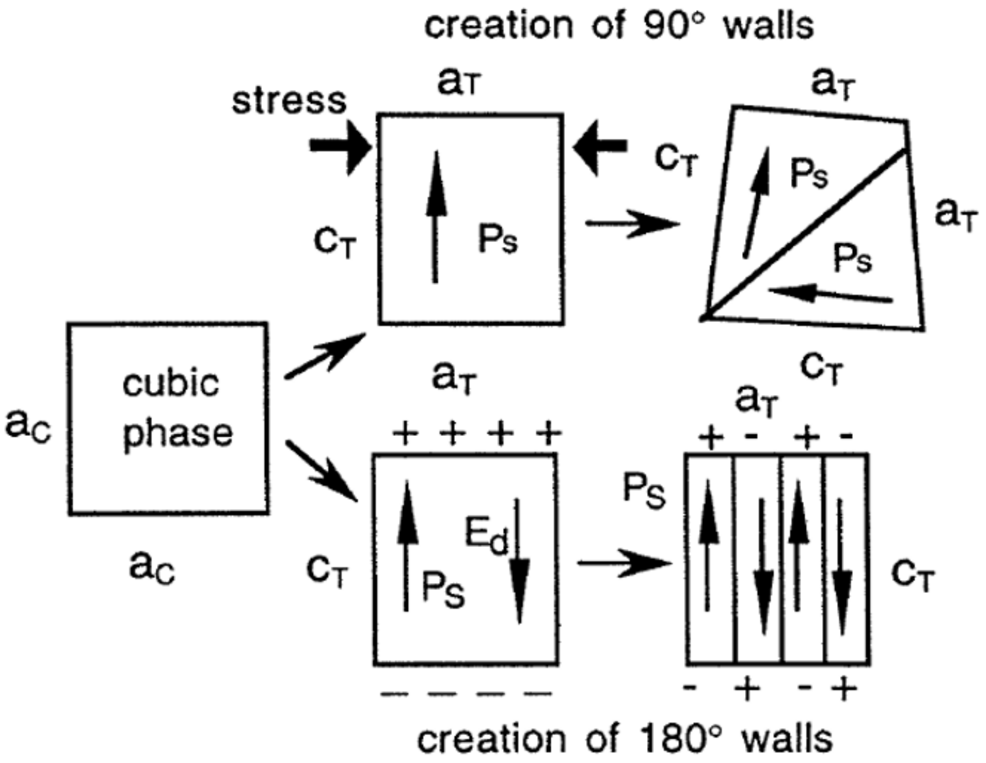

Figure 2.3 Formation of domain walls. The creation of 90° walls under mechanical constraints and the creation of 180° walls under electrical constraints as the cubic phase transforms to tetragonal phase while it is cooled through T_C [29].

2.2.3 Poling and Hysteresis Loop

In an as-prepared ferroelectric ceramic or film, the domains are usually randomly oriented and the bulk ceramic or film exhibits zero net polarization. Before utilizing the ferroelectric materials in various applications, it is essential to align the spontaneous polarization in each domain in the same direction to obtain their unique properties, e.g. piezoelectric and pyroelectric effect. The process of aligning the domains' polarizations coercively in one direction using a high external electric field is called poling. A net remnant polarization will be generated after poling [29]. Usually, the poling process is conducted at a temperature slightly below the Curie temperature to reduce the potential barrier for moving the B-site ion. The schematic diagram shown in figure 2.4 illustrates the poling process.

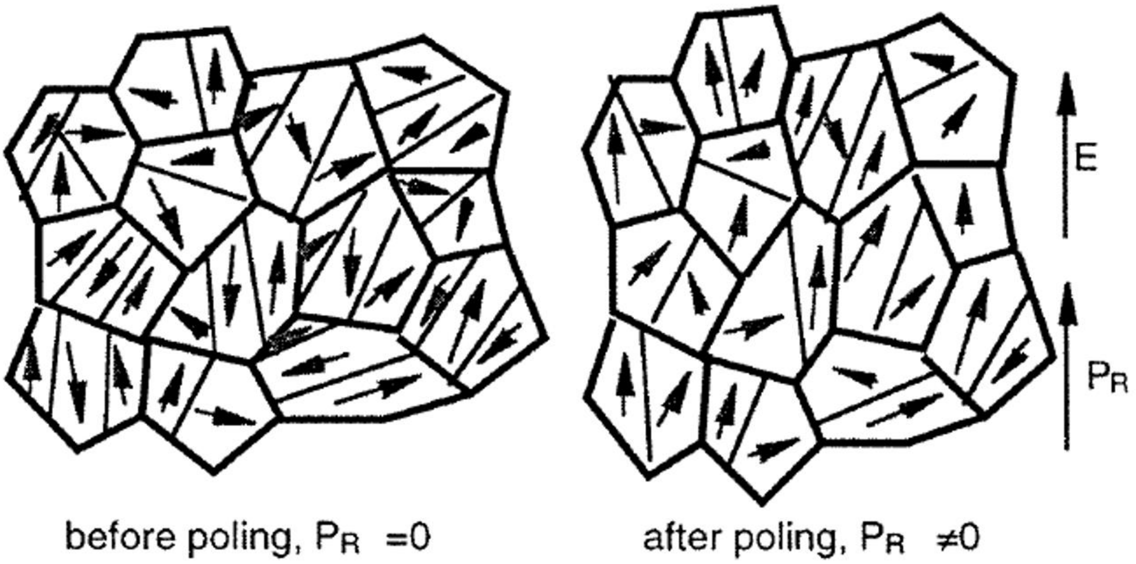

Figure 2.4 The domains are randomly oriented in a polycrystalline ferroelectric material before poling and it produces zero net remnant polarization. The domains are coercively aligned along the poling field. After poling, the material produces a net remnant polarization [29].

The ability of ferroelectric materials to switch the polarization under an external electric field can be evaluated from the hysteresis loop (or P-E loop), which is a loop describing the relation between the external electric field and net polarization of the material. The P-E loop can be experimentally observed by using the Sawyer–Tower circuit [35].

Figure 2.5 shows a typical hysteresis loop. At the start point A, the as-prepared ceramic contains randomly oriented domains and exhibits a zero net polarization. An AC electric field ($E = E_o\sin\omega t$) starts to apply on the ceramic. In the very beginning (i.e., the very first section of segment AB), E is small and not high enough to orient the polarizations in domains. The observed net polarization P is then mainly contributed by the dielectric polarization and increases linearly with E, following the typical relationship $P = \chi E$, where χ is the dielectric susceptibility of the material [29]. As E increases, the polarizations start to switch along the field direction, and thus contributing to the observed polarization. As a result, the observed P becomes increased nonlinearly with increasing E. At point B, all the domains are aligned along the poling field, giving a maximum P that is defined as the saturated polarization, P_S. As E decreases (i.e., from B to C), some, but not all, domains' polarizations relax, causing a decrease in the observed P. At point C or E = 0, the material exhibits a net (non-zero) polarization that is called the remnant polarization, P_r. As E continues to decrease and becomes negative, i.e., alter the direction, the domains are forced to switch to the opposite direction. As a result, the observed P decreases and reaches a zero value at point D. The amplitude of the electric field at this point is defined as the coercive field, E_C. At point E, all the domains are switched in opposite direction and the observed P reaches a minimum value or -Ps. Similarly, if E now increases, some domains relax and the observed P increases, giving a remanent polarization in opposite direction, i.e., $-P_r$, at point F [29, 36]. For an ideal hysteresis loop, the shape is rotational symmetric and $|E_C| = |-E_C|$ and $|P_r| = |-P_r|$.

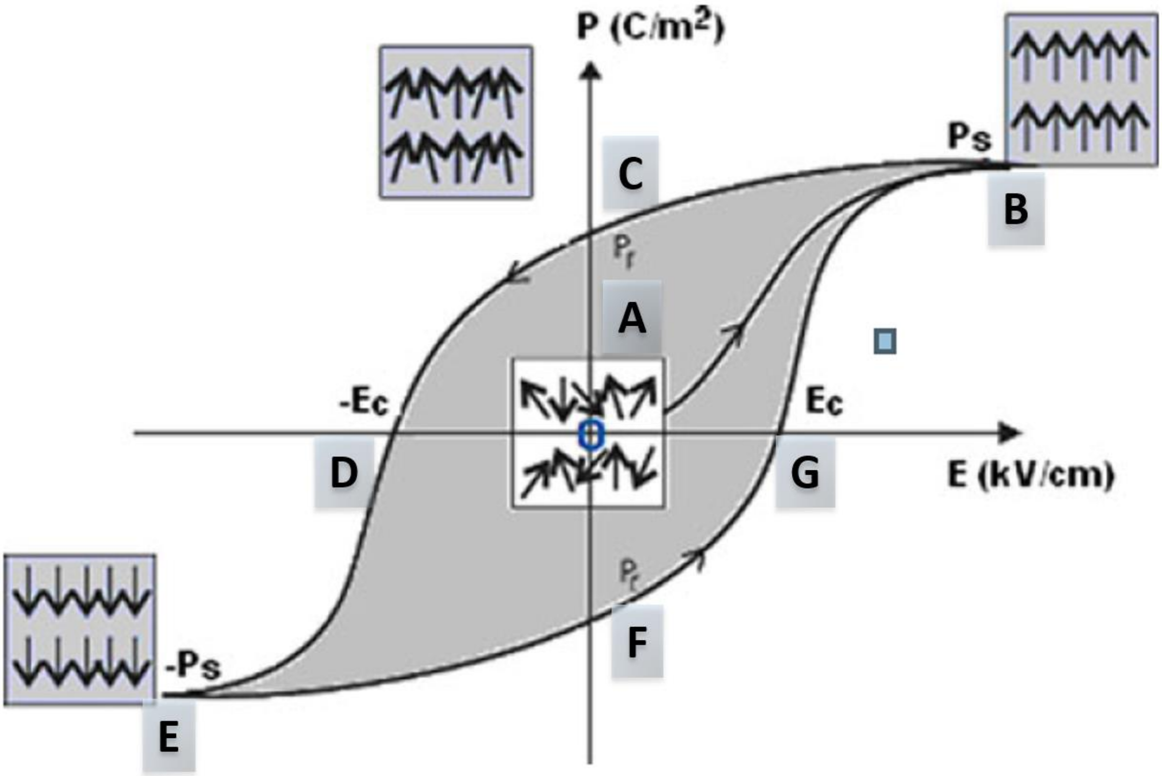

Figure 2.5 A typical hysteresis loop of a ferroelectric ceramic [36].

2.2.3 The relations between Dielectric, Piezoelectric, Pyroelectric and Ferroelectric

Ferroelectric materials (after poling) provide both piezoelectric and pyroelectric effects. However, piezoelectric materials may not be pyroelectric, and pyroelectric materials must be piezoelectric but may not be ferroelectric [37]. The Venn diagram shown in Figure 2.6 illustrates the relation between dielectric, piezoelectric, pyroelectric and ferroelectric.

In the following sections, piezoelectricity and pyroelectricity will be introduced.

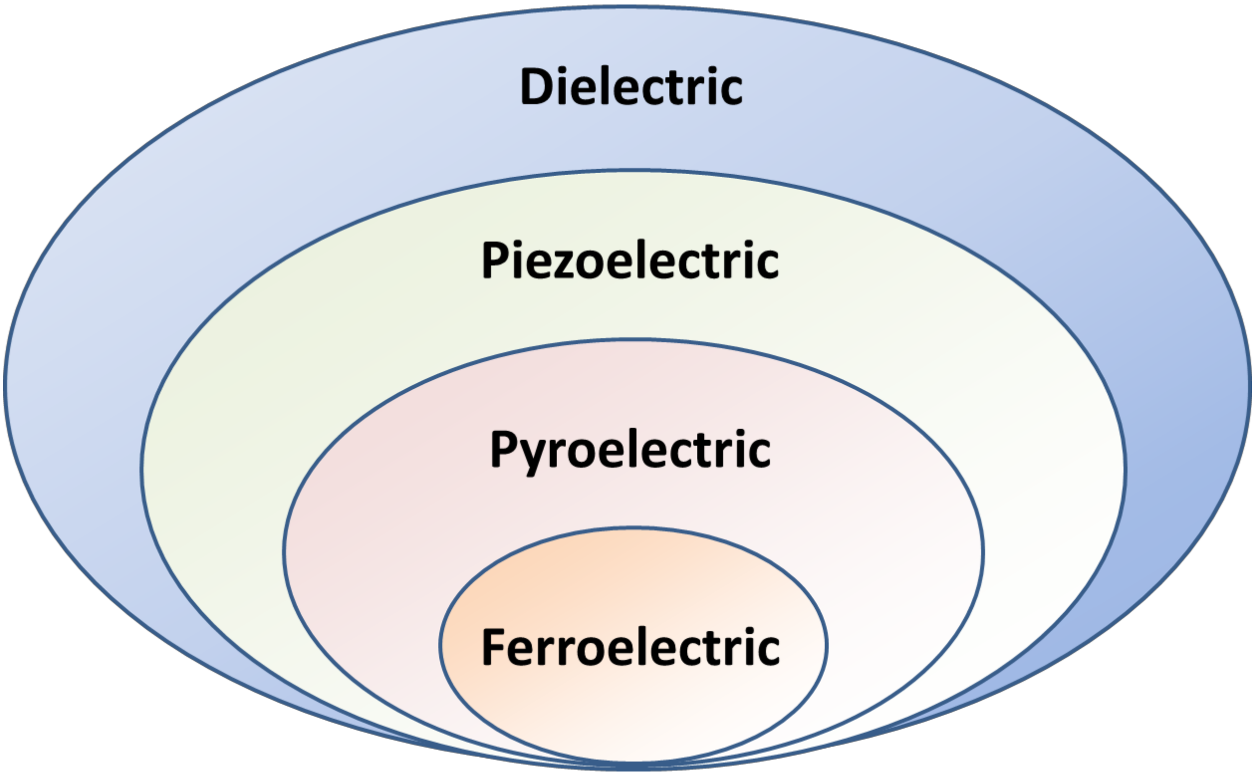

Figure 2.6 Venn diagram of the relations between Dielectric, Piezoelectric, Pyroelectric and Ferroelectric.

2.2.3.1 Piezoelectricity

Piezoelectricity, or piezoelectric effect, is the generation of electrical potential across a material when a mechanical stress is applied. On the contrary, the converse piezoelectric effect is the appearance of a physical deformation on a material when an electric field is applied [29].

The piezoelectric effect was first demonstrated by Paul-Jacques Curie and Pierre Curie in 1880. They demonstrated the effect on various crystals such as tourmaline, quartz, topaz, cane sugar, and Rochelle salt [1]. The converse piezoelectric effect was first theoretically deduced from thermodynamic principles by Gabriel Lippmann in 1881 [38]. Both the direct and converse piezoelectric effect are reversible.

A schematic explanation of piezoelectricity is shown in Figure 2. Figure 2a shows the piezoelectric material at a natural state. Figures 2b and 2c explain the relations between the output voltage and external force in the direct piezoelectric effect while figures 2d and 2e explain the relations between the applied voltage and induced forces in the converse piezoelectric effect.

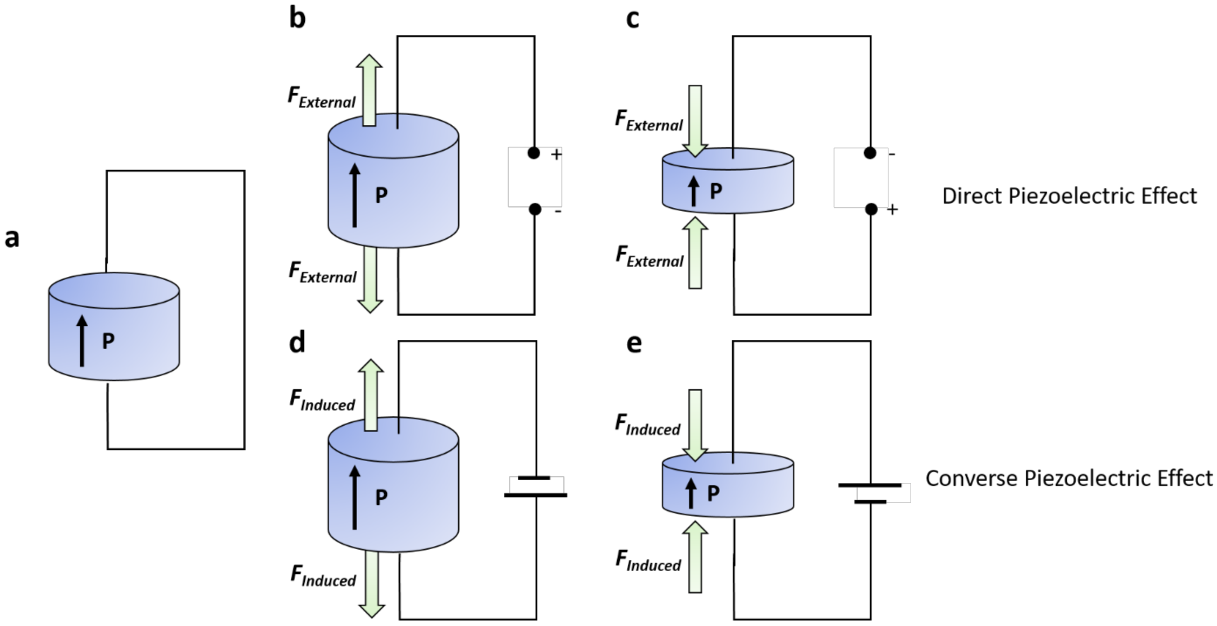

Figure 2.7 a) a piezoelectric material at natural state, temperature below Curie point, b) and c) Direct piezoelectric effect - Electric potentials induced by external compressive force or tensile force, d) and e) Converse piezoelectric effect – Forces induced by external voltages applied on material.

The direct and converse piezoelectric theoretical equations were developed by W. Voigh in 1910 [39],

$$S_{ij} = s_{ijkl}(E) \cdot T_{kl} + d_{mij} E_m \cdots\cdots (2.1)$$
$$D_i = d_{ikl} T_{kl} + \varepsilon_{ij}(T) \cdot E_j \cdots\cdots (2.2)$$

where S is the strain, s is the elastic compliance, T is the stress, d is the piezoelectric coefficient, E is the external electric field, D is the electric displacement, ε is the permittivity, i, j, k, l, m = 1, 2 and 3. Equation 2.1 describes the converse piezoelectric effect and equation 2.2 describes the direct one.

2.2.3.2 Pyroelectricity

Pyroelectricity, or pyroelectric effect, is the generation of an electrical potential across the material when it is heated or cooled.

The pyroelectric effect has a long history. The first discovery of the effect was in 314BC by Theophrastus [40]. The effect was named by Sir David Brewster in 1824 and the theory of it was developed by William Thomson and WoldemarVoigt [41-43].

In a polar material, the dielectric displacement equation can be expressed in

$D = \varepsilon E + P_S \cdots\cdots (2.3)$ (the format is different from eqn. 2.1 and 2.2 as well as 2.4)

where D is the dielectric displacement, ε is the permittivity, E is the electric field and P_S is the spontaneous polarization.

Equation 2.4 is the derivative of equation 2.3 with respect to the temperature,

$$p_i' = E_j \frac{\partial \varepsilon_{ij}}{\partial T} + \frac{\partial P_S}{\partial T} \ldots\ldots (2.4)$$

where $p_i' = \frac{\partial D_i}{\partial T}$ is defined as the pyroelectric coefficient[29].

2.3 Photovoltaic effect

Photovoltaic effect is the generation of free electrons and holes upon the absorption of light. The electrons and holes are driven by a built-in field and reach the electrodes for producing voltage or current [44]. The first demonstration of photovoltaic effect was conducted by Edmond Becquerel in 1839 using an electrochemical cell [45]. However, most of the photovoltaic cells used nowadays are solid-state materials due to their stabilities and promising performances.

In this section, the physics of photovoltaic effect will be introduced. First, the photovoltaic effect in semiconductors will be described and followed by that in ferroelectric materials. The mechanism, advantages and drawbacks will be discussed and compared. Finally, the state-of-the-art of researches in ferroelectric photovoltaic effect will be given.

2.3.1 Photovoltaic effect in semiconductor

2.3.1.1 Semiconductor

Semiconductor is a kind of materials of which the electrical properties are in between those of conductors and insulators. It can be classified using the concept of bandgap. Bandgap is defined as the energy required to excite an electron from its bounded state (valence band) to a free state (conduction band) in a material.

Figure 2.8 illustrates the band diagrams of these three kinds of materials. For conductors, the valence band is overlapped with the conduction band. There always exist free electrons in the conduction band so they are conducting. For insulators, the bandgap is very large, contributed by its ionic bonds [12]. High energy is required to excite electrons from the valence band to the conduction band. So, they are electrically insulated. For semiconductors, the bandgap is much lower than that of insulators, typically 1eV to 2eV. Owing to the low bandgap, there are fistful of electrons existed in the conduction band at temperatures above absolute zero due to thermal excitation.

The temperature dependences of the (electrical) conductivity for conductors and semiconductors are different. The conductivity of conductors (e.g. metals) decreases as the temperature increases due to lattice scattering [46]. However, for semiconductors, the conductivity increases with increasing temperature because more electrons are excited to the conduction band due to thermal excitation. Be noted that, at sufficiently high temperatures where significant amount of electrons are excited to the conduction band, the semiconductor will become a conductor and its conductivity will decrease with increasing temperature due to lattice scattering [47].

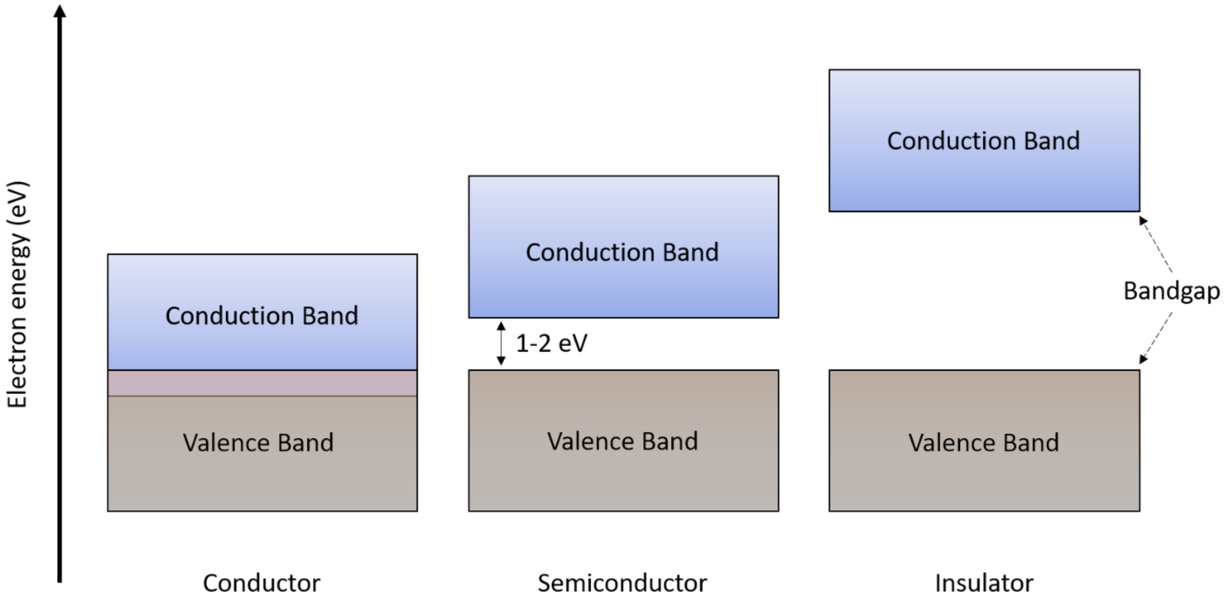

Figure 2.8 The band diagram of conductor, semiconductor and insulator

2.3.1.2 p-n junction

Most of the applications do not adopt the intrinsic semiconductor (or undoped semiconductor). In applications of energy harvesting, excited electrons cannot be obtained in an intrinsic semiconductor because of the lack of driving force. A p-n junction provides an internal electric field for driving the electrons and holes to the electrodes so that electricity can be harvested.

The electrical properties of semiconductors can be altered via doping. For example, the free electron concentration of silicon can be increased by doping elements in the fifth column of the periodic table (e.g. phosphorus) to make it become an n-type semiconductor. On the other hand, if elements in the third column of the periodic table (e.g. boron) are used as dopants, the hole concentration will be increased and the doped silicon will become an p-type semiconductor.

When an n-type and an p-type silicon are brought together, as driven by the electron concentration gradient, the free electrons in the n-type region will diffuse into the p-type region, leaving positive ions in the n-type region. Space charges are then built up at the interface and a depletion region is formed. Figure 2.9 illustrates the formation of a depletion region at the p-n junction. The built-in electric field by the space charges repels the electrons from further diffusion. At the equilibrium state, a potential difference V_{bi}, is created across the depletion region [44, 48-50].

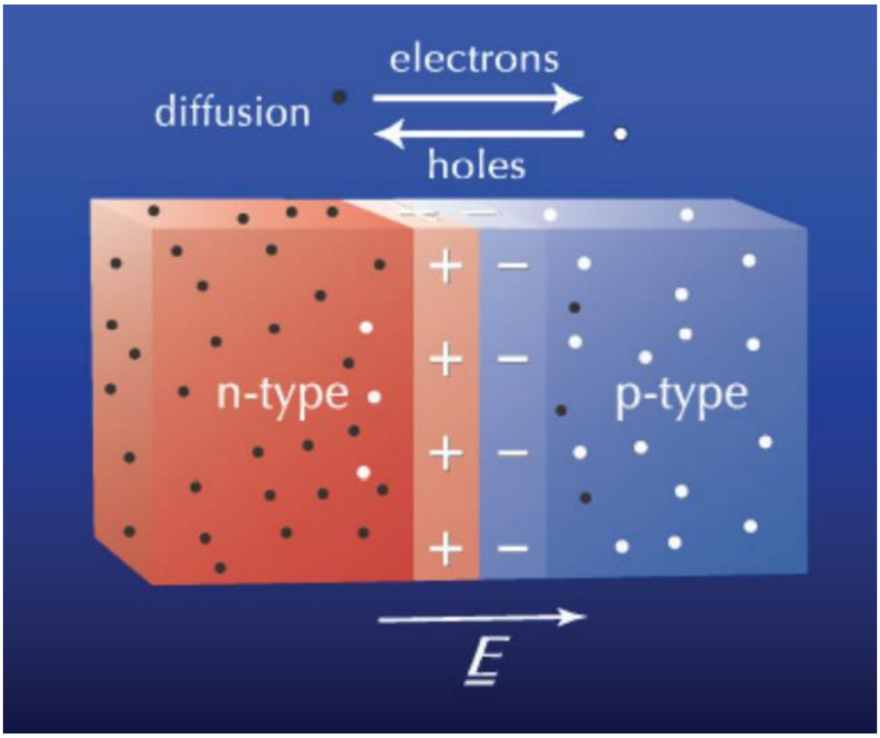

Figure 2.9 Illustration of the p-n junction and depletion region [48].

2.3.1.3 Mechanism of photovoltaic effect in semiconductor

As mentioned in the previous section, the intrinsic semiconductor cannot be used as photovoltaic cells because of the lack of driving force for harvesting the electricity. After introducing a p-n junction, the electrons can be driven out and collected.

In photovoltaic applications, when photons with energy higher than the bandgap enter the depletion region, the electrons in the valence band are excited to the conduction band and become free electrons, leaving holes in the valence band. The excitons are then driven out the depletion region by the built-in electric field and diffuse to the electrodes [51]. The induced voltage difference between the electrodes is called the open-circuit voltage V_{oc}. If the electrodes are connected with a wire, the electrons will flow through the wire and recombine with the holes at the p-type electrode. The corresponding current is called the short-circuit current, I_{sc}.

2.3.2 Ferroelectric photovoltaic effect

Ferroelectric photovoltaic effect is distinct from the photovoltaic effect in semiconductors because of its intrinsically different photovoltaic mechanisms. There are various mechanisms proposed for the anomalous photovoltaic effect appeared in perovskite oxide since its discovery, which is a very high output voltage generated by illumination. The mechanisms were theoretically and experimentally studied over the last few decades but a single mechanism is still lacked for universally explaining all the photovoltaic-related phenomena observed in ferroelectric perovskite oxides.

In the following sections, the well-developed mechanisms of ferroelectric photovoltaic effect will be introduced.

2.3.2.1 Depolarization Field Effect

After poling a ferroelectric perovskite oxide, a net remnant polarization is established in the material across two electrodes. Polarization charges are distributed at the head-side and tail-side of the surfaces, respectively. Usually, the free charges at the electrodes cannot perfectly screen the polarization charges due to the non-coincidence between the centers of gravity of the compensating charges and polarization charges. The net charges produce an electric field opposite to the direction of the polarization and it is named the depolarization field, E_{dp} [52, 53]. As the depolarization field is originated from the charges at the two surfaces of the ferroelectric oxide, its magnitude will be increased with decreasing the thickness. It is believed that the depolarization field should be the major driving force for separating the photo-generated carriers [54]. It is also suggested that the depolarization field may contribute to the anomalous photovoltage but a qualitative study of the relation between the depolarization field and photovoltage has not been reported yet [54, 55].

Different from the semiconductor cells in which only the narrow depletion region with built-in field can separate the excitons, the depolarization field is uniform across the whole ferroelectric oxide and thus the excitons wherever generated can be driven to the electrodes [56]. Furthermore, the phenomenon of the switchable photovoltaic response driven by switching the ferroelectric remnant polarization can be explained by the depolarization field effect straightforwardly.

2.3.2.2 Bulk Photovoltaic Effect

Due to the non-centrosymmetric properties of ferroelectric perovskite oxides, the transition probability of an electron from a momentum k state to k' state is not equal to that of the reverse process. The imbalance transition probability provides a non-symmetric momentum distribution for the photo-generated. Consequently, a short-circuit current J_{SC} will be generated under above-bandgap illumination [57]. The short-circuit current can be described as:

$$J_{SC} = G\alpha I \cdots\cdots (2.5)$$

where G is the Glass coefficient, α is the material absorption coefficient and I is the incident light intensity. The total current J in general case with the present of electric field can be expressed as:

$$J = J_{SC} + (\sigma_d + \sigma_{ph})E \cdots\cdots (2.6)$$

where σ_d and σ_{ph} are the dark conductivity and photoconductivity of the material, respectively, and E is the electric field. The open-circuit voltage V_{OC} can be expressed as:

$$V_{OC} = E_{OC}d = \frac{J_{SC}d}{\sigma_d + \sigma_{ph}} = \frac{G\alpha Id}{\sigma_d + \sigma_{ph}} \cdots\cdots (2.7)$$

where d is the electrodes distance. From Equation 2.7, it can be seen that V_{OC} is not dependent on the bandgap but the electrodes distance. It is believed that the anomalous photovoltaic effect can be explained by this model [58].

In some cases, e.g. in Fe-doped LiNbO3 crystals, V_{OC} is linearly related to the incident light intensity (I) if the photoconductivity σ_{ph} is not sensitive to I and is significantly smaller than σ_d. However, a constant V_{OC} can be observed over a range of I if σ_{ph} is sensitive to I and is significantly larger than σ_d. This phenomenon is observed in Fe-doped $KNbO_3$ crystals. It is explained that the differences in photoconductivity are contributed by the life time of the photo-generated carriers [59].

2.3.2.3 Domain wall Theory

Domain wall theory is the most recent model proposed by Yang *et al*. to explain the ferroelectric photovoltaic effect. With the support of their experimental results, they asserted that the separation of charges was attributed to the potential steps at the domain walls [22]. The existence of potential steps in domain walls was also theoretically proofed before the Yang's experiment [60].

In Yang's experiment, it was observed that the photovoltage of a BFO film increased linearly with the electrode distance, i.e. the number of domain walls, along the polarization direction (Figure 2.10a, c and e). The potential drop at each domain wall was calculated to be approximately 10mV, independent of the width of the domain. The photovoltaic effect disappeared when the electrodes were deposited perpendicularly to the polarization direction (Figure 2.10b and d) [22].

In this model, the open-circuit voltage ~~output~~ is actually the sum of the potential drops at the domain walls. Therefore, the open-circuit voltage is, again, not dependent on the bandgap but the number of domain walls existed between the electrodes. It is also suggested that the ferroelectric photovoltaic effect is dominated by the domain wall effect. Owing to the higher recombination rate, the lifetime of the photogenerated excitons in the domains is normally shorter. Thus, the bulk photovoltaic effect is neglected in the domain wall model [22, 61].

However, the domain wall model is still controversial as it fails to fully explain the phenomena existed in some later studies. First, Bhatnagar *et al*. revealed an angular dependency of photoresponse on the polarized incident light [62]. The domain wall model could not explain this phenomenon well because the photoresponse in this model is originated from the potential drops at domain walls and then is independent of the light polarization direction. Secondly, Nakashima *et al*. showed an above-bandgap open-circuit voltage in a single-domain BFO film [63]. Obviously, the film contains no domain walls and the open-circuit voltage should then be generated by other mechanisms rather than the domain wall model. Finally, Alexe *et al.* showed that the lifetime of photo-generated carriers in domains has no significant difference with that in domain walls. And it is further proposed that the anomalous photovoltaic response should not be dominated by the domain wall effect but the bulk photovoltaic effect [62, 64, 65].

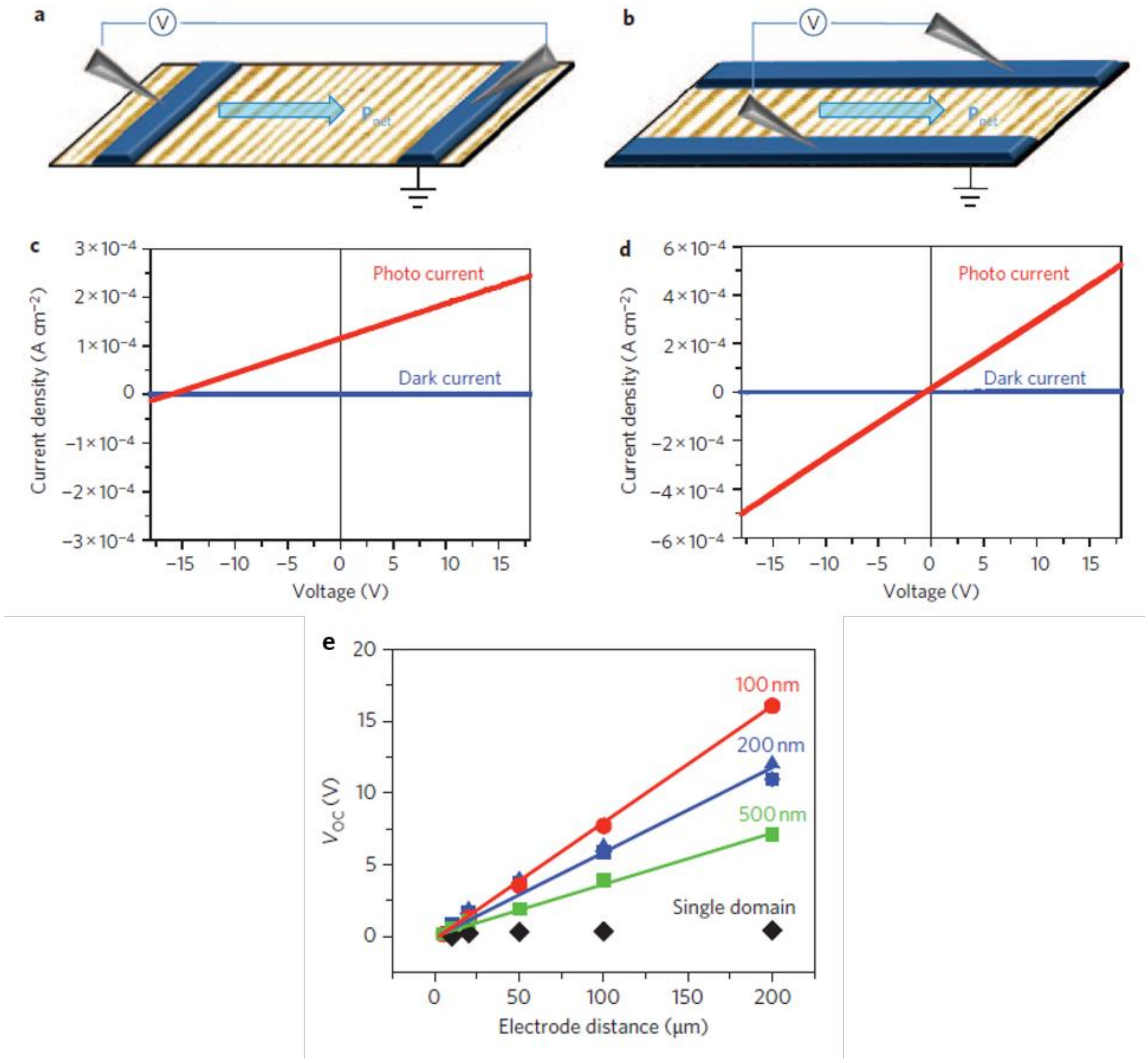

Figure 2.10 The schematics diagrams showing the electrodes in a) parallel and b) perpendicular direction to domain walls. The corresponding I-V characteristic of the sample shown in a) and b). e) The electrode distance dependence of open-circuit voltage measured on 100nm, 200nm and 500nm film, as well as a single domain film with no domain walls [22].

2.3.2.4 Schottky Barrier Effect

Schottky barrier effect is considered as one of the driving forces for the separation of the photo-generated charges. The effect exists only when two different materials are used as electrodes on a homogeneous ferroelectric oxide. When two materials with different work functions are brought into contact, an energy barrier will be formed at the interface. A built-in electric field is formed in the region near the interface. It is analogous to the built-in electric field at the p-n junction of semiconductors. The output photovoltage is limited by the bandgap of ferroelectric oxides [66].

The difference between the barrier heights at the bottom and top electrodes determines the direction and magnitude of the photo-response output. By proper selection of electrodes material, the photovoltaic response could be enhanced by the Schottky barrier effect [18, 67].

2.3.2.4 Optical Properties of Ferroelectric Perovskite Oxide

Ferroelectric perovskite oxides usually have a relatively large bandgap due to the presence of ionic bonds between transition metals and oxygen. In an excitation process across the bandgap, an electron is excited from the 2p state of oxygen (which locates in the valence band) to the d states of transition metals (which locate in the conduction band). The excitation requires high energy because of the large differences in electronegativity between transition metals and oxygen. Thus, the bandgap is much larger than that in semiconductor, which consists of covalent bonds [12]. Most of the conventional ferroelectric perovskite oxides have a bandgap larger than 3 eV [26, 27, 68-70], while BFO thin films and single crystals exhibit a low bandgap of 2.7 eV and 2.2 eV, respectively [21]. Owing to the large bandgap, the ability to utilize the solar spectrum is limited and only 25% of solar energy can be absorbed using BFO single crystals.

2.3.3 Photovoltaic effect comparison on semiconductors and ferroelectric perovskite oxides

For semiconductors, the solar power conversion efficiency, η, is governed by the short-circuit current, I_{SC}, and open-circuit voltage, V_{OC}. It can be expressed as:

$$\eta = \frac{I_{SC} \times V_{OC} \times FF}{P} \cdots\cdots (2.8)$$

where FF is the fill factor and P is the total power of incident light.

Both I_{SC} and V_{OC} are influenced by the bandgap. A narrow bandgap will lead to a larger I_{SC} because a wide solar spectrum can be absorbed. At the meantime, it will reduce V_{OC} because V_{OC} is bounded by the bandgap. A wide bandgap will increase V_{OC} but reduce I_{SC}. Figure 2.11 shows the theoretical maximum efficiency as a function of bandgap energy for a single p-n junction solar cell. The maximum solar energy conversion efficiency is 33.7% obtained in a single p-n junction semiconductor with a bandgap of 1.34 eV [71].

On the other hand, due to the large bandgap and poor electric conductivity of perovskite oxides, the short-circuit current output is usually extremely low. However, according to the bulk photovoltaic model and the domain wall model, the open-circuit voltage theoretically has no limit. These imply that the solar conversion efficiency of perovskite oxides may be comparable with that of semiconductor-based solar cells. To achieve a high conversion efficiency, studies focusing on reducing bandgap and enhancing conductivity while maintaining the remnant polarization and optimizing the devices' structure are suggested.

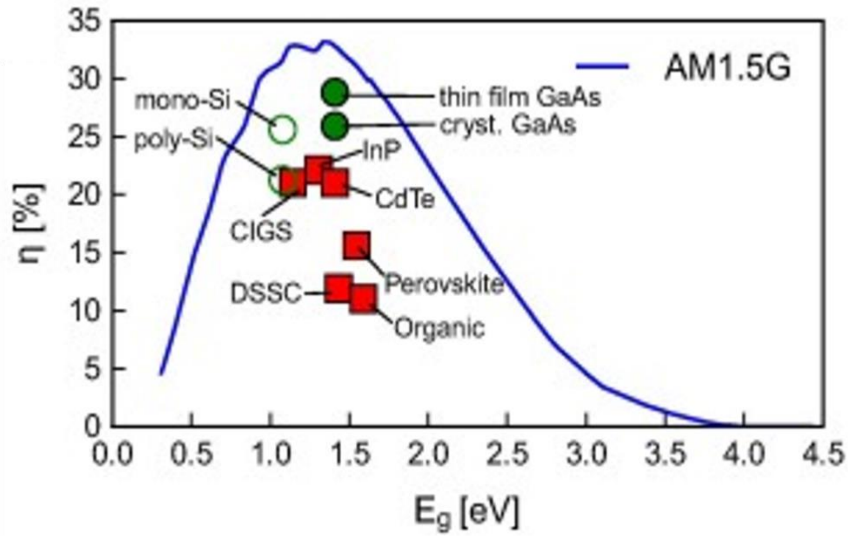

Figure 2.11 The theoretical maximum efficiency of a single p-n junction solar cell in function of bandgap. The bandgaps and maximum obtained efficiencies from different materials are also shown.

2.3.4 Review on the state-of-the-art researches

The researches in the field of ferroelectric photovoltaic effect focus mainly on engineering the bandgap or device structure to obtain higher power conversion efficiency or to achieve other purpose.

In 2013, Grinberg *et al*. reported a successful bandgap engineering on ferroelectric perovskite oxides. The solid-state $[KNbO_3]_{0.8}[BaNi_{0.5}Nb_{0.5}O_{3-q}]_{0.2}$ was fabricated using conventional methods, and the bandgap was found highly tunable with a range of 2.7 eV and can be surprisingly low with 1.1eV (Figure 2.12a). The high concentration of Ni^{2+} substituted the Nb^{5+} and high density of Oxygen vacancy, V_o. The large size of K and Ba cations favor the formation of high density of vacancy. The low bandgap is attributed to the Ni-V_o-Ni bonds, confirm with the reported electronic structure simulation. Also remark that the ferroelectric properties and the magnitude of remnant polarization were maintained. The sample also shows a polarization direction dependence current [12]. However, the KBNNO was in ceramic form and the photocurrent was too low to be utilized in energy harvesting applications. Better performances are expected in KBNNO high-quality thin film.

In 2014, Nechache, R., *et al*. demonstrated another bandgap engineering by modifying the cationic order and domain size. The bandgap of 1.4eV was obtained in Bi_2FeCrO_6(BFCO) double perovskite via the modifications in domain size (D) and Fe/Cr cationic ordering parameter (R). It was found that increasing R and enlarging D can reduce the bandgap (Figure2.12b and c). The research group then fabricated a solar with multilayered thin film structure using BFCO film with different R and D as different layers. By superpositioning the absorption peak from different layers, a record-breaking efficiency of 8.1% was achieved [72]. Besides, modifying the electrode materials and film thickness would also boost the efficiency because of the enhanced photocurrent. A high energy conversion efficiency of 19.5% in PLZT film is predicted by simulation [73]. It would undoubtedly draw attentions to researchers for experimental verifications.c

In 2016, Wang L, *et al* reported a new approach of utilizing the $BiFeO_3$ (BFO) perovskite oxide. The BFO was used as an oxide dye and interfaced with charge-transporting TiO_2 nanoparticles. The photovoltaic properties were improved by improving the charge extraction efficiency, which 1.0 V of open-circuit voltage was obtained and the fill factor of 55% is reached. It is the highest fill factor recorded by far. [74]

In 2017, Wu, M, *et al* bandgap engineered the $SrBi_2Nb_2O_9$ (SBNN) via Ni doping. The $Sr_{0.91}Bi_{2.09}Nb_{1.91}Ni_{0.09}O_{8.91}$ showed the lowest bandgap of 2.25 eV. The remnant polarization was remained at a high level of 2.5 $\mu C/cm^2$, despite the high concentration of Oxygen vacancy it has. The experimental results were confirmed with first-principle calculation. [75]

On the other side, Han, H, *et al* reported a new method of bandgap engineering. The bandgap of hexagonal $YbFeO_3$ (h-YbFO) was reduced by introducing compressive strain. The photovoltaic efficiency of h-YbFO/Pt/MgO heterojunction device with compressive strain was reported 3 times better than that of h-YbFO/Pt/A12O3 device with tensile strain. Confirmed with the density functional theory, the compressive strain on h-YbFO could enhance the polarization and reduce the bandgap as well. Thus, it leads to an improvement on photovoltaic efficiency. [76]

In 2018, another method of improving the power conversion efficiency has been reported by Chakrabartty, J, *et al*. The power conversion efficiency of $BiMnO_3$ have been improved and reached 4.20% by mixing $BiMn_2O_5$ crystal phases. It was reported that the short-circuit current (I_{sc}) and open-circuit voltage (V_{oc}) are not developed within the grains but the grain boundaries and interfaces. It is further reported that the I_{sc} and V_{oc} could be tuned by tuning the electrical resistance of the device.[77]

Other than the application of solar energy harvesting, it may also possible to utilize the ferroelectric photovoltaic effect in various applications due to its above-bandgap photo-voltage and the polarization direction sensitive photo-current. Last but not least, the ferroelectric perovskite oxide may combine its photovoltaic effect with piezoelectric or pyroelectric effect in some applications to boost its multifunctionality.

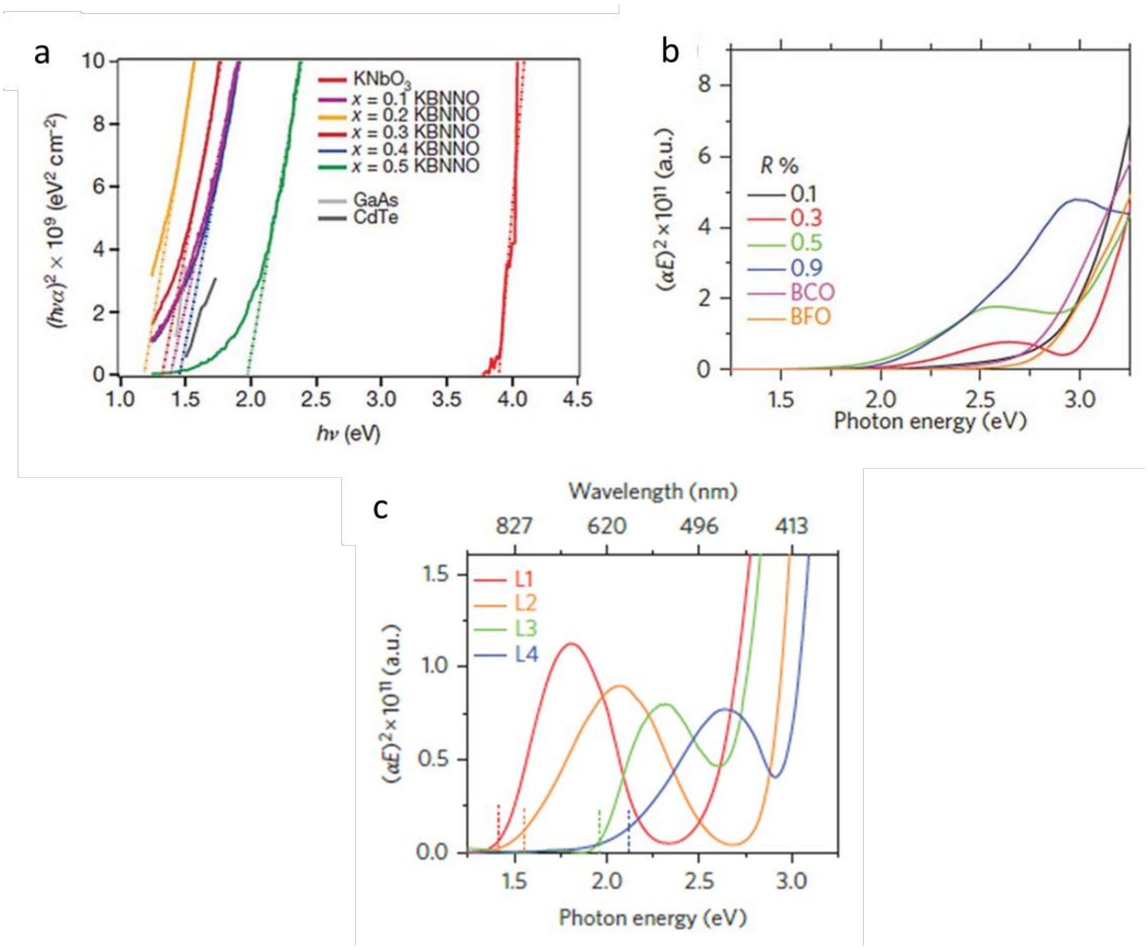

Figure 2.12 Tauc plots of a) KBNNO [12], b) BFCO with various R value and c) BFCO with various Domain size, L1 has the largest size (26nm) and L4 has the smallest (10nm) [72].

Chapter 3. Sample Fabrication and Characterizations

3.1 Introduction

Among the lead-free perovskite oxides, $K_{0.5}Na_{0.5}NbO_3$ (KNN) has drawn attention to the researchers due to its promising piezoelectric and ferroelectric properties, as well as its high Curie temperature, which are comparable to those of PZT [28, 78]. However, the ferroelectric photovoltaic effect of KNN has not been widely studied. To study the ferroelectric photovoltaic effect of KNN, one major obstacle is its poor densification by the conventional solid state sintering. It leaves many micron-size pores on the surface and inside the bulk. As an interdigital electrode pattern, with micro-size electrode gaps, will be deposited on the sample surface, the pores would lead to great problems in the pattern deposition. To overcome the problem, MnO_2 and CuO were chosen as additive dopants since they have been shown to be effective sintering aids for densifying the KNN ceramics in others' previous studies [79-81].

In this Chapter, the fabrication of the ceramic samples will be described. Then, the characterization method will be introduced. Finally, the result of the sample characterization will be presented and discussed.

3.2 Sample Fabrication

Before the sample fabrication, all the equipment was cleaned by 99.9% Ethanol to prevent contamination to samples. In this study, $K_{0.5}Na_{0.5}NbO_3$ (KNN), $K_{0.5}Na_{0.5}NbO_3$

+ 0.25 mol% MnO_2 (KNN-Mn) and $K_{0.5}Na_{0.5}NbO_3$ + 1 mol% CuO (KNN-Cu) were fabricated. Since alkali metal carbonates are sensitive to moisture, they were kept in an oven at 150 °C for 8 hours or above before use.

3.2.1 Conventional fabrication

The raw materials used are shown as follows:

1. Sodium carbonate - Na2CO3 (99%, International Laboratory USA)
2. Potassium carbonate - K2CO3 (99.9%, International Laboratory USA)
3. Niobium pentoxide - Nb2O5 (99.99%, Sinopharm Chemical Rengent Co. Ltd.)
4. Manganese dioxide - MnO_2 (99.9%, International Laboratory USA)
5. Copper Oxide – CuO (99%, International Laboratory USA)

The raw powders were weighed in stoichiometric ratio with an electronic balance (ME204, Mettler Toledo), and then were mixed and milled by zirconia balls in an ethanol-filled milling bowl for 8 hours. The mixture was placed into an oven at 150°C to vaporize the ethanol. The remained mixed powder was calcinated at 800°C for 2 hours in an alumina crucible. The temperature profile is shown in the inset of Figure 3.1. The calcinated powder was then ball-milled again for 8 hours. For KNN-Mn and KNN-Cu, the additive was weighed and added before ball-milling.

After drying in an oven, the powders were mixed with a 5-wt% polyvinyl alcohol (PVA) solution. The weight ratio of the powders to the PVA solution was 1 : 0.015. The mixture were then mixed, grinded, dried, sieved with a 80-mesh screen, and finally pressed into disc samples with a diameter of 12 mm under a pressure of ~70 MPa. The samples were then baked at 650°C for 2 hours, with a slow increasing rate, to burn out the PVA binder. Finally, dense ceramics discs were obtained by sintering at 1090 – 1110^{o}C for 2 hours in air. A brief working flow with temperature profiles for the calcination and sintering processes is shown in Figure 3.1,.

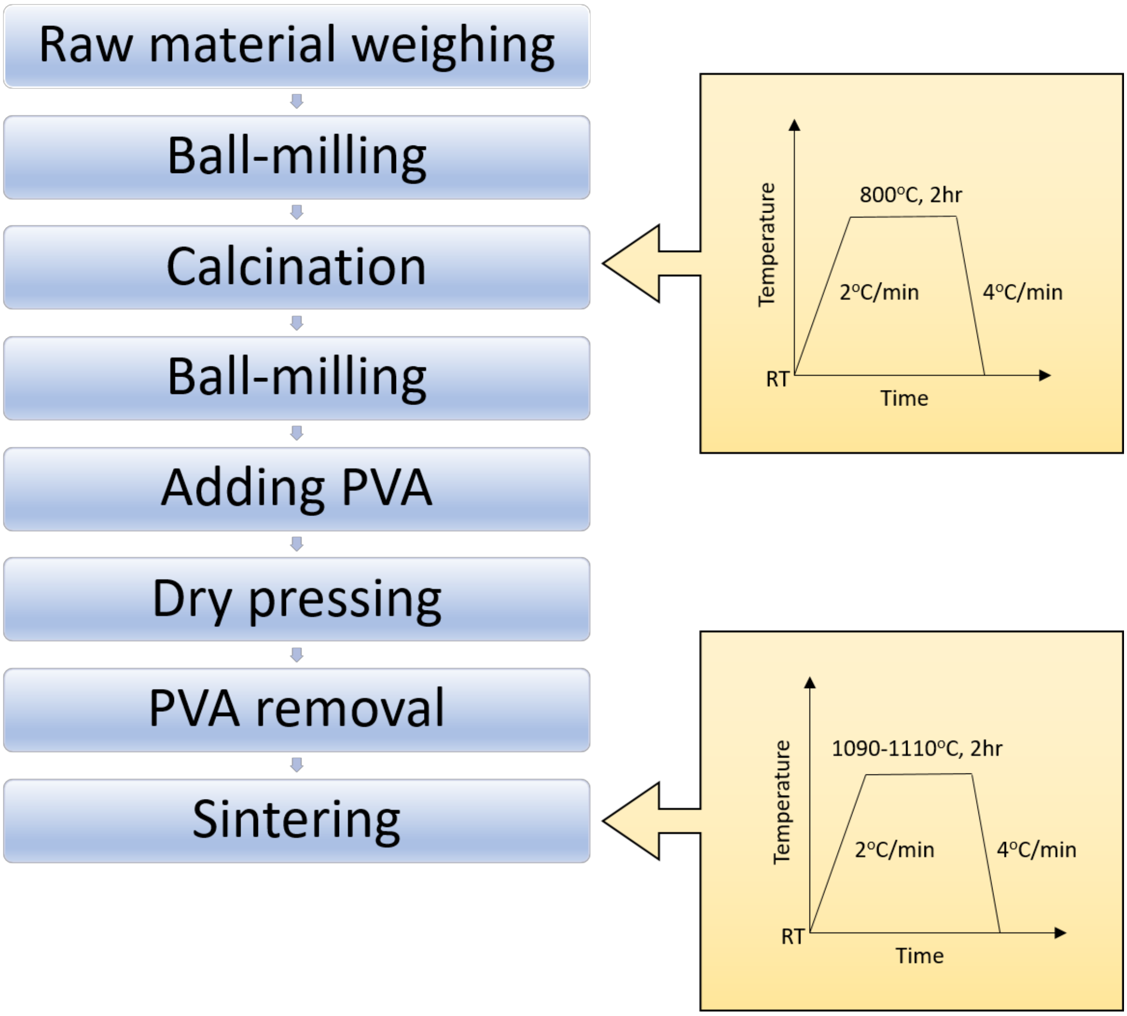

Figure 3.1 Working flow of conventional sintering technique.

3.2.2 Poling

Before poling, both surfaces of the as-sintered ceramics were polished using 2000 Grit sandpapers to reduce the surface roughness and obtain a uniform thickness. Silver electrodes were then fired onto both surfaces at 750 °C for 30 mins.

To obtain a net remnant polarization, the ceramics have to be poled under a bias electric field above the coercive field E_C. The sample was placed in a silicone oil bath and heated to 150°C. A D.C. voltage was applied according to the sample thickness to provide a poling field along the thickness direction. The sample was cooled down in the oil bath after 30-mins poling. The poling field was remained until the temperature decreased to room temperature. A schematic diagram of the poling system is shown in Figure 3.2

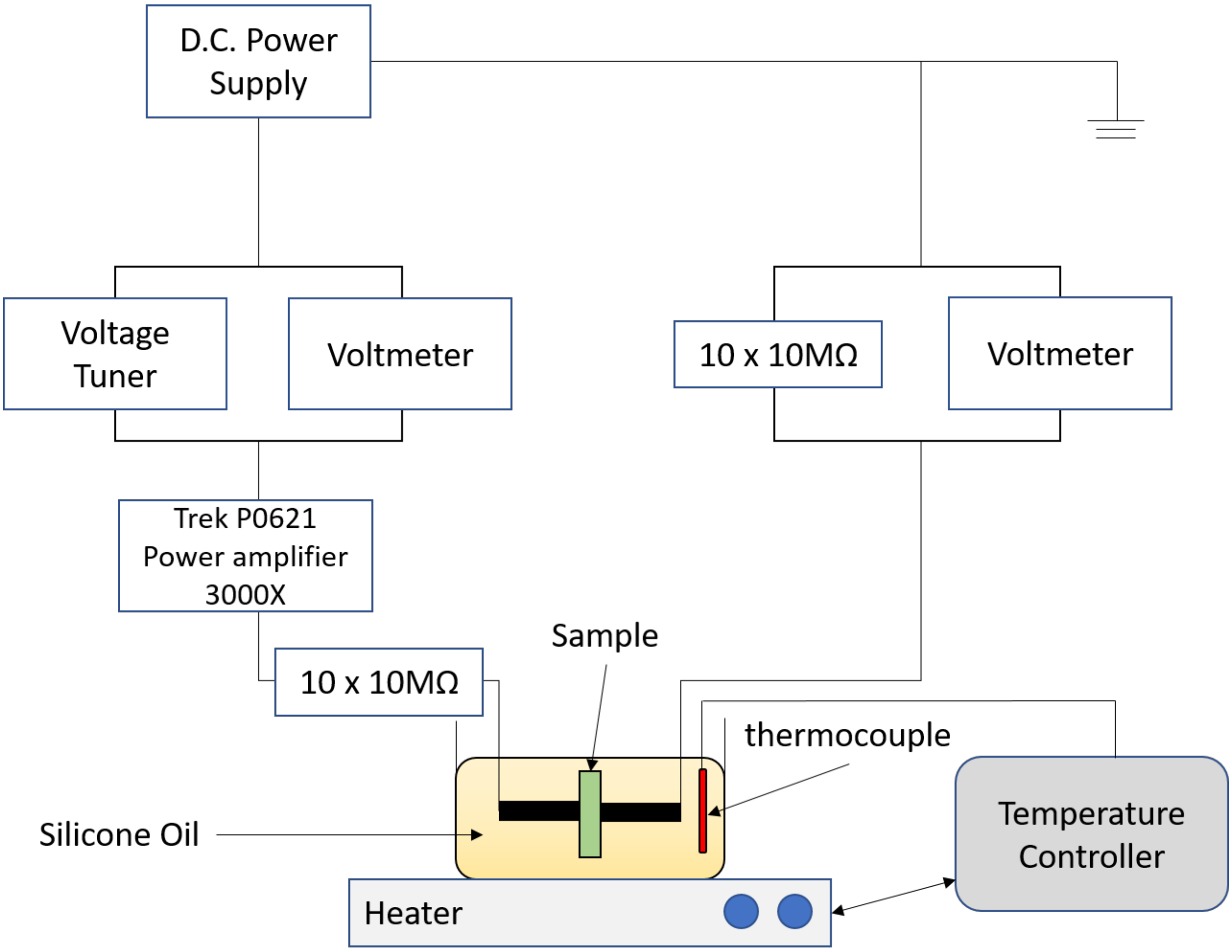

Figure 3.2 Schematic diagram of the poling system

3.3 Sample Characterization

In this section, the characterization methods adopted in this study will be introduced. The characterizations are roughly divided into three parts: general and structural characterization, electrical characterization and optical characterization.

3.3.1 Structural Characterization

3.3.1.1 Density measurement

The density of a ceramic is very dependent on the fabrication conditions. It indicates the ceramic's quality. Contaminations during preparation or improper sintering conditions may cause impurities and pores inside the ceramic and lower the density. Consequently, the performance of the ceramic, in most of the applications, will be degraded.

In this study, the density of samples was determined using Archimedes' principle. The dry mass, m_{dry}, of the sample was measured in air. The same sample was then immersed in water and the corresponding mass, m_{water}, was measured. The density of the sample was calculated using Equation 3.1:

$$\rho = \frac{m_{dry}}{m_{dry} - m_{water}} \cdot \rho_{water} \cdots\cdots (3.1)$$

where ρ is the density of the ceramic and ρ_{water} is the density of water. The density of water is assumed to be 1000 kg/m^3.

The density of a material is compared to its theoretical density, TD, to evaluate the quality. The TD can be calculated by Equation 3.2.

$$TD = \frac{\sum_{i=0}^{k} n_i M_i}{V N_A} \cdots\cdots(3.2)$$

where n_i is the number of the ith atom contained in the unit cell, M_i is the molar mass of the ith atom, V is the volume of the unit cell and N_A is the Avogadro constant. The volume of the unit cell can be calculated with the lattice parameters obtained from XRD results.

3.3.1.2 X-Ray Diffraction (XRD)

The X-Ray Diffraction, or XRD, is a tool to study the crystal structure of crystalline materials by analyzing the diffraction pattern produced via the interactions between the X-ray and the crystal lattices. XRD may be used to identify unknown crystals or determine the lattice parameters. Absorption, transmission and scattering will be occurred when an X-ray beam is incident on the sample. The scattered X-ray from the lattices produces a diffraction pattern. The diffraction peaks appear at certain incident angle according to Bragg's Law (Equation 3.2).

$$2d_{hkl} \sin\theta_{hkl} = n\lambda \cdots\cdots(3.2)$$

where h, k and l are the miller index, d is the interplanar spacing of $\{hkl\}$ set of lattice planes, θ_{hkl} is the incident angle of X-ray beam, n is the order of diffraction, and λ is the wavelength of the incident X-ray.

In this study, the powder-form samples were used for the characterization. The as-sintered ceramic samples were grinded into powder form and sieved with a 80-mesh screen. The X-ray used was CuK_{α} radiation with $\lambda = 0.154$ nm (SmartLab, Rigaku Co., Japan).

3.3.1.3 Scanning Electron Microscope (SEM)

SEM is an electron microscope that produces images with resolution in sub-nano scale. The SEM is consisted of 3 main parts: an electron source, a lens system, and detectors.

The system works at vacuum environment to reduce the collision between electrons and air particles. In the operation, electrons are generated by an electron gun and accelerated toward the lens system. The electron beam is focus by the lens system and incident on the specimen with a spot area of few nanometers. Various signals will be obtained, such as secondary electrons (SE), backscattered electrons (BE), auger electrons and characteristic X-rays. The topography information can be obtained from the SE. A secondary electron detector is placed next to the specimen with few hundred volts to attract the low-energy SE. The number of SE generated is determined by the specimen surface, and a greater number of SE will generate a brighter image spot. By the contrast in brightness, a topography image is obtained. A schematic block diagram of SEM is shown in Figure 3.3.

In this study, JEOL Model JSM-6490 was used for topography analysis. The as-sintered ceramic samples were cleaned using acetone and ethanol to remove the organic substance that may adhere on sample surface. A thin layer of gold was then deposited on the sample using sputtering before the SEM characterization.

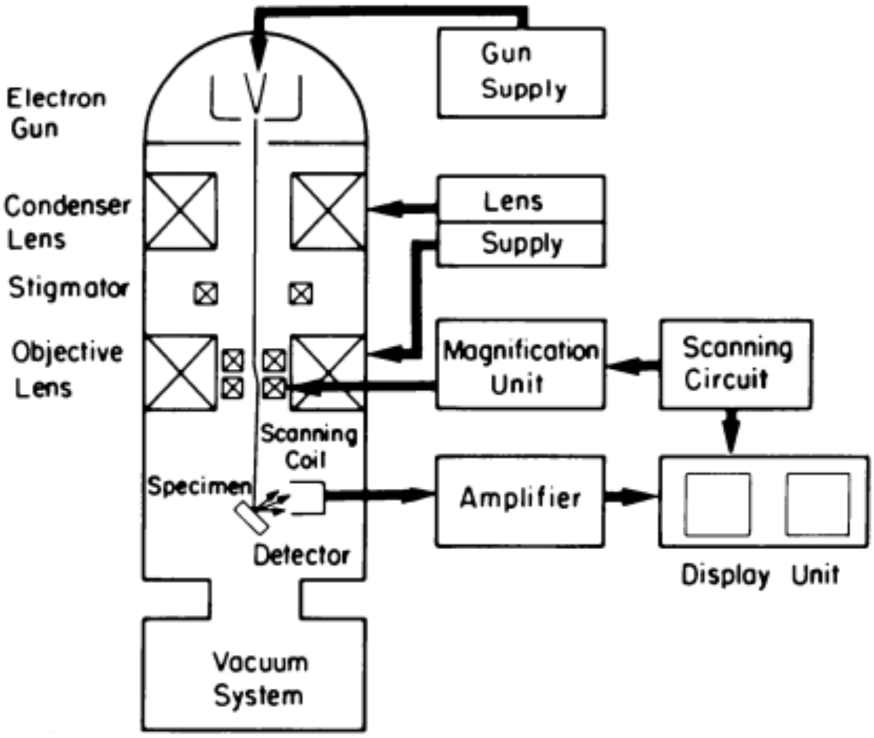

Figure 3.3 Schematic block diagram of SEM [82]

3.3.2 Dielectric Characterization

3.3.2.1 Dielectric Properties Measurement

A Schering bridge-based impedance analyzer (4294A, Agilent) was used for measuring the relative permittivity ε_r and dielectric loss $\tan\delta$ of the samples. The properties were measured at room temperature with 1k Hz measuring voltage. The relative permittivity ε_r was calculated from Equation 3.3.

$$C = \frac{\varepsilon_0 \varepsilon_r A}{d} \cdots\cdots (3.3)$$

where C is the measured capacitance, ε_0 is the permittivity of the free space, A is the area overlapped by two electrodes and d is the sample thickness.

The relative permittivity ε_r can be expressed in complex form (Equation 3.4) as dielectric materials may dissipate energy.

$$\varepsilon_r = \varepsilon' - \varepsilon'' \cdots\cdots (3.4)$$

where ε' and ε'' are the real part and imaginary part of the permittivity, respectively. The dielectric loss $\tan\delta$ is then defined as Equation 3.5

$$\tan\delta = \frac{\varepsilon''}{\varepsilon'} \cdots\cdots (3.5)$$

3.3.2.2 Piezoelectric Properties Measurement

The piezoelectric coefficient d is the relation between the charge generated at the electrodes and the applied stress or the relation between the induced strain and the applied electric field. (Equation 3.6 and 3.7)

$$d = \frac{induced\ strain}{applied\ electric\ field} \left({}^{m}/_{V}\right) \cdots\cdots (3.6)$$

$$d = \frac{short\ circuit\ charge\ density}{applied\ mechanical\ stress} \left({}^{C}/_{N}\right) \cdots\cdots (3.7)$$

The direction of the applied mechanical stress can be depicted by subscript “1”, “2”, “3”, “4”, “5” and “6”, where “1” and “2” are the direction perpendicular to the polarization axis “3” and “4”, “5”, and “6” are the shear planes perpendicular to the directions “1”, “2” and “3”, respectively. The piezoelectric coefficient is presented as d_{ij}, where i represents the induced polarization direction and the j represents the direction of applied mechanical stress. In this study, the d_{33} coefficient was measured using the d_{33} meter (ZJ-3D, Beijing Institute of Acoustics) after poling.

3.3.2.3 Ferroelectric Hysteresis Loop Measurement (P-E loop)

As introduced in Chapter 2, the remnant polarization P_r and coercive field E_C can be obtained from the P-E loop. The measured E_C is a reference for estimating the poling field for the sample. The measured P_r is a reference for estimating the performance in applications. In this study, the P-E loop was measured using the Sawyer-Tower circuit [35], which contains a ferroelectric capacitor C_F (i.e., the sample) and a reference capacitor C_R. The Schematic setup is shown in Figure 3.4 The capacitance of C_R is 1000 times larger than that of C_F. An A.C. voltage signal was generated using a function generator (HP 8116A). The signal was then amplified using a high voltage amplifier (Trek 609D-6) before applying to the sample. The output voltage from the amplifier (i.e. the input voltage to the sample) and the voltage of the reference capacitor were measured using a digital oscilloscope (HP54645A). The applied electric field and the polarization were calculated using the known area and thickness of the sample and the measured voltages, similar to the calculation reported in [83]. The post-calculated data were then recorded in computer.

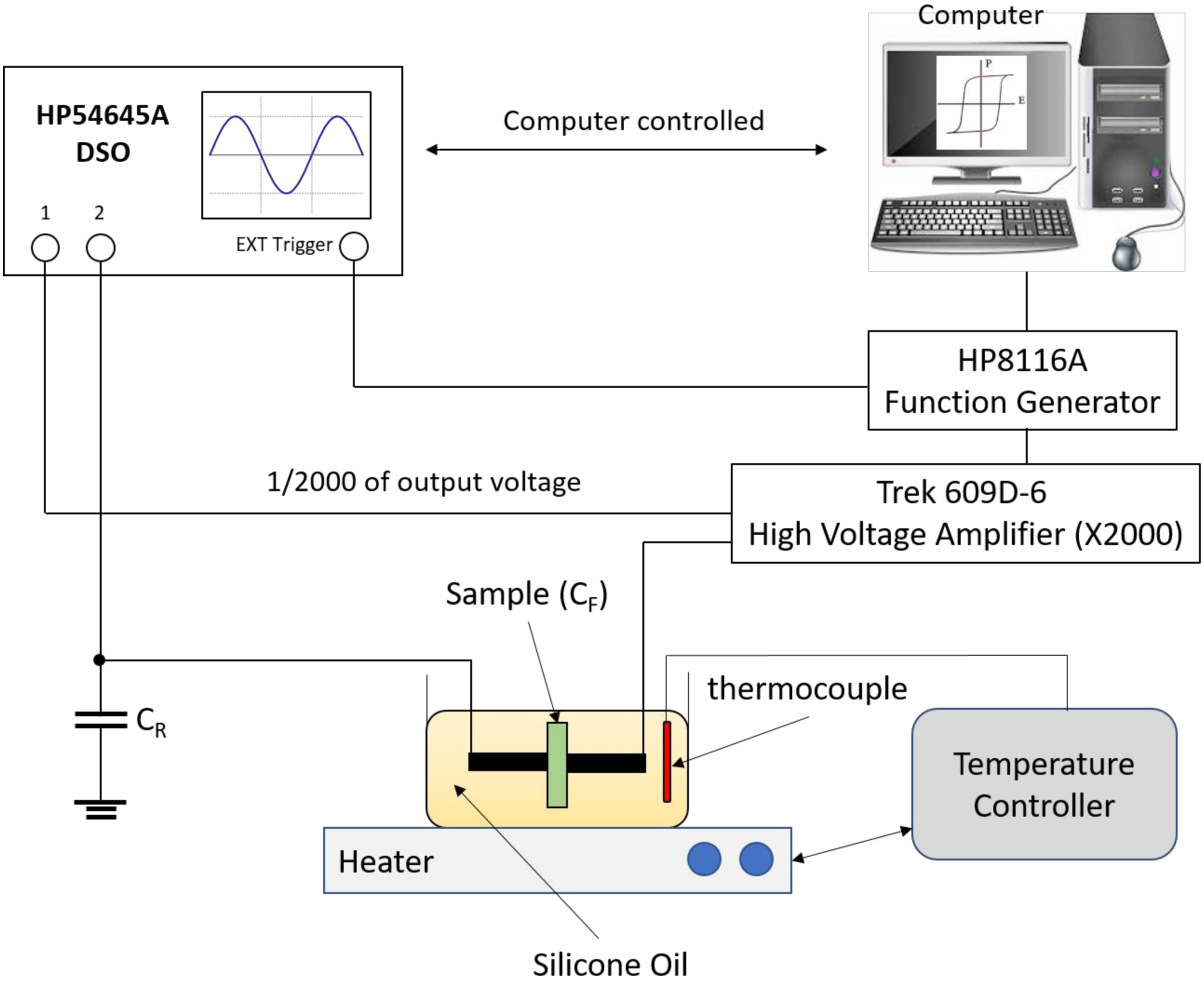

Figure 3.4 Schematic diagram of the setup for the P-E loop measurement

3.3.3 Optical Characterization

In this study, the transmittance and diffuse reflectance of the samples were measured using bulk samples and powdered-form samples, respectively. A UV-Vis spectrophotometer (UV—2550, Shiadzu Co.) was used for the measurement. The measured range was 300-800nm for both transmittance and diffuse reflectance characterizations. Finally, the bandgaps of the samples were estimated using Tauc’s plot by manipulating the data of transmittance and diffuse reflectance.

3.3.3.1 Transmittance

The as-sintered ceramic discs are too thick for light to transmit. Therefore, they were first grinded down to <100 µm to become semi-transparent. Then both surfaces were polished using 1-µm diamond lapping film to obtain mirror-like surfaces to reduce light scattering. The thickness of sample was measured using a thickness gauge (VL-50 Mitutoyo) before the measurements. Since the thin ceramic sample is very fragile, it was attached onto a thin glass using hot glue. The measured transmittance without putting the sample in the light path was taken to be 100%. The sample was then inserted in the light path and the transmittance spectrum was measured. The schematic setup of the measurement is shown in Figure 3.5.

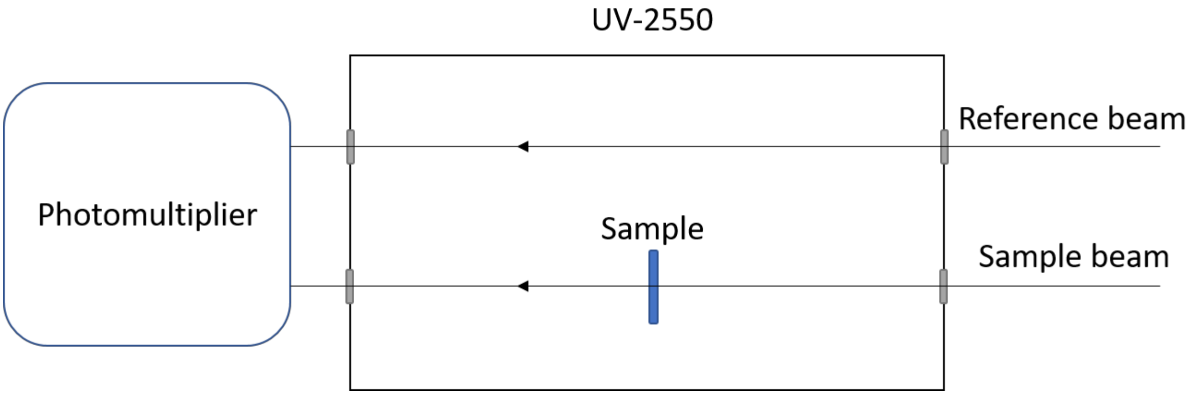

Figure 3.5 Schematic setup for the measurement of transmittance spectra using bulk sample.

3.3.3.2 Diffuse Reflectance

When a light beam strikes on a sample surface, part of it is reflected with respect to the incident angle, which is the specular reflection, and part of it is reflected randomly to different directions, which is the diffuse reflection. Some of the wavelengths may be absorbed during the diffuse reflection, depending on the material, and thus the diffuse reflected beam contains information of the optical properties of the sample. The optical properties of an opaque sample can then be obtained by measuring the diffuse reflectance.

In this study, the diffuse reflectance of the samples was measured using the spectrophotometer (UV-2550) equipped with an integrating sphere attachment (ISR-240A). The inner surface on the integrating sphere is coated with $BaSO_4$ powders. The schematic setup of the measurement and the light paths are shown in Figure 3.6. The sample beam strikes perpendicularly on the sample surface, so most of the specular reflected beam would leave the integrating sphere through the window. As a result, the measured reflectance is mainly contributed by the diffuse reflection.

The samples to be measured were first grinded into powder form and sieved using an 80-mesh screen. Then the sample powder was spread and pressed tightly on a layer of $BaSO_4$ powder in a sample holder. A standard $BaSO_4$ white board was first placed in the sample holder, and its reflectance was taken to be 100%. Then, the sample holder was placed in and the corresponding diffuse reflectance spectrum was measured.

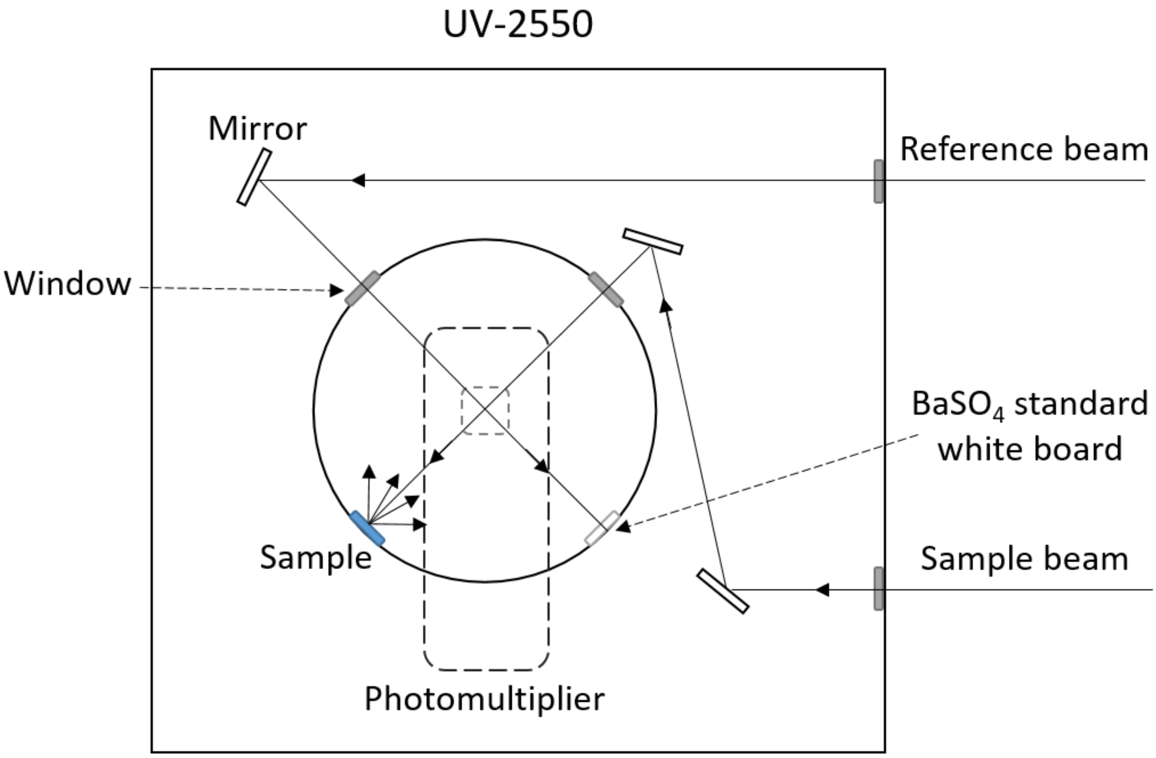

Figure 3.6 Setup for diffuse reflectance measurement. A hole is located at the bottom of the integrating sphere and the photomultiplier is underneath the hole.

3.3.3.3 Tauc's Plot

Tauc's plot is a method to estimate the bandgap of a material, which was proposed by J. Tauc in 1968 [84]. The Tauc's relation is expressed as Equation 3.8.

$$(h\nu\alpha)^n = A(h\nu - E_g)\cdots\cdots(3.8)$$

where h is the Plank's constant, ν is the frequency of the photon, α is the absorption coefficient, E_g is the bandgap, A is a proportional constant, and n is a constant relating to the type of transitions. n = 2 and 1/2 indicate the direct and indirect allowed transitions, respectively, while n = 2/3 and 1/3 indicate the direct and indirect forbidden transitions, respectively.

To estimate the bandgap, $(h\nu\alpha)^n$ was plotted against $h\nu$. By extrapolating the linear region of the curve to the horizontal axis, the intersection of the extrapolating line and the horizontal axis indicates the bandgap energy. A Tauc's plot for $Cd_{0.62}Zn_{0.38}S$ is shown in Figure 3.7 as an example [85].

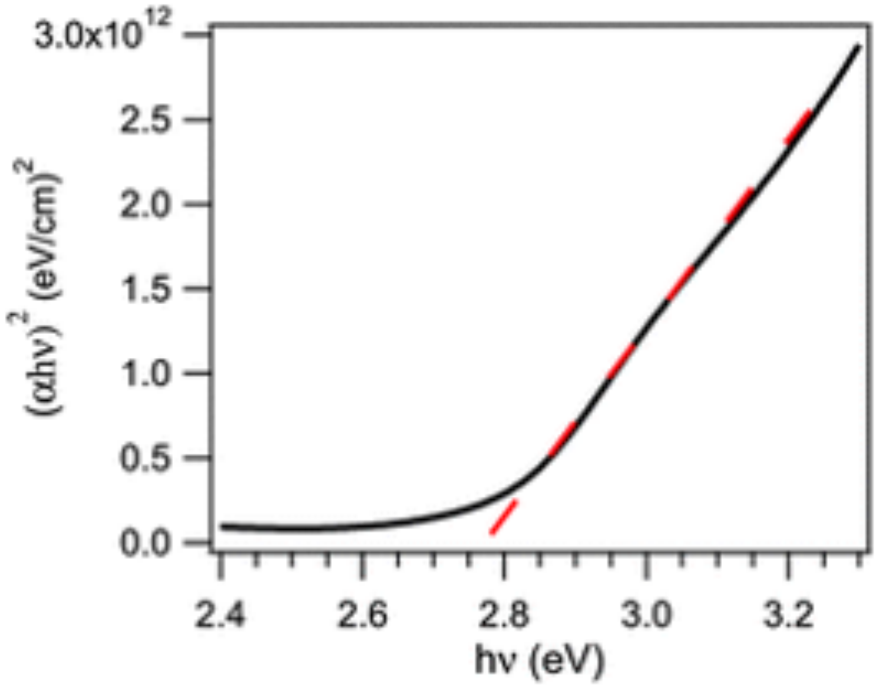

Figure 3.7 A typical Tauc's plot. The red dashed line is the linear fit and the bandgap was estimated to be 2.78 eV [85].

Tauc's Plot obtained from transmittance spectrum and diffuse reflectance spectrum

To obtain a Tauc's plot from a transmittance spectrum, the absorption coefficient α of sample was first calculated from the transmittance T using Equation 3.9.

$$\alpha = d^{-1}\ln(\frac{1}{T})\cdots\cdots(3.9)$$

where d is the sample thickness.

To obtain a Tauc's plot from a diffuse reflectance spectrum, the absorption coefficient α of sample was first calculated from the diffuse reflectance R using the Kubelka-Munk function $F(R\infty)$ (Equation 3.10).

$$\alpha = \frac{(1-R)^2}{2R}\cdots\cdots(3.10)$$

3.4 Results and discussion

The densities of the KNN ceramics added with different additives are shown in Table 3.1. All the samples have reached above 95% of the theoretical density. The KNN-Mn and KNN-Cu ceramics show higher densities. Among them, the KNN-Mn ceramic has the highest density, reaching 98% of the theoretical density. The results are consistent with that reported in ref [81]. MnO_2 and CuO are effective additives for enhancing densification of KNN-based ceramics. Moreover, CuO could decrease the sintering temperature by forming a liquid phase during sintering [79-81]. In this study, the sintering temperature of the KNN-Cu ceramic is decreased from 1110°C to 1060°C. It is believed that the decrease in sintering temperature is attributed to the formation of a liquid phase.

The SEM micrographs of the ceramics are shown in Figure 3.8. All the samples show a dense structure and the grains are generally of rectangular shape. The grain size distributions for the samples are in Figure 3.9. The sample size and bin size for all histograms are 120 and 0.2 µm, respectively. The measured average grain size of the KNN ceramic is 1.4 µm, whereas the grain sizes of both the KNN-Mn and KNN-Cu ceramics are 1.0 µm, smaller than that of the KNN ceramic. The XRD patterns of the KNN, KNN-Mn and KNN-Cu ceramics are shown in Figure 3.10. All the samples show a single-phase orthorhombic perovskite structure. No impurity phases are observed within the XRD detection limit. For the KNN-Mn ceramic, Mn^{3+} may stably exist at the high sintering temperature [86]. The ionic radius of Nb^{5+} (0.68 Å) is close to those of Mn^{3+} (0.66 Å) and Cu^{2+} (0.73 Å). Therefore, it is suggested that some of the Mn^{3+} and Cu^{2+} may have entered the KNN lattices and substituted the Nb^{5+} ions.

Table 3.1 Density of KNN with different additive

Sample	Density (g/cm^3)	Relative Density
KNN	4.29	95%
KNN-Mn	4.44	98%
KNN-Cu	4.32	96%

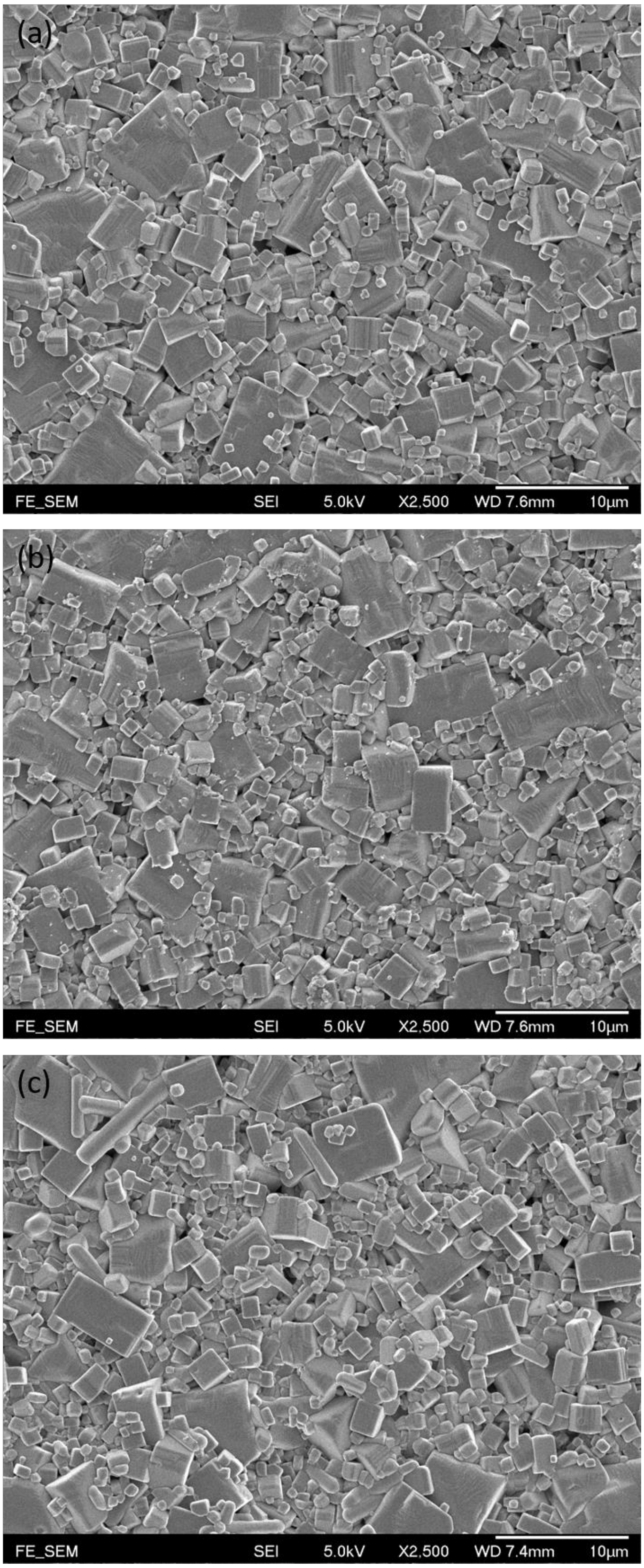

Figure 3.8 SEM micrographs of (a) KNN, (b) KNN-Mn and (c) KNN-Cu, respectively

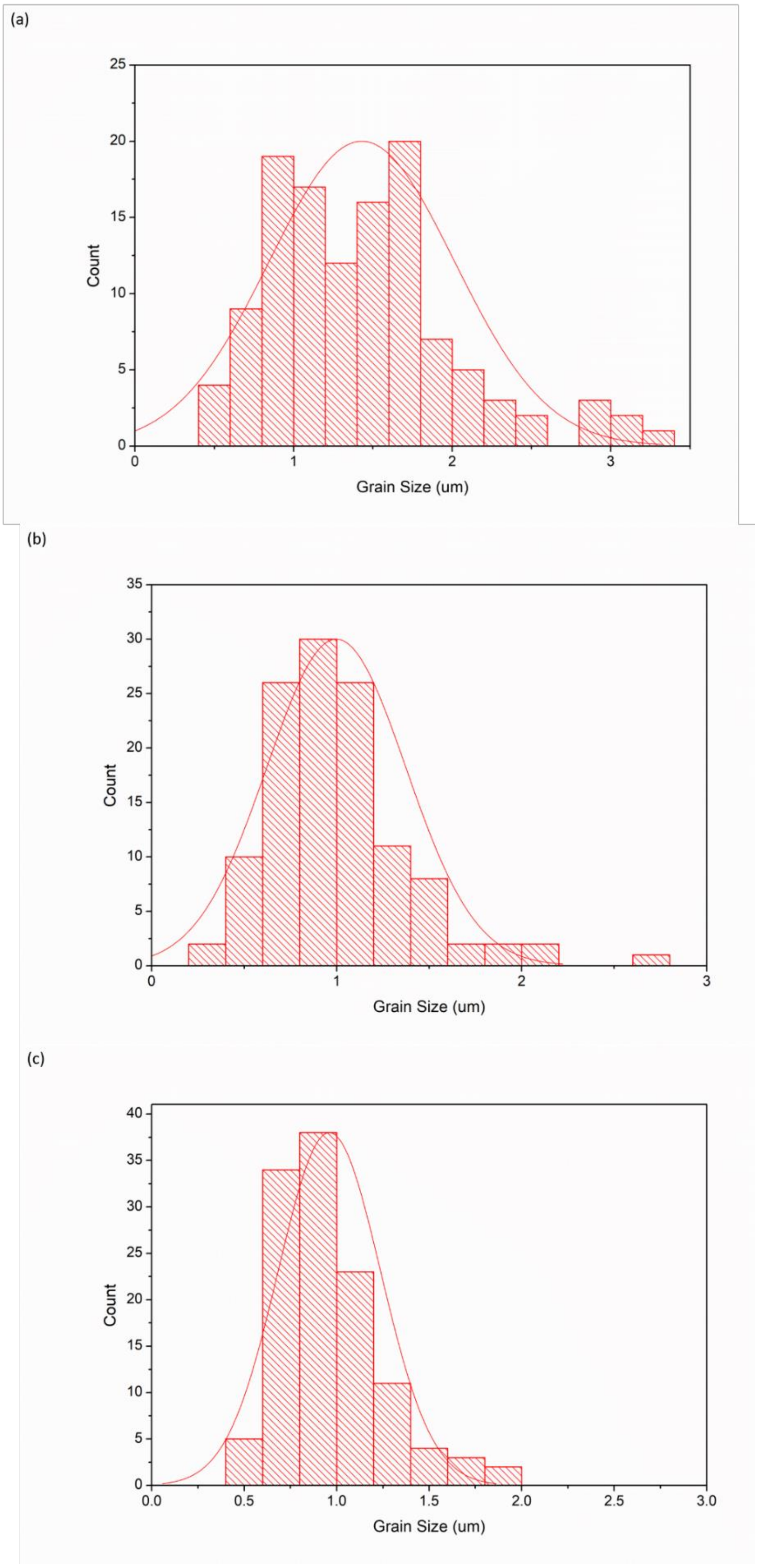

Figure 3.9 Distribution of grain size count on the SEM micrographs (a) KNN, (b) KNN-Mn and (c) KNN-Cu, respectively

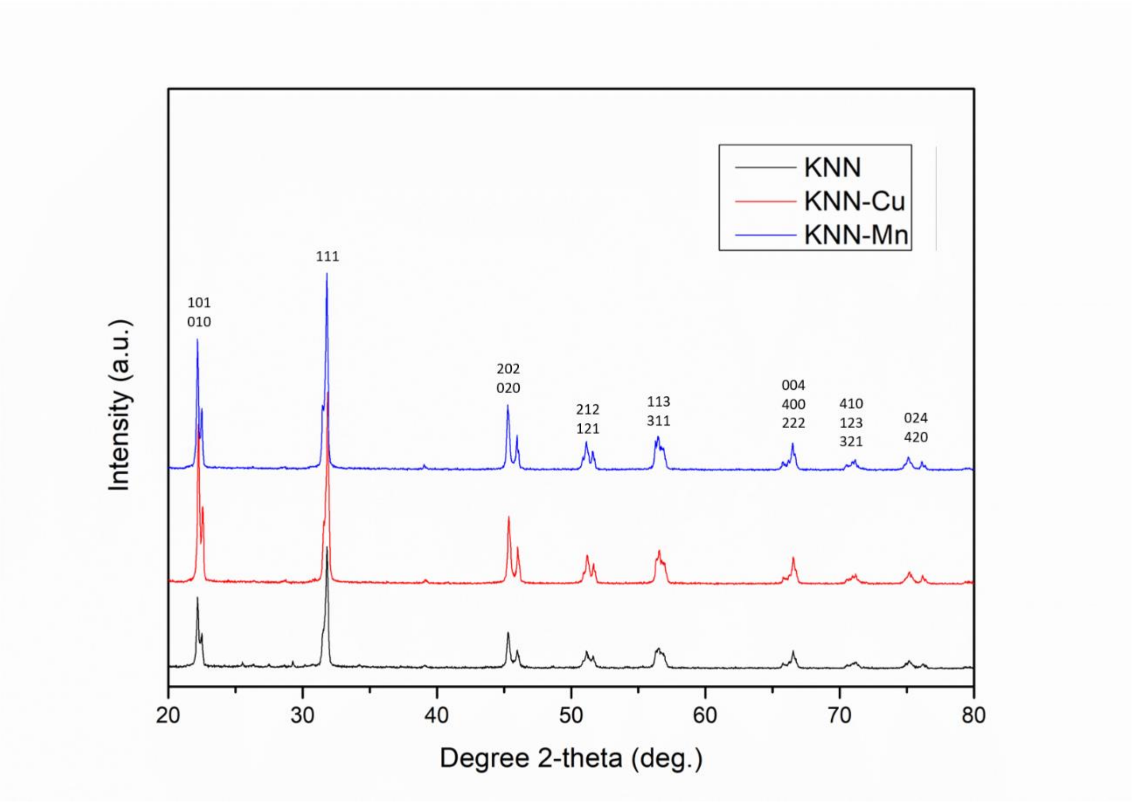

Figure 3.10 XRD pattern of KNN, KNN-Mn and KNN-Cu.

Optical measurement

The measured diffuse reflectance spectra for all the ceramics are shown in Figure 3.11. The measured diffuse reflectance of KNN increases sharply as the wavelength increases from ~350 nm, and then becomes almost unchanged in the range of 400 nm – 800 nm. The KNN-Mn ceramic exhibits similar spectra, except that its diffuse reflectance is lower and increases slowly in the range of 400 - 800 nm. For the KNN-Cu ceramic, the diffuse reflectance is even lower in the range of 400 - 800 nm, and varies more significantly with increasing wavelength, in particularly near 600 nm. The differences in diffuse reflectance may be attributed to the additives [87]. This may also explain why the

KNN-Cu ceramic is greenish dark in color, while the KNN and KNN-Mn ceramics are white and yellowish white, respectively.

The low diffuse reflectance observed for all the ceramics at wavelengths shorter than ~400 nm is attributed to the bandgap absorption. When the incident photons have energy larger than the bandgap (i.e., shorter wavelengths), they will be absorbed and thus leading to a low reflectance.

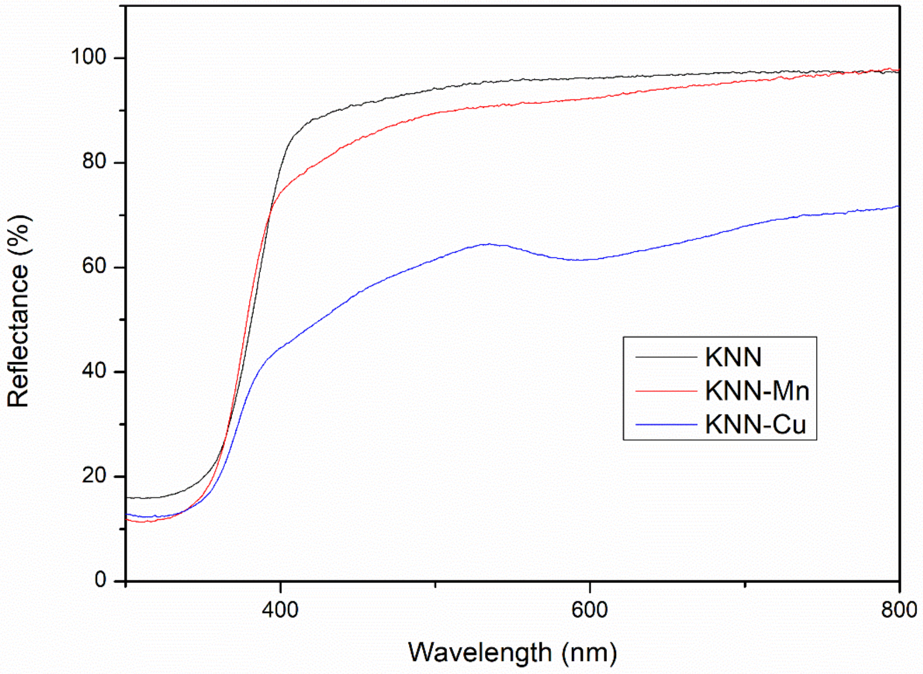

Figure 3.11 The diffuse reflectance spectra of KNN, KNN-Mn and KNN-cu

The Tauc's plots obtained from the diffuse reflectance for the direct (n = 2) and indirect (n = 0.5) transitions are shown in Figure 3.12 and 3.13. The dashed lines show the linear fitting for the linear regions. For the indirect transitions (Fig. 3.13), two fitted lines are obtained for each sample to estimate the indirect bandgap value, i.e., the x value of the intersection. The estimated bandgaps, both direct and indirect, are listed in Table 3.2. The bandgap of the KNN-Mn ceramic is slightly larger than that of KNN. The electronegativity of Mn (1.55) is lower than that of Nb (1.6) [88]. As some of the Mn^{+3} may substitute the B-site Nb^{5+}, the electronegativity difference between the B-site ions and oxygen may increase. Consequently, the bandgap of the KNN-Mn ceramic may thus be increased. Despite the higher electronegativity of Cu (1.9), the estimated bandgaps of the KNN-Cu are similar to those of KNN. This may be attributed to the limited substitution of Cu2+ for the B-site Nb^{5+} arisen from the large difference in ionic radii (Cu radius 0.73 Å vs Nb radius 0.64 Å).

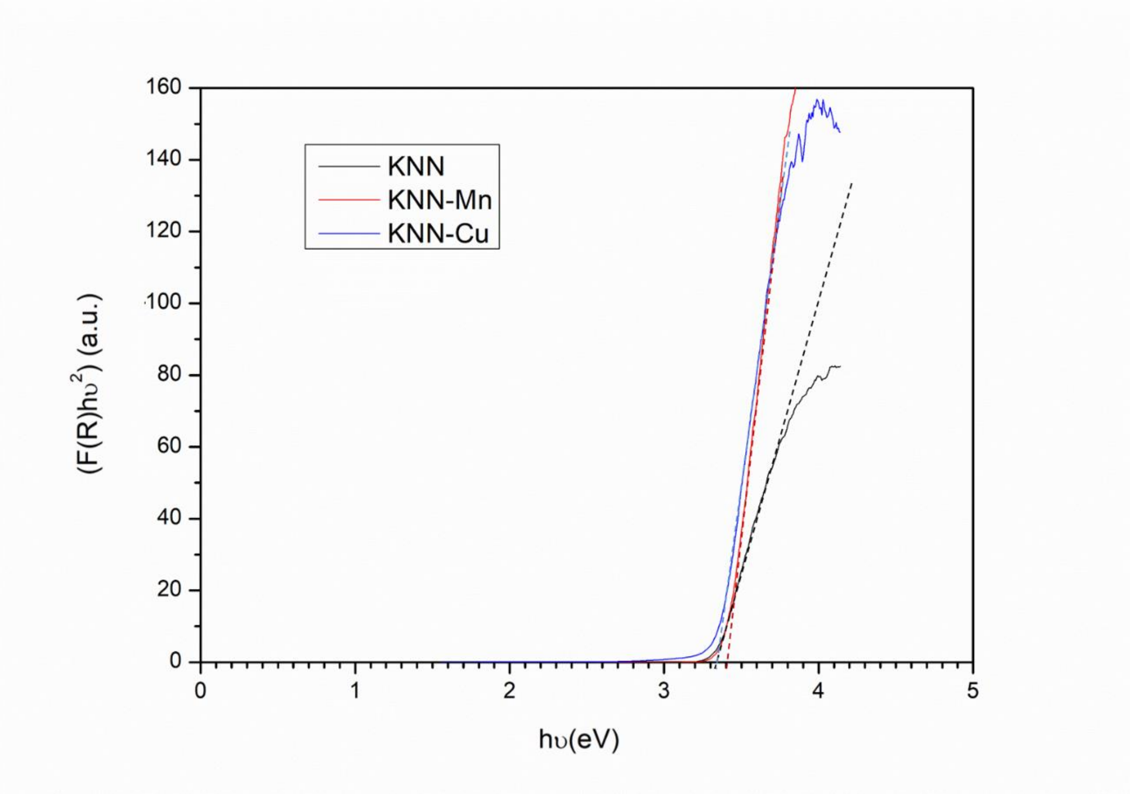

Figure 3.12 Tauc's plot for direct bandgap estimation obtained using diffuse reflectance spectra data.

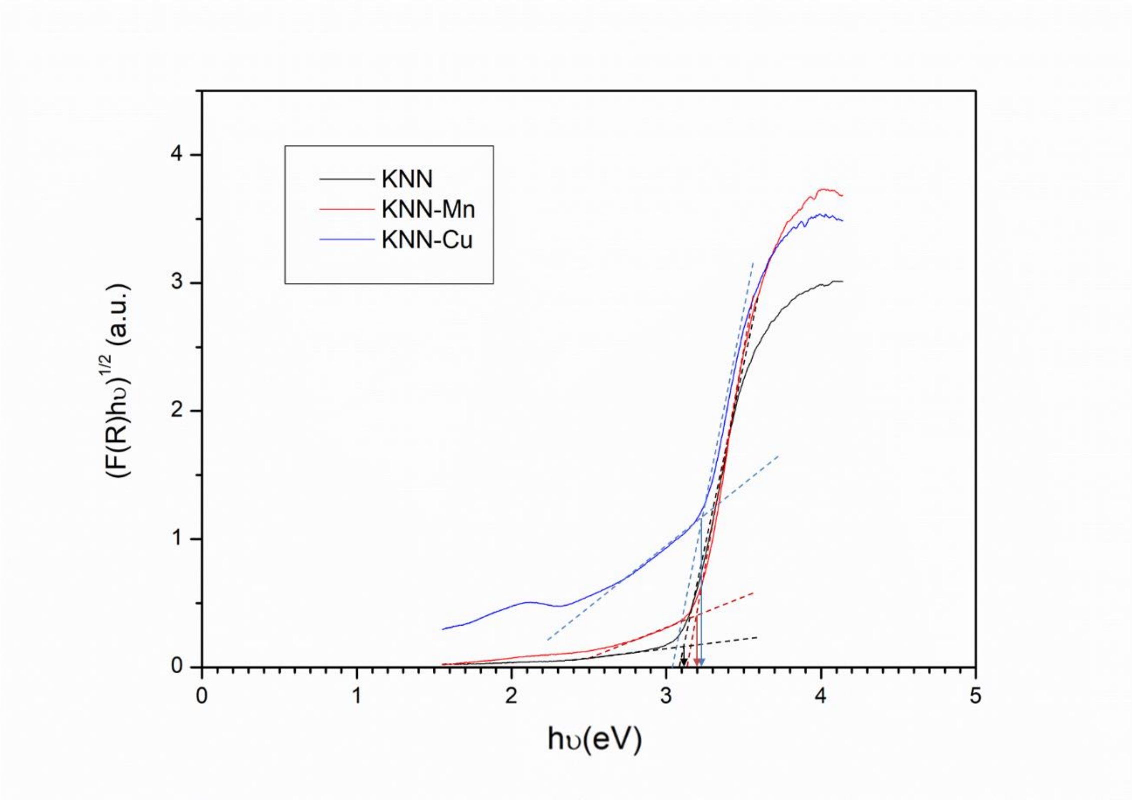

Figure 3.13 Tauc's plot for indirect bandgap estimation obtained using diffuse reflectance spectra data.

Table 3.2 Bandgap values of KNN, KNN-Mn and KNN-Cu estimated from the Tauc's plot obtained using diffuse reflectance spectra data

Sample	Direct Bandgap (eV)	Indirect Bandgap (eV)
KNN	3.34	3.13
KNN-Mn	3.41	3.22
KNN-Cu	3.35	3.26

The measured transmittance spectra for all the ceramics are shown in Figure 3.14. All the samples have been ground to around to a thickness of 80 μm and adhered to a thin glass using hot glue for the measurements. The transmittance spectrum of the thin glass with a layer of hot glue has been measured for deducting their effects from the overall transmittance spectra. Owing to the greenish dark color, the KNN-Cu ceramic is still opaque at a thickness of 80 μm, and thus giving relatively low transmittances in the visible range as shown in Figure 3.14. Consequently, the corresponding absorption edge cannot be clearly observed. In contrast, the transmittances of the KNN and KNN-Mn ceramics in the visible range are higher, and thus their absorption edges can be clearly observed at around 400 nm.

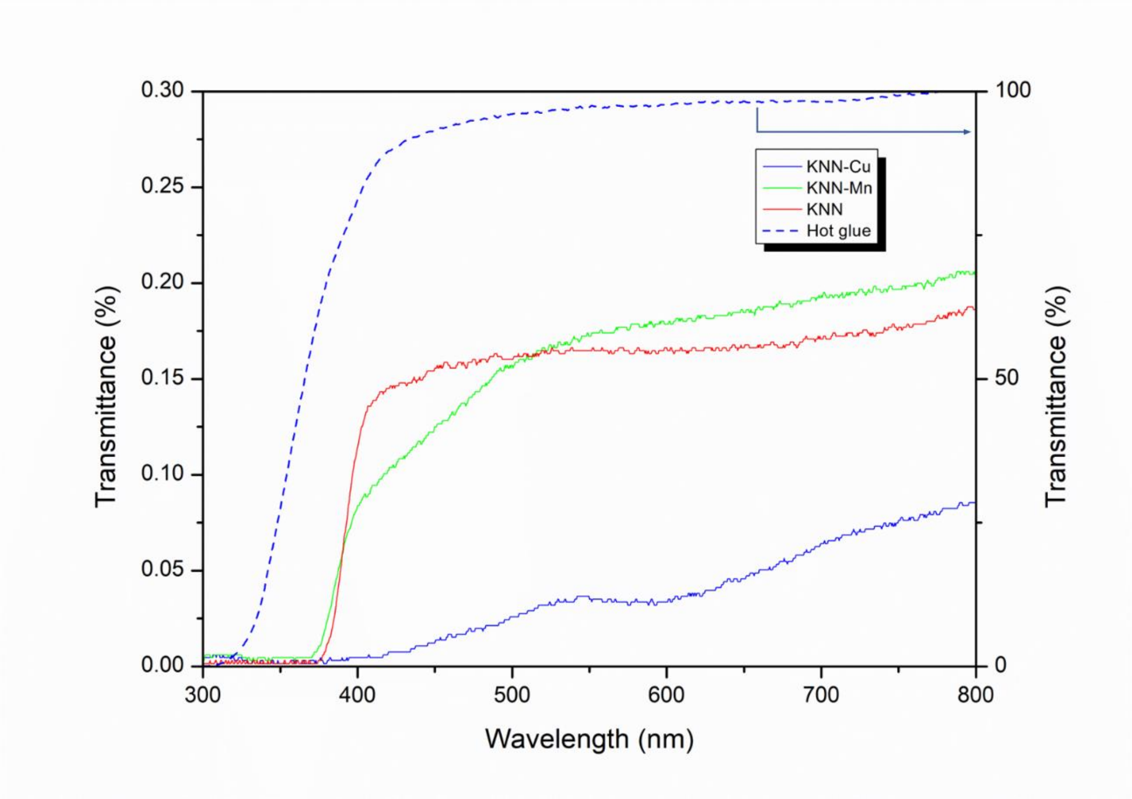

Figure 3.14 Transmittance spectra of KNN, KNN-Mn, and KNN-Cu

The Tauc's plots obtained from the transmittance spectra for the direct (n = 2) and indirect (n = 0.5) transitions are shown in Figure 3.15 and 3.16. As the absorption edge for the KNN-Cu ceramic is not clear, the linear fitting cannot be precisely conducted and thus no bandgap values are reported for it. The estimated bandgaps, both direct and indirect, for the KNN and KNN-Mn ceramics are listed in Table 3.3. The bandgap of the

KNN-Mn ceramic is larger than that of KNN, which is consistent with the results obtained from the diffuse reflectance spectra (Figs. 3.12). However, the estimated direct bandgaps for both samples are lower than those obtained from the diffuse reflectance spectra, while their indirect bandgaps are similar.

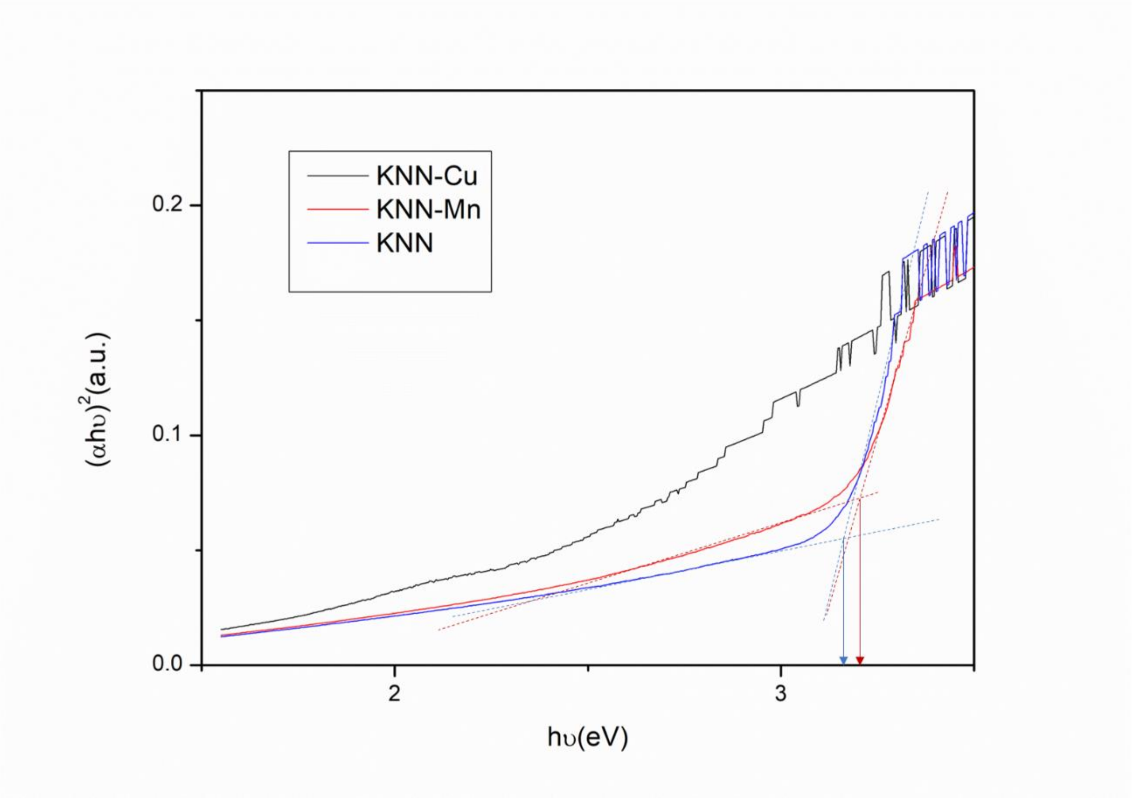

Figure 3.15 Tauc's plot for direct bandgap estimation obtained using transmittance spectra data

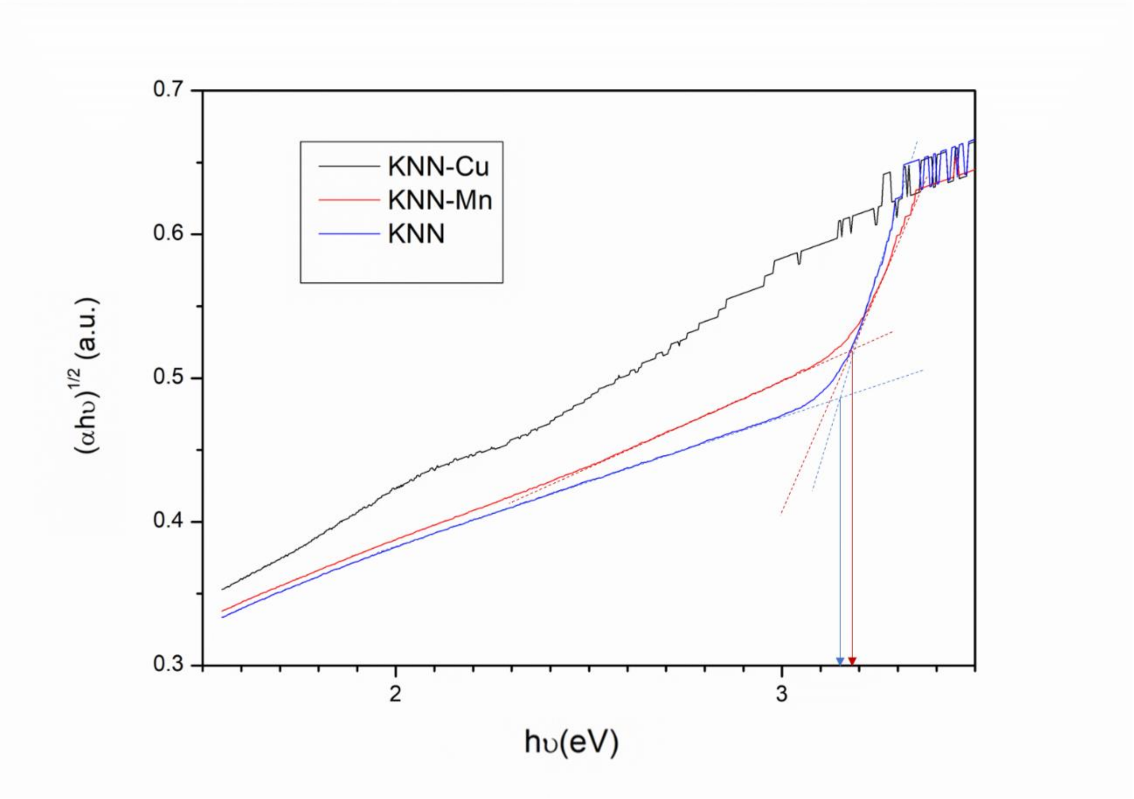

Figure 3.16 Tauc's plot for indirect bandgap estimation obtained using transmittance spectra data

Table 3.3 Bandgap values of KNN, KNN-Mn and KNN-Cu estimated from the Tauc's plot obtained using transmittance spectra data

	From Transmittance spectra		From Diffuse Reflectance spectra	
Sample	Direct Bandgap (eV)	Indirect Bandgap (eV)	Direct Bandgap (eV)	Indirect Bandgap (eV)
KNN	3.16	3.14	3.34	3.13
KNN-Mn	3.21	3.19	3.41	3.22
KNN-Cu	N/A	N/A	3.35	3.26

The transmittance of a sample is affected by its thickness. The transmittance spectra of the KNN ceramics with different thicknesses (33 µm, 47 µm and 88 µm) have then been measured for studying the effects on the estimation of bandgap. As shown in Figure 3.17, the transmittance at all wavelengths increases with decreasing thickness. As the thickness decreases, the total loss in scattering or absorption becomes lesser in the bulk and thus the transmittance is enhanced. The increase in transmittance is more significant for the the 33-µm thin sample. It may be attributed to the defects such as pores existed on the surface and inside of the bulk. Some of the pores are as large as 5-10 µm. Light beam may be diffracted through the sample via the pores, and the diffraction is more significant at longer wavelength. As a result, the transmittance is higher at longer wavelength for the 33-µm sample.

The Tauc's plot for the direct and indirect transitions are shown in Figure 3.18 and 3.19, respectively. It can be seen that the estimated bandgaps shift to higher energy as the thickness decreases. As the bandgap of a material should not be affected by its thickness, the change in bandgap should be resulted from the curve fitting.

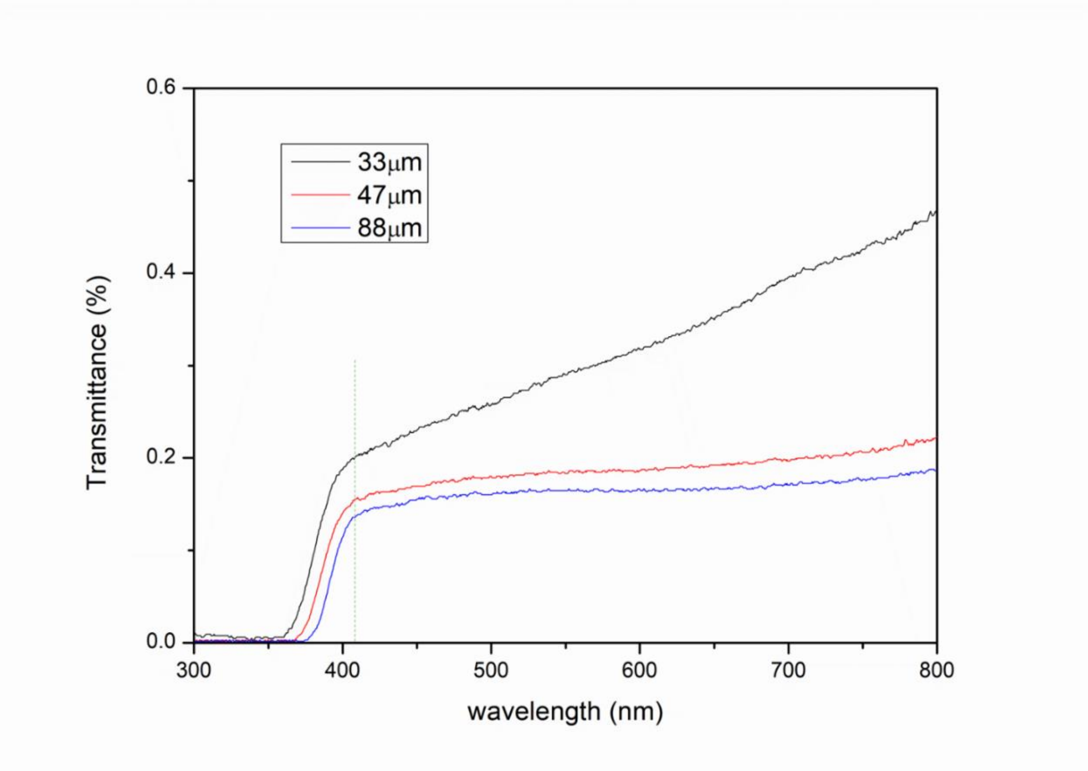

Figure 3.17 Transmittance spectra of KNN with different thickness

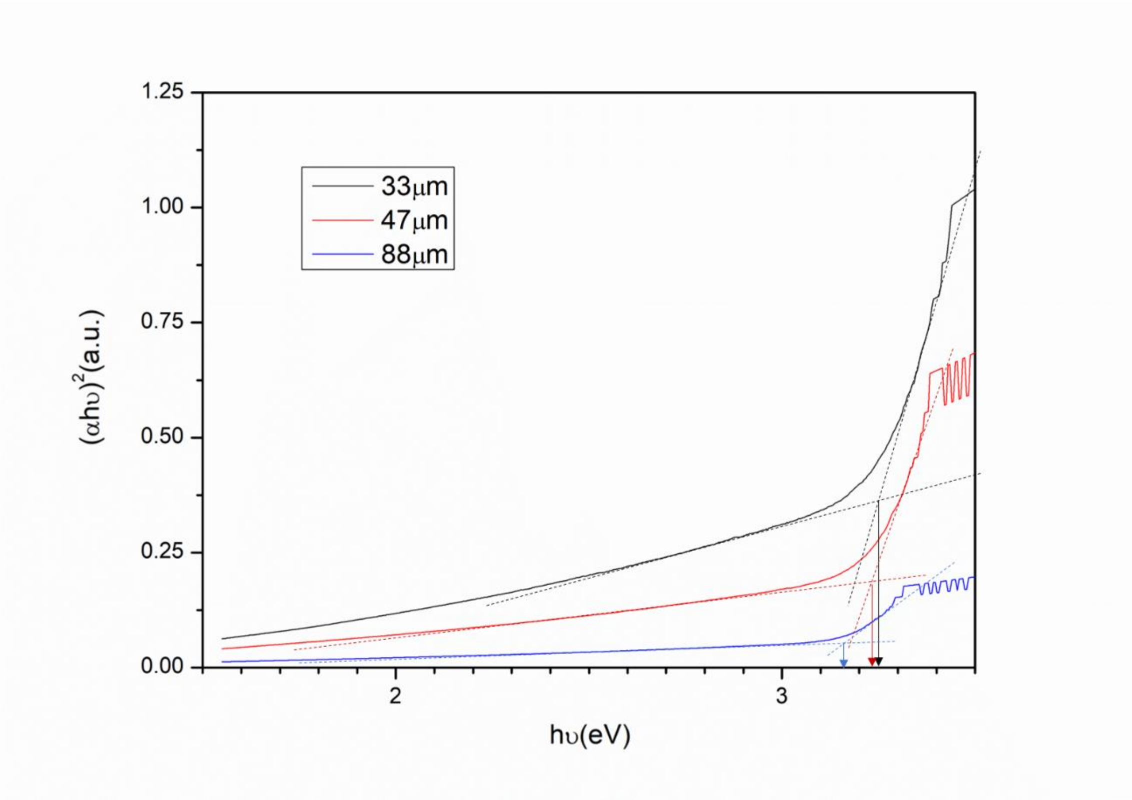

Figure 3.18 Tauc's plot for direct bandgap estimation for KNN in thickness obtained using transmittance spectra.

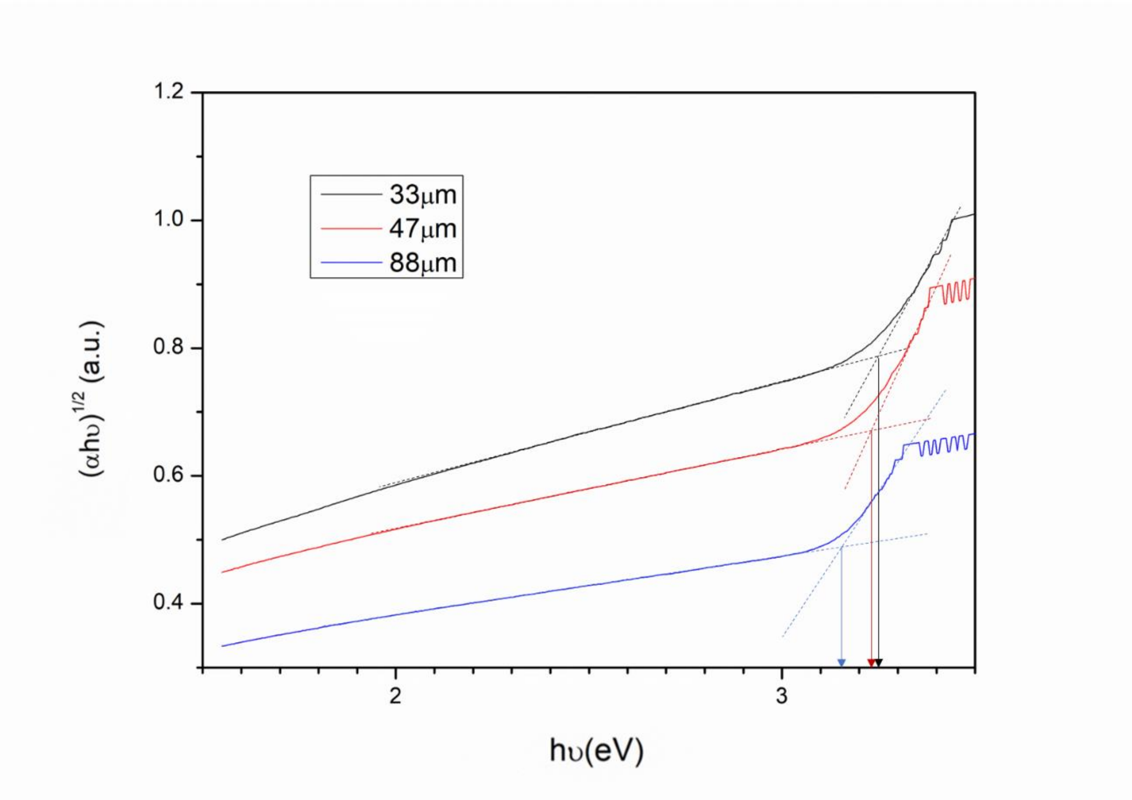

Figure 3.19 Tauc's plot for indirect bandgap estimation for KNN in thickness obtained using transmittance spectra.

Table 3.4 Bandgap values of KNN in different thickness estimated from the tauc's plot obtained using transmittance spectra data

Thickness of KNN	Direct Bandgap (eV)	Indirect Bandgap (eV)
33 μm	3.27	3.24
47 μm	3.23	3.21
88 μm	3.16	3.14

Our results show that the values of bandgap estimated using different methods are slightly different. Both methods have their own assumptions for the calculation and thus lead to the difference in the estimated bandgaps. For the transmittance method, it is assumed that the sample is highly transparent and thin enough to reduce the light path for high energy photons (the region where the sample exhibits strong absorption). And the energy loss of light beam should be mainly contributed to the absorption inside the bulk, instead of reflection, scattering or diffraction on the surface or at the grain interfaces. But owing to the poor density of KNN fabricated by the conventional method, the pores in the samples would be unavoidable. The Tauc's plot curve fitting may thus be affected, especially for thin samples. And for the diffuse reflectance method, it is assumed that the sample particles are highly light scattering and in sub-micron size to maximize the scattering efficiency. The diffuse reflected light passes through the powder and absorption may be occurred. It is similar to the transmittance method, but the light path in powder could be greatly reduced. Comparing to the transmittance method, in the region of strong absorption, because of the reduced light path, more detail could be shown in the diffuse reflectance spectra. However, in the region of weak absorption, it may result in stronger signal than the transmittance method [89, 90]. The curve fitting in tauc's plots obtained from the diffuse reflectance method is clearer than that obtained from transmittance method. However, the powders are not in sub-micron size, due to the technical limit, and it may have some effect on the curve fitting, i.e. the estimated bandgap. The effect of powder size on tauc's plot fitting is suggested to be further investigated.

3.5 Conclusion

KNN, KNN-Mn and KNN-Cu ceramics with a dense structure have successfully been fabricated by a conventional solid-state reaction method. In agreement with the other studies, MnO2 and CuO are effective in enhancing the densification of KNN, leading to a higher density in KNN-Mn and KNN-Cu.

As demonstrated by SEM micrographs, all the samples are dense and the grains are generally of rectangular shape. The grain sizes of KNN-Mn and KNN-Cu are 1.0 μm, which are smaller than that of KNN (1.4 μm). All the samples show a single-phase orthorhombic perovskite structure, suggesting that some of the Mn3+ and Cu2+ may have entered the KNN lattices and substituted the Nb5+ ions.

The optical properties of samples have been evaluated based on the diffuse reflectance and transmittance spectra. Tauc's plots have also been plot based on both spectra for estimating the bandgap of the samples. The direct bandgaps of KNN and KNN-Mn, both are 80 μm thick, estimated using the transmittance spectra are 3.16 eV and 3.21 eV, respectively, while their indirect bandgaps are 3.14 eV and 3.19 eV, respectively. On the other hand, the direct bandgaps of KNN, KNN-Mn and KNN-Cu estimated using the diffuse reflectance spectra are 3.34 eV, 3.41 eV and 3.35 eV, respectively, and their indirect bandgaps are 3.13 eV, 3.22 eV and 3.26 eV, respectively. The difference between the bandgaps estimated from the transmittance and diffuse reflectance spectra has also been discussed based on their theoretical assumptions.

Chapter 4 Ferroelectric Photovoltaic Measurement

4.1 Introduction

In this Chapter, the study of the short-circuit current, one of the ferroelectric photovoltaic properties, of the KNN and MnO_2/CuO-added KNN (KNN-Mn and KNN-Cu) ceramics are presented. The temperature effect and the origin of the short-circuit current is discussed. The feasibility of I-V characteristic measurement conducting on ferroelectric photovoltaic materials is discussed. First, the fabrication of devices is introduced. Then, the measurement method is described. Finally, the results and discussion are presented.

4.2 Device Fabrication and Measurement Setup

In recent years, the devices used in most of the research works are the sandwich-like device, of which electrodes are deposited on the top and bottom surfaces of a thin film sample. The output electrical signal is measured across the sample thickness. In this study, such the sandwich-like device is not practical as it is nearly impossible to obtain a few-micron thick device by the top-down method using bulk samples. Also, the thick sample does not favour the transmission of light and flow of electrons. Therefore, an interdigital electrode (IDE) device have been adopted for this study. Electrodes with inner gap distance as short as 10 μm are deposited on the top surface of a bulk sample using a conventional method. The schematic diagram of the IDE pattern used in this study is shown in Figure 4.1. a is the overlapped length of the electrodes, b is the gap distance and n is the number of gap. In this study, the parameter of the used IDE pattern are a = 5600 μm, b = 10 μm and n = 20.

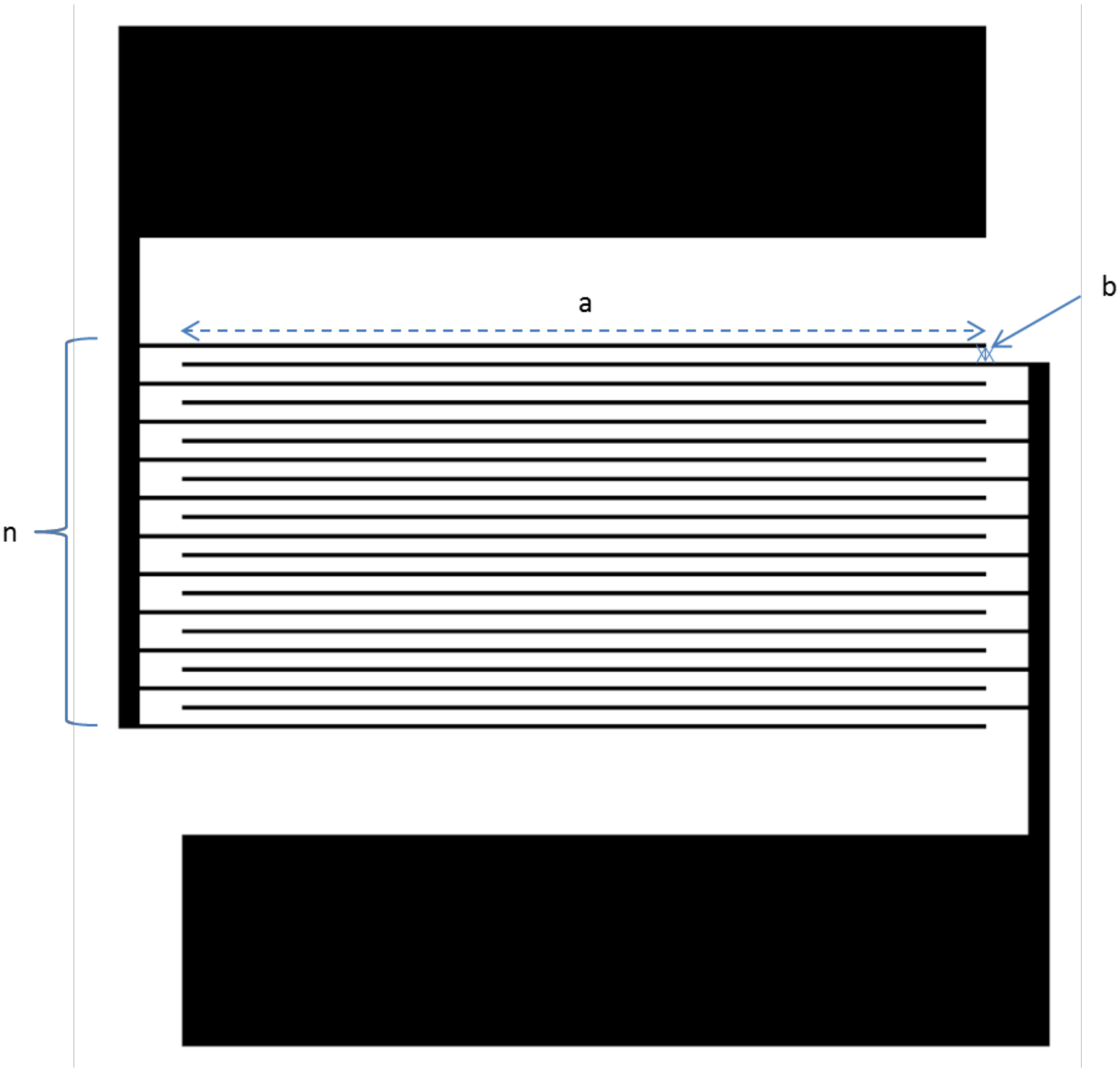

Figure 4.1 The schematic diagram of the IDE pattern used in this study

Photolithography

The as-sintered ceramic disc was first polished using 1-μm diamond lapping film until a mirror-like surface was obtained. The IDE pattern was then deposited on it by a conventional photolithography technique. First, a layer of positive photoresist was spin-coated on the mirror-like surface. Then, it was exposed to UV light under a mask with the designed pattern. After that, the exposed photoresist was removed by a developer, leaving a pattern (the white region in Figure 4.1) on the sample surface. Finally, Cr/Au was deposited on the sample by magnetron sputtering. After removing the remaining photoresist, a Cr/Au IDE pattern (the black lines in Figure 4.1) was obtained. Figure 4.2 shows the schematic diagram of the working procedures for the fabrication of the IDE pattern. The patterned sample was then adhered on a PCB board for the ease of handling in the subsequent measurements.

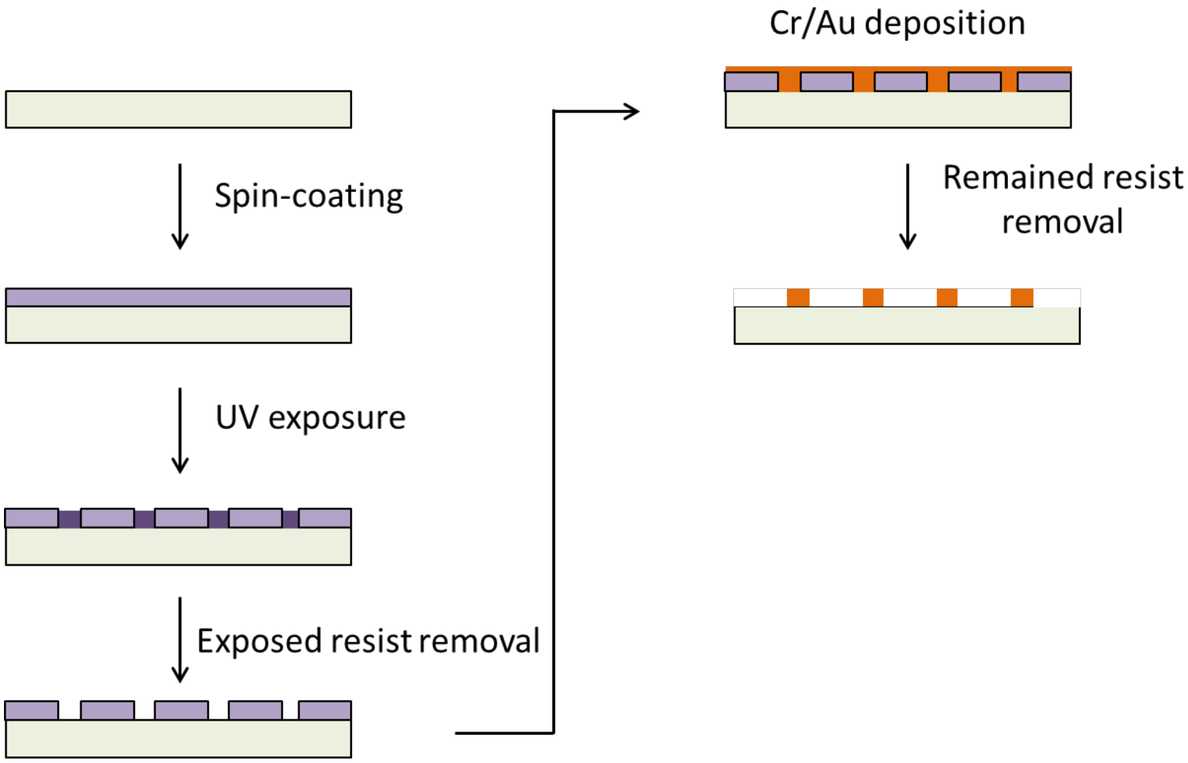

Figure 4.2 Schematic diagram of the working flow for the fabrication of Cr/Au IDE patterns

Poling

The poling setup is simpler than that used for poling the thick bulk samples. The IDE patterned sample was connected to a DC power supply. As the electrode gap distance is short, the required poling voltage is relatively low. Thus, no amplifier was needed for the poling. The schematic diagram for the poling setup is shown in Figure 4.3.

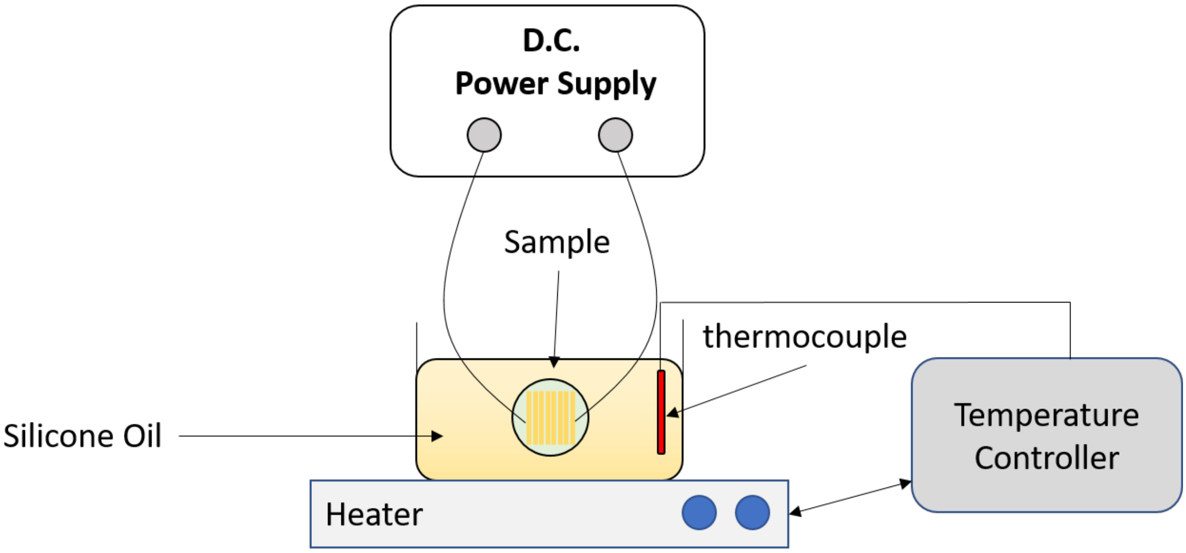

Figure 4.3 Schematic diagram of the poling setup for IDE patterned samples

Measurement setup

The schematic diagram of the measurement setup is shown in Figure 4.4. The electrodes on the IDE pattern were connected to a sourcemeter (Keithley 2410) and placed under a solar simulator (Newport) that was controlled by an attached power controller.

The measurements including the data collection were controlled by a computer programme written in LabView.

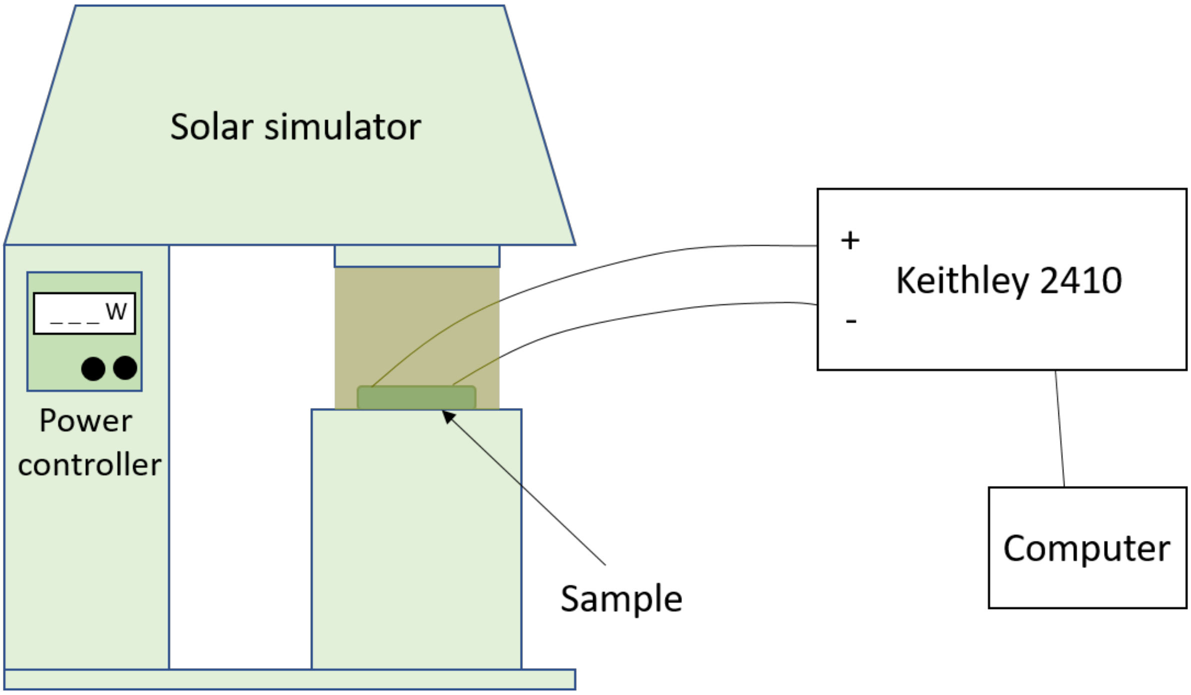

Figure 4.4 The schematic diagram of the setup for the photovoltaic measurements

4.3 Result and discussion

The Cr/Au IDE patterns have been successfully deposited on the fine-polished sample surfaces. Figure 4.5 shows a microscopic photography of the Cr/Au IDE pattern deposited on a KNN bulk sample. The electrode gap distance is 10 μm and the overlapped electrode length is 5600 μm.

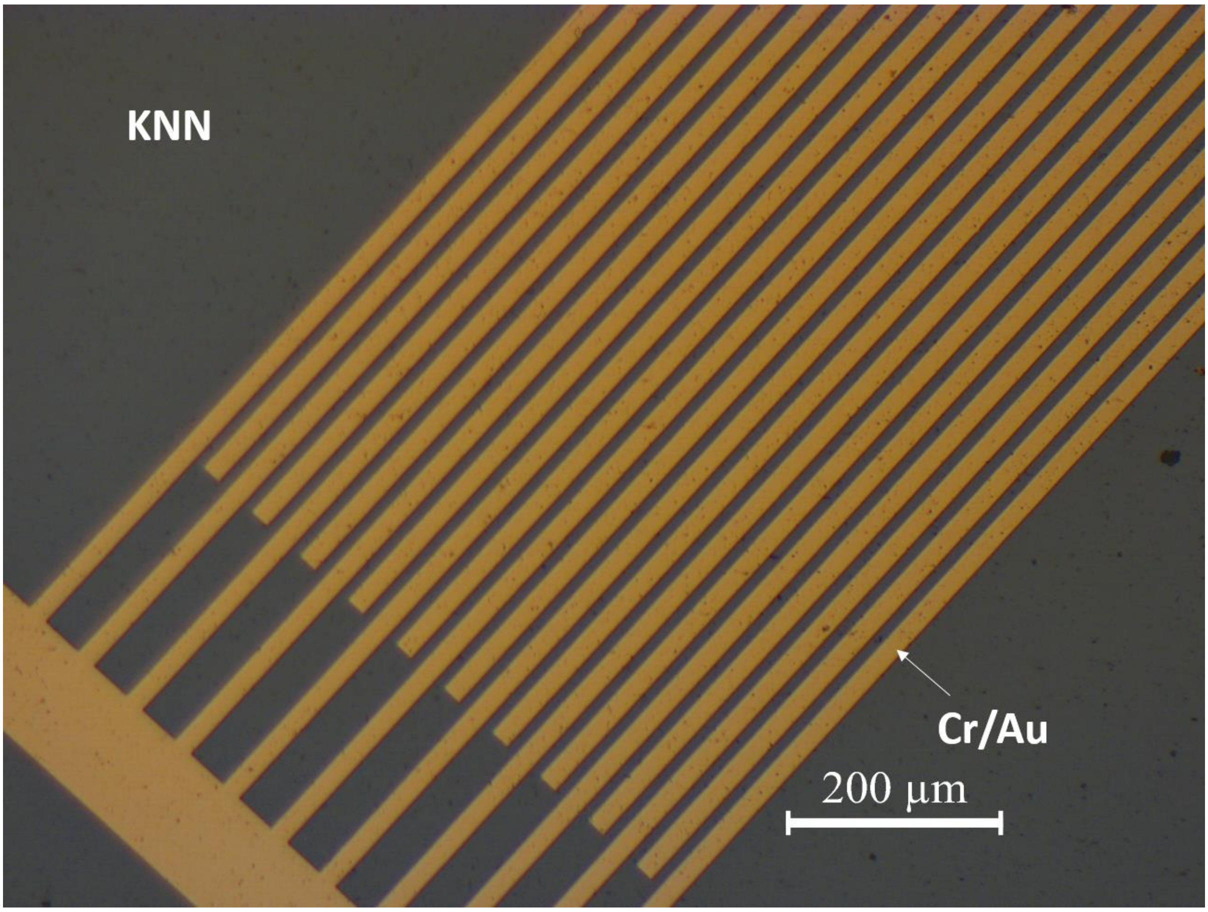

Figure 4.5 A microscopic photograph of the Cr/Au IDE pattern deposited on the surface of a KNN bulk sample

Photocurrent response of KNN

The photovoltaic response of the patterned KNN samples poled with different poling fields has been measured using a solar simulator (Newport) and a sourcemeter (Keithley 2410). The poled samples have been short circuited and stored in the dark for 1 day before the measurement. The short-circuit currents, I_{sc}, of the samples exposed to solar light with an intensity of 0.4 sun (or 40 $mWcm^{-2}$) are shown in Figure 4.6. The two dashed line indicate the duration of the illumination. The total illumination time is 20 minutes. As shown in Figure 4.6, the observed I_{sc} for the unpoled sample is 0 nA during the whole measurement. The net polarization of the sample is zero. Therefore, there is no driving force for separating and then drifting the photo-generated electrons and holes to different electrodes. Nevertheless, it indicated the thermal energy at room temperature in not sufficient to dissociate the excitons generated by above-bandgap photons. Apparently, because of the net polarization, the observed I_{sc} for the poled samples in enhanced and increases with the poling field (Fig. 4.6). It also indicated that the potential energy between the net polarization charges (which contribute to the depolarization field) and the photo-generated carrier is greater than the binding energy of the photo-generated exciton, the exciton, therefore, is dissociated and the electron is driven to the electrodes. As illustrated in Figure 4.7 in which the interdigital electrode (IDE) is simplified as a pair of parallel plates, a depolarization field is formed in the poled sample because of the (net) alignment of the spontaneous polarization. Under illumination, electron and hole pairs are produced by the photovoltaic effect, and separated and drifted by the depolarization field to different electrodes. The direction of the short-circuit current is opposite to the net polarization or the poling field, which is in agreement with our observation. Obviously, the higher the poling field, the larger the net polarization, and then the stronger the depolarization field is. As a result, although the light intensity and then the number of photo-generated electrons and holes are unchanged, the observed I_{sc} increases with the poling field because of the higher efficiency in separating and drifting the opposite charges. However, it is noted that the observed I_{sc} increases rapidly to a maximum value once the sample is illuminated, but it decreases gradually with time and becomes saturated afterwards. Nevertheless, the observed I_{sc} should be mainly resulted from the photovoltaic effect.

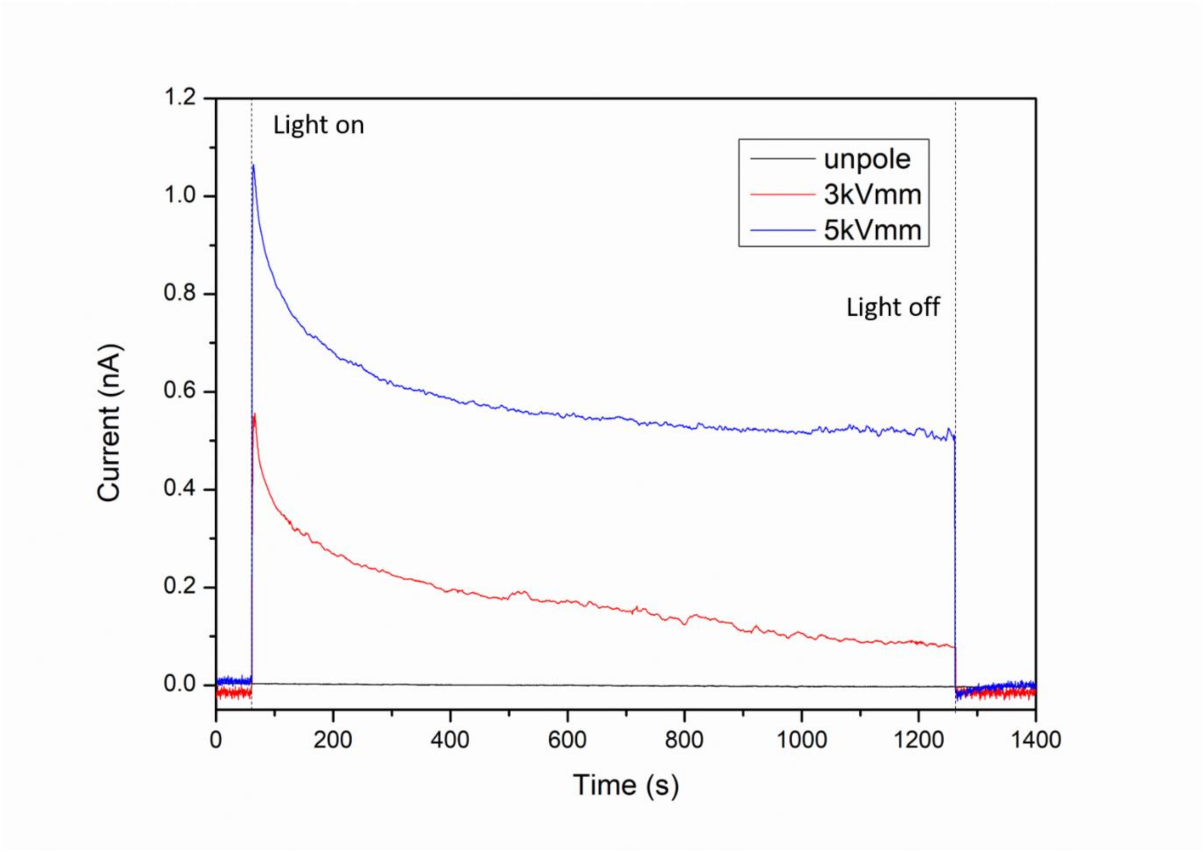

Figure 4.6 The photocurrent response of KNN after poling with different field

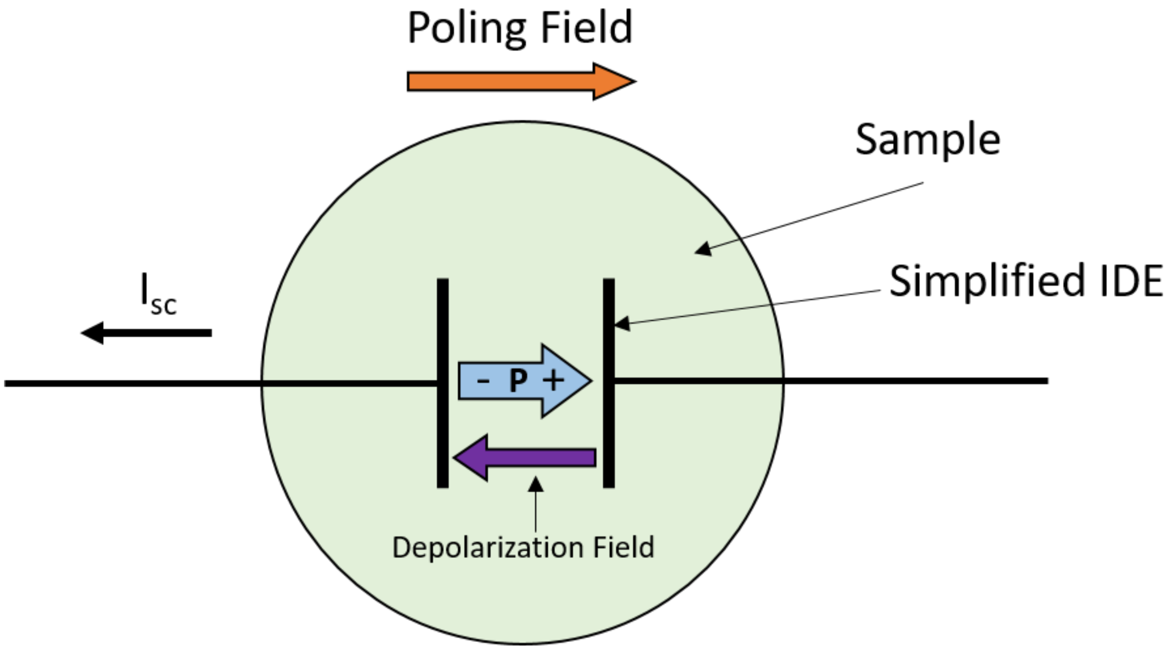

Figure 4.7 Illustration of the physical properties of the sample after poling.

For confirming the source of the observed I_{sc}, the photovoltaic response of the KNN sample poled with a field 5 kV/mm has been studied under different illumination conditions. Besides the data collected beyond the illumination period as shown in Figure 4.6, the sample also gives no current response when the illumination is switched off (Fig. 4.9). Moreover, a high-pass filter with a cut-off wavelength 420 nm has been used to adjust the illumination. The transmittance spectrum of the filter is shown in Figure 4.8. It exhibits a sharp edge at 420 nm, suggesting that it can effectively eliminate the light with wavelengths shorter than 420 nm. As the bandgap of KNN is measured to be 3.34 eV (Refer to Fig. 3.11), only the photons with wavelengths shorter than ~370 nm will be absorbed for producing the photovoltaic effect. Therefore, when the 420-nm filter is inserted in the light path for the measurement, almost all the photons with sufficient energy to excite the electrons in KNN are removed, and then no photo-generated electrons and holes are produced. As a result, the observed I_{sc} is greatly reduced to a level almost identical to that observed for without illumination as shown in Figure 4.9. This can thus deduce that the observed I_{sc}, including the decreasing trend with time, is mainly originated from the photo-generated electrons and holes or in other words, the photovoltaic effect.

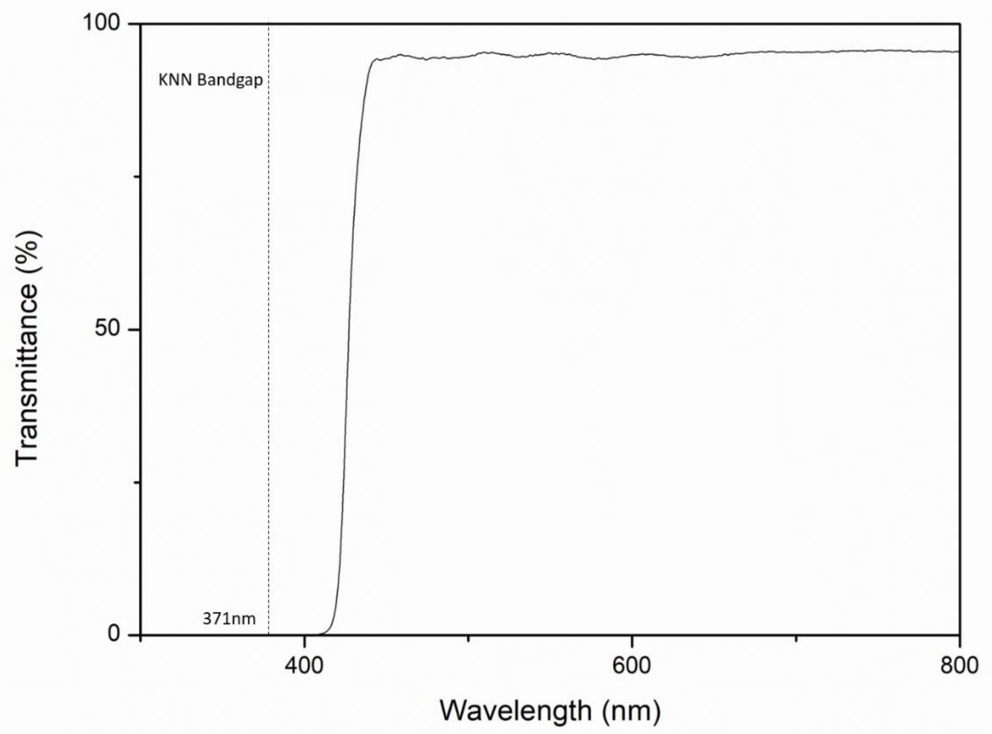

Figure 4.8 Transmittance spectrum of the 420-nm high pass filter

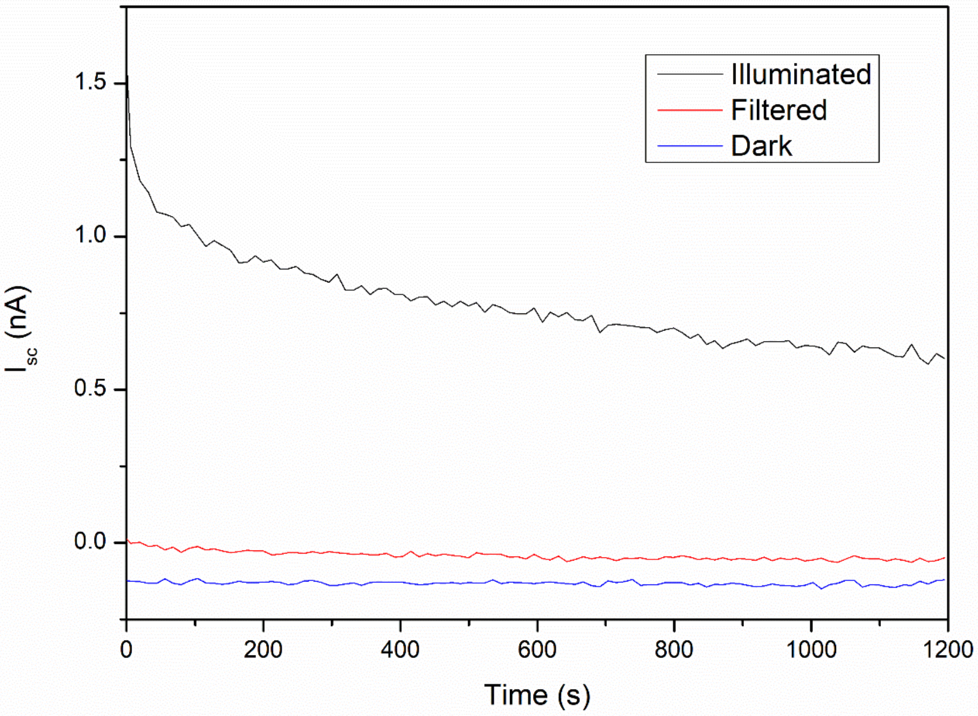

Figure 4.9 Short-circuit current measurement for 5kV/mm poled KNN with filtered illumination

The temperature effect on the observed I_{sc} has been studied for investigating the cause of the gradual decrease in the observed I_{sc}. A controlled experiment has been conducted for investigating the temperature change of the sample under illumination. The experiment setup is schematically shown in Figure 4.10. The sample is placed on a Peltier cooler, and a thermocouple is attached on the sample surface using silver paste for measuring the temperature during the illumination. Figure 4.11 shows the observed I_{sc} and temperature for the KNN sample poled with a field of 5 kV/mm. Similar to the previous results, the observed I_{sc} increases very rapidly to a maximum value once the illumination is switched on, and then decreases gradually with time. Meanwhile, the observed temperature also increases from room temperature (20°C) to ~30°C with similar trend, i.e., changes rapidly at first and then becomes slowly. This seemingly implies a relationship between them. However, when the Peltier cooler has been switched on for 1 minute with keeping the illumination on, the temperature decreases rapidly from 27°C to 13°C but the observed I_{sc} decreases only slightly (Fig. 4.11). Similarly, after the Peltier cooler is switched off, the sample temperature increases gradually back to 27°C and the observed I_{sc} increases only slightly. These clearly indicate that the observed I_{sc}, in particular its variation with time, is not contributed by the thermal effect.

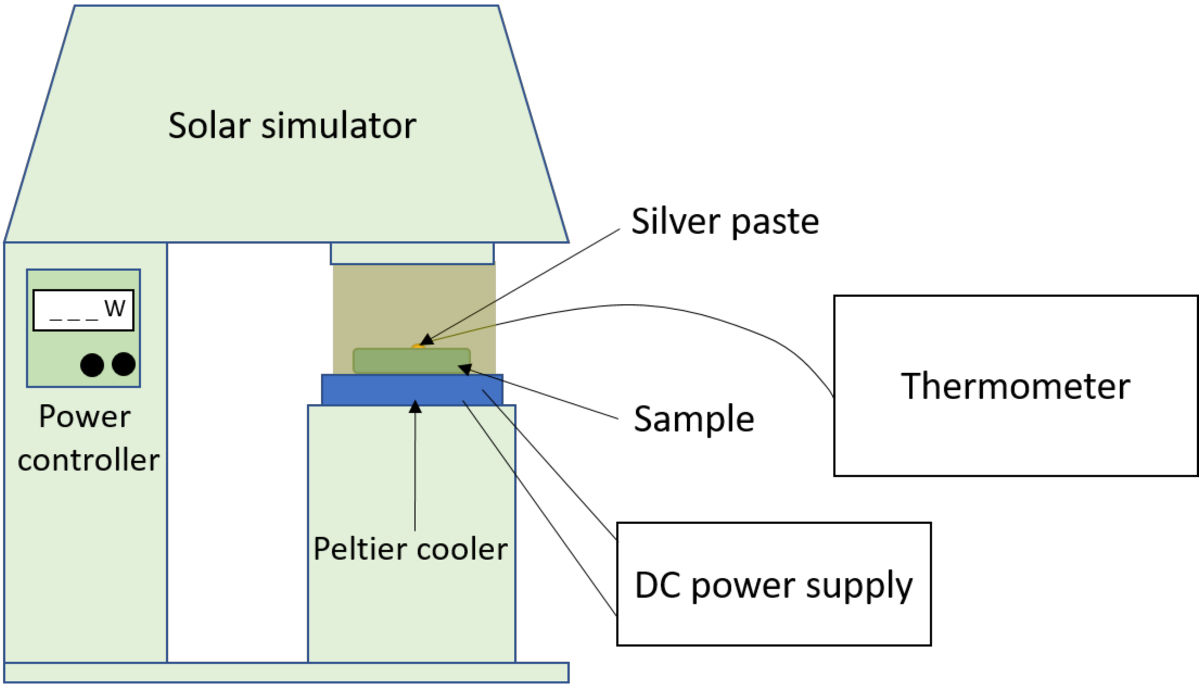

Figure 4.10 Experimental setup for temperature measurement during illumination

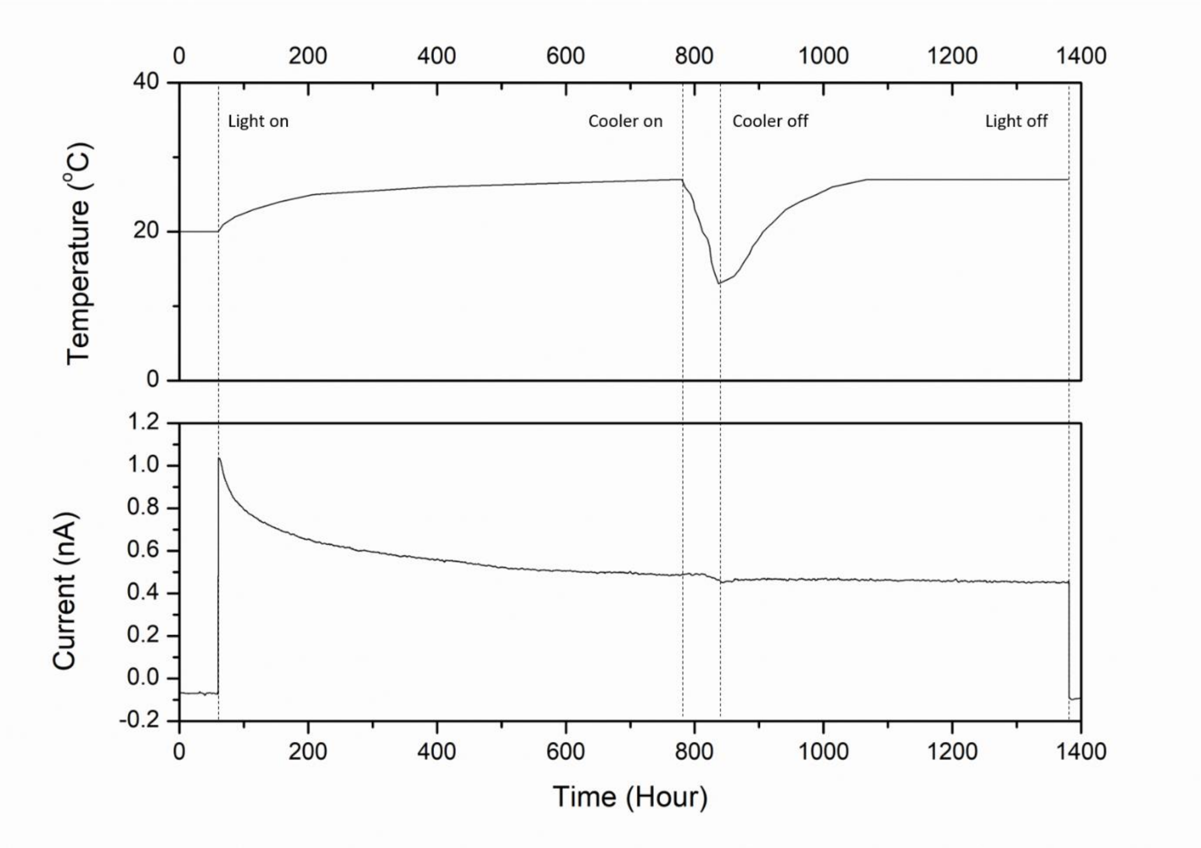

Figure 4.11 The 5kV/mm poled KNN was placed on a peltier cooler. The peltier cooler started cooling after 12 minutes illumination and stopped cooling after 1 minute. The temperature raised to original level in 3 minutes. The rapid drop in temperature induced an insignificant drop in short-circuit current

The repeatability of the observed photocurrent has then been evaluated. Before the measurement, the KNN sample (poled with a field of 5 kV/mm) has been short circuited and kept in the dark for a few days. In the measurement, the illumination is first switched on for 20 minutes and then off for 40 minutes. Such an illumination cycle is then repeated for five times. The observed I_{sc} as well as sample temperature are shown in Figure 4.12, in which the illumination periods are marked in yellow and the dark period are marked in grey for the ease of observation. Similar to the previous results, the observed I_{sc} increases rapidly at first and then decreases gradually while the sample temperature increases gradually to ~30°C in each illumination period. Once the illumination is switched off, the observed I_{sc} decreases almost instantaneously to zero whereas the sample temperature decreases gradually back to the room temperature, suggesting that the observed I_{sc} is mainly caused by the illumination. In the consecutive illumination cycles, the sample temperature exhibits almost the same variation with time, i.e., increases gradually to ~30C during the illumination-on period and then decreases back to room temperature after the illumination-off period. However, although the observed I_{sc} exhibits similar variations with time in each illumination-on period, it cannot reach the same maximum value that in fact decreases in the consecutive cycles. However, if the sample has been kept in the dark as well as short-circuited for longer time, e.g., 85 hours as illustrated in Figure 4.12, the observed I_{sc} can reach almost the same maximum value once the illumination is switched on. These indicate that the reduction in I_{sc} is reversible if the recovery time is long enough. These suggest that there should be effects other than photovoltaic effect contributing to the observed I_{sc}. Moreover, the response time of those effects should be rather slow as indicated by the gradual decrease and long recovery time of the observed I_{sc}. We thus propose that these should be attributed to the reduction in the depolarization field. During the illumination, the photo-generated electrons and holes (or charge carries) are separated and driven to the electrodes by the depolarization field. The charge carriers may temporarily be trapped and accumulate at the sample-electrode interfaces, slowly build up an electric field opposite to the depolarization field, and thus lowering the efficiency of driving the photo-generated charges to the electrodes. The release of the temporarily trapped charges is a very slow process, such that only a small portion of them is released during the 40-minute illumination-off period and it takes a long period of 85 hours to release all of them. As a result, the observed I_{sc} reaches almost the same level again once the sample is illuminated.

Similar phenomenon has been reported by Park et al. [91]. However, they have not investigated the reversibility of the process.

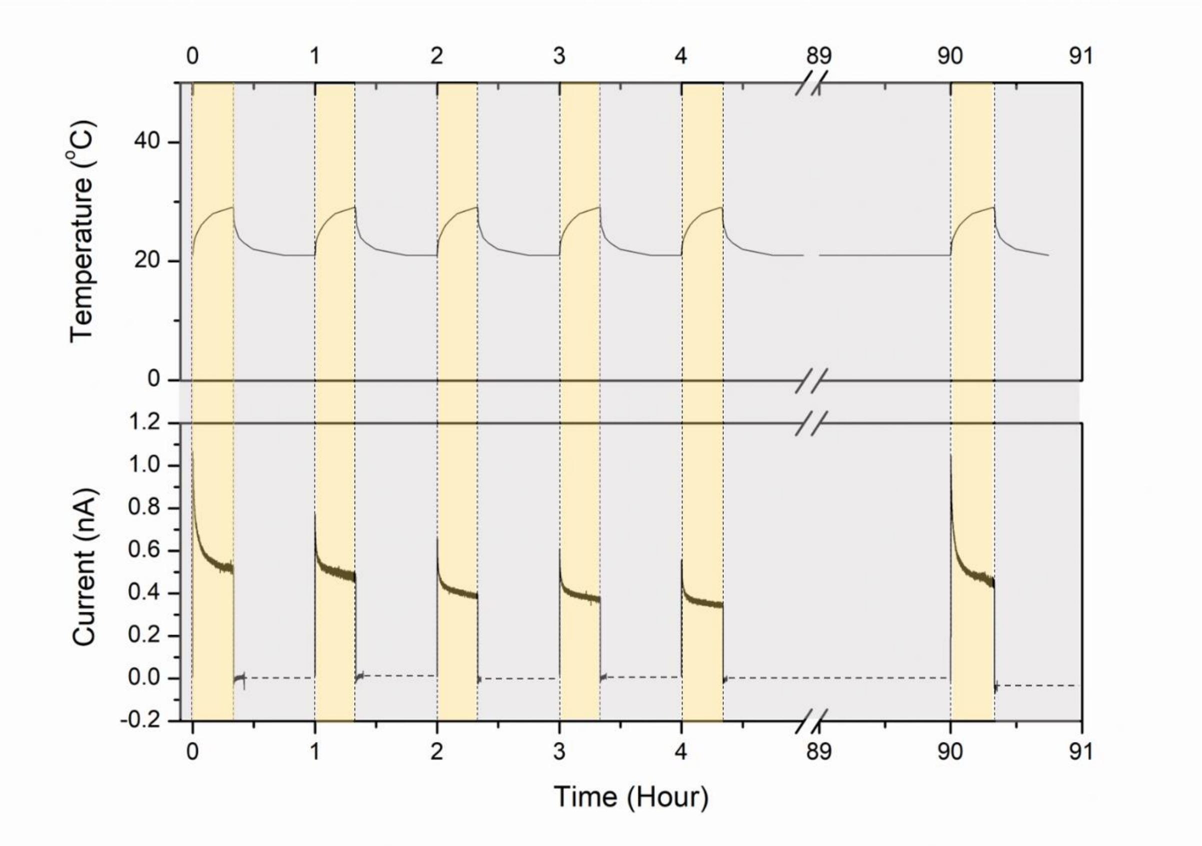

Figure 4.12 The I_{sc} of 5kV/mm poled KNN, the temperature was 21 °C at the beginning of each 20-minute illumination cycle. During the whole measurement, the sample was in short-circuit condition. The I_{sc} in the first 5 hours of meausrement was gradually weakening. The I_{sc} was recovered after resting in dark and short-circuit condition for 85 hours.

Photocurrent response of KNN-Cu and KNN-Mn

The photocurrent responses of the KNN-Mn and KNN-Cu ceramics deposited with the same IDE pattern have been studied. However, as the IDE patterns become partially damaged when a poling field higher than 3 kV/mm is applied, the photocurrents of both the ceramics poled with a field of 3 kV/mm have only been measured, giving the results shown in Figure 4.13 and Figure 4.14, respectively. Both the poled ceramic samples have been short circuited and kept in the dark for one day before the measurements. Similar to KNN, the observed I_{sc} for both the ceramic samples exhibit similar variations with time, i.e., reach a maximum value once the illumination is switched on and then decrease gradually with time. However, their maximum values are much lower than that of KNN, only about 30% (Fig. 4.15).

However, it is interesting to note that the observed I_{sc} for all the three ceramics saturate at almost the same level, ~0.8 nA (Fig. 4.15). Also, the I_{sc} of KNN-Mn and KNN-Cu reach the saturate level much earlier than that of KNN. The I_{sc} measured before the saturation may be attributed to effects other than photovoltaic effect. KNN has been known as defective ferroelectric perovskites, owing to the high volatilities of Na and K [92]. The doping of Mn and Cu have been shown effective for improving the densification of KNN. The defect density in KNN should thus be higher than those of KNN-Mn and KNN-Cu. When the sample is short-circuited and stored in the dark, the defects may temporarily be charged up. Under the illumination, the charges are excited and released slowly, and thus contributing to the observed I_{sc}. After the release of most of the trapped charges, the observed I_{sc} becomes saturated and reaches a level similar to those for KNN-Mn and KNN-Cu. As all the three ceramics have similar bandgaps, the saturated I_{sc} should then reflect to the photovoltaic effect. More investigation are needed to further understand the phenomenon.

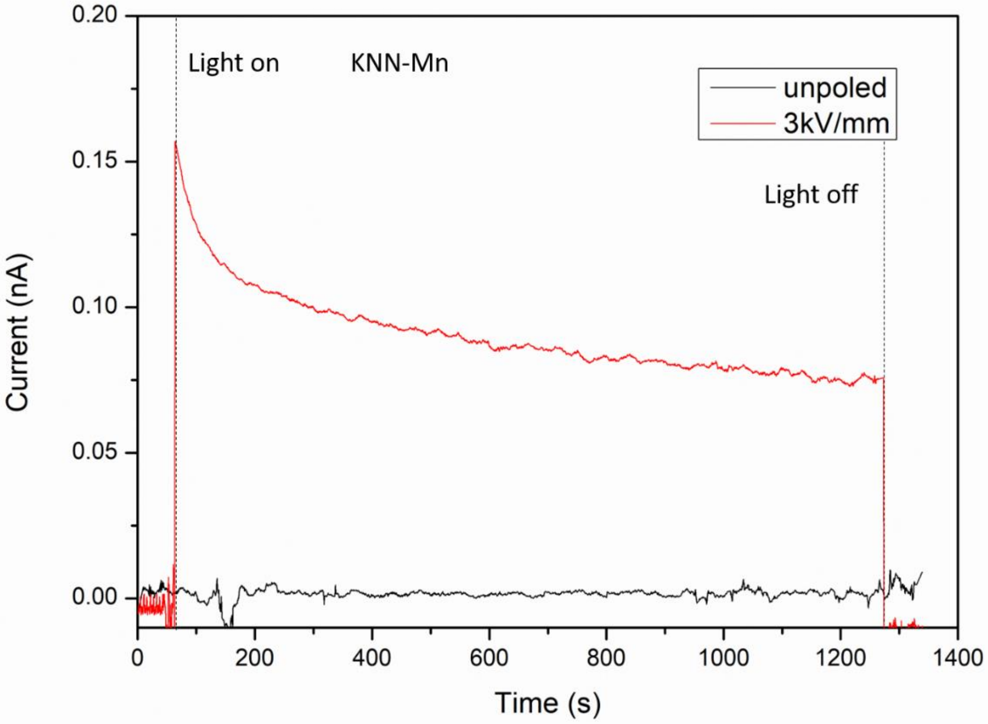

Figure 4.13 The photocurrent response of KNN-Mn.

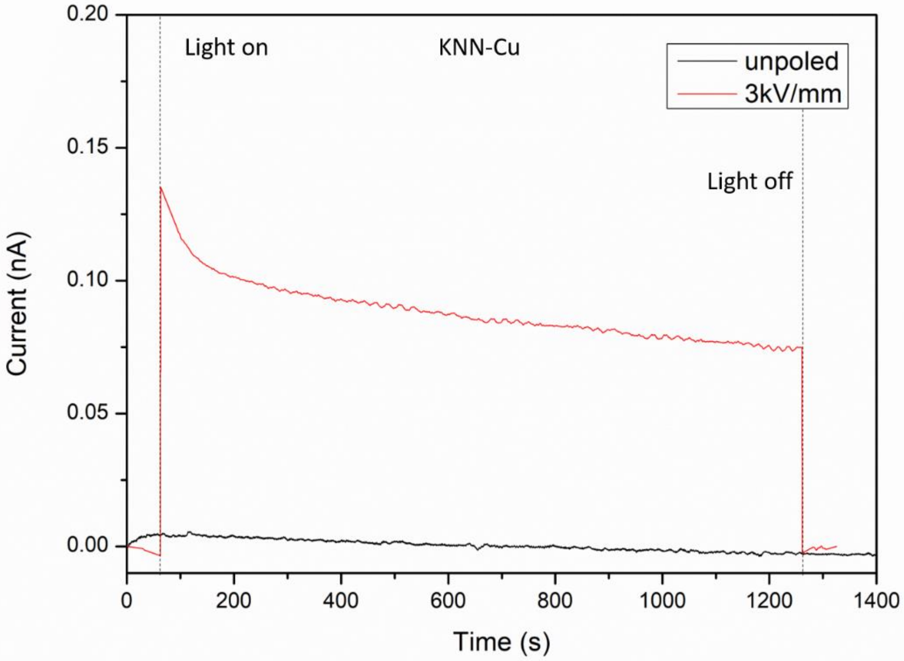

Figure 4.14 The photocurrent response of KNN-Cu

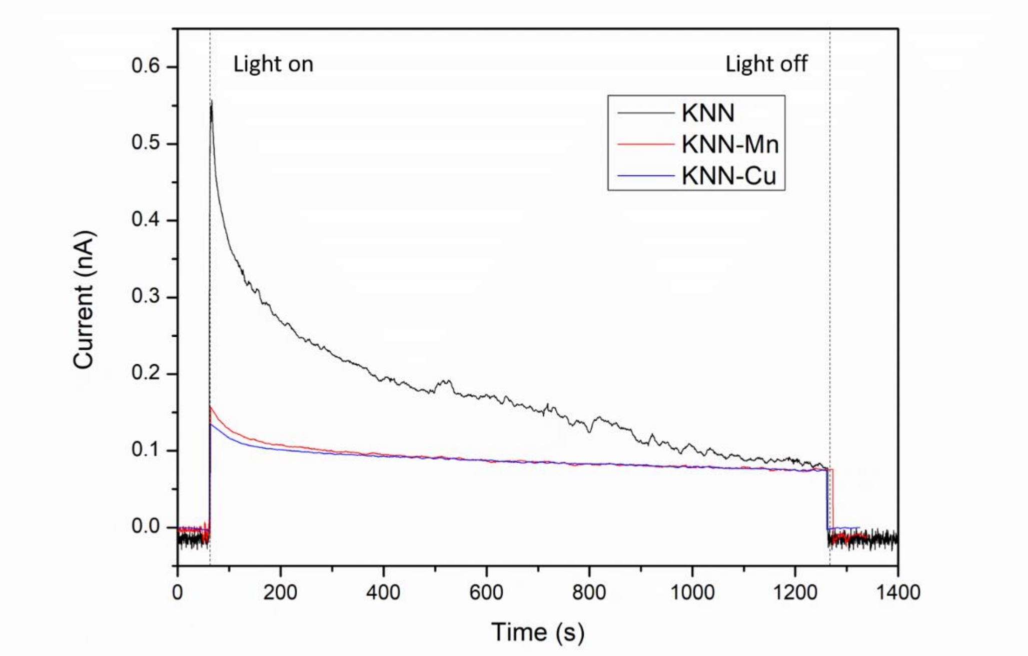

Figure 4.15 The photocurrent response of KNN, KNN-Mn and KNN-Cu, all the samples were poled with 3kV/mm and have been placed in dark and short-circuit condition for one day before measurement.

Discussion on IV characteristic measurement

The IV characteristic (or IV curve) is one of the typical measurements for characterising the common semiconductor-based solar cells. A number of characteristics, such as the short-circuit current, open-circuit voltage and fill factor, which is related to the power conversion efficiency of the device, can be determined from the IV curve. A typical IV curve of a semiconductor solar cell is shown in Figure 4.16.

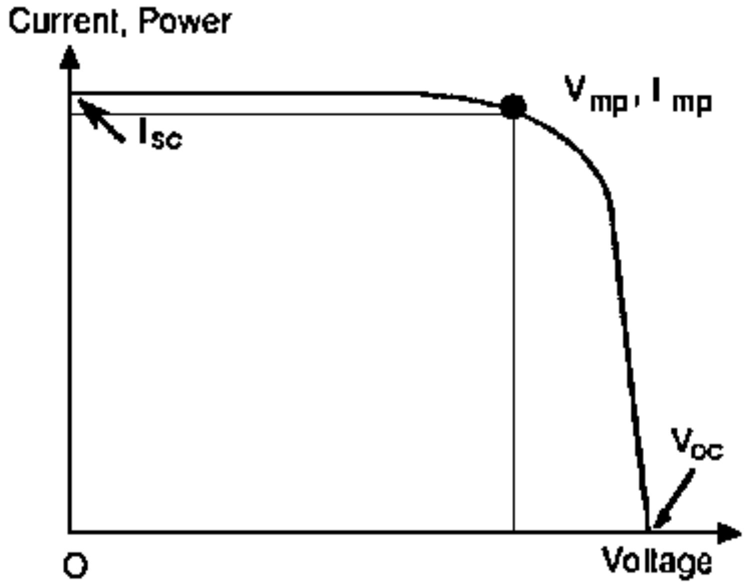

Figure 4.16 A typical IV curve of a semiconductor solar cell. I_{sc} *is the short-circuit current,* V_{oc} *is the open-circuit voltage,* V_{mp} *and* I_{mp} *are the voltage and current at maximum generated power. The fill factor is defined as* $(V_{mp}I_{mp}/I_{sc}V_{oc})$

The IV curve has also been used for studying the ferroelectric photovoltaic effect in most of the publications. However, the observed IV curve is quite different from that for the semiconductor solar cell, making the determination of I_{sc} and V_{oc} becomes ambiguous. Figure 4.17 shows the IV curve for the KNN sample poled with a field of 5 kV/mm. In the measurement, an AC voltage with an amplitude of 50 mV sweeping first to the positive direction has been applied to the sample. As shown in Figure 4.17, a loop instead of a single curve is observed for the sample. The amplitude of the ac voltage for the measurement is only about 0.5% of the coercive field. Therefore, the observed variations of I_{sc} and V_{oc} should not be caused by the change in polarization. These may be attributed to the charging and discharging of its capacitor or trapping of charges by defects. More in-depth investigations are needed for further understanding the phenomena. It has also been noted that the sweeping direction of the ac voltage can change the values of I_{sc} and V_{oc}. Larger values are generally observed when the ac voltage is first sweeping to the positive direction. Unfortunately, the sweeping direction of the ac voltage has not been mentioned in most of the publications studying the ferroelectric photovoltaic effect [12, 13, 17, 21, 22, 93-97]. Because of these ambiguities, it is then not proper to determine the values of I_{sc} and V_{oc}, let alone determining the efficiency of the device. Nevertheless, based on the above results and discussions, the photovoltaic effect has been confirmed in the ferroelectric KNN ceramics.

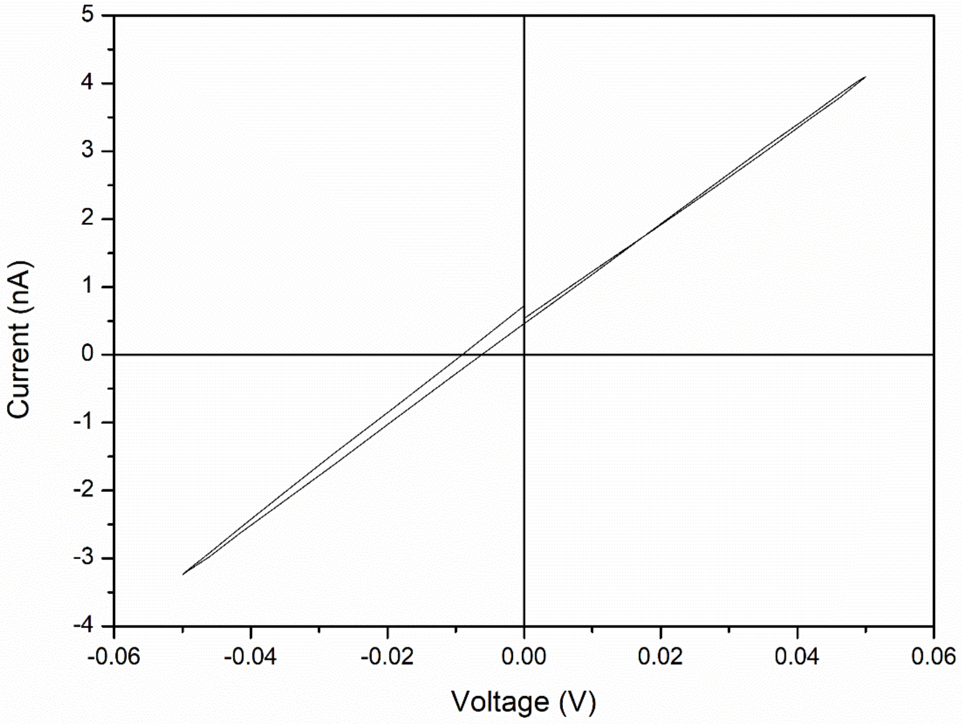

Figure 4.17 IV curve of 5kV/mm poled KNN. A sine voltage with 50 mV amplitude was applied.

4.4 Conclusion

The photovoltaic effect of ferroelectric KNN ceramics has been demonstrated. The short-circuit current has been studied. For the KNN ceramic poled with a field of 5 kV/mm, the observed I_{sc} is 1.1 nA at the beginning of a sunlight illumination with an intensity of 40 mW/cm^2. It then decreases gradually and saturates at a level of 0.5 nA after 10 minutes. The observed I_{sc} has been confirmed to be induced by the incident photons with energies larger than the bandgap or the photovoltaic effect. Based on the results of the sample temperatures, the decrease in I_{sc} is concluded not contributed by the change in temperature arisen from the illumination. It is suggested to be due to the weakening of the depolarization field by the trapped charges at the sample-electrode interfaces. Moreover, the decrease in I_{sc} has been shown as a reversible process despite requiring a long recovery period during which the sample is short circuited and kept in the dark.

The photovoltaic effect has also been demonstrated in poled KNN-Mn and KNN-Cu ceramics. Because of the inferior quality of the IDE, both the ceramics can only be partially polarized with a poling field of 3 kV/mm. The observed I_{sc} for the ceramics exhibit similar variations with time, but of lower values as compared to KNN. The greater I_{sc} of KNN is suggested to be attributed to the higher concentration of oxygen vacancies. Charges may temporarily be trapped in the defects during the storage in the dark. Under the illumination, the trapped charges are excited and released slowing, and thus contributing to the observed I_{sc}. After the release of most of the trapped charges, the I_{sc} becomes saturated and reaches a level similar to those for KNN-Mn and KNN-Cu. As all the ceramics have similar bandgaps, the saturated I_{sc} should then reflect to the photovoltaic effect. More investigation is needed to further understand the phenomenon.

Chapter 5 Conclusion

$K_{0.5}Na_{0.5}NbO_3$ (KNN) ceramics and KNN ceramics doped with 0.25 mol% MnO_2 (KNN-Mn) or 1 mol% CuO (KNN-Cu) have been successfully fabricated using a solid-state reaction method. Their optical properties have been studied via transmittance and diffuse reflectance spectra. Their dielectric, piezoelectric and ferroelectric properties have also been studied, while the ferroelectric photovoltaic effect has been demonstrated and studied.

It has been found that all the samples possess a dense structure. As demonstrated by SEM micrographs, the average grain size of the ceramic is reduced from 1.4 μm to 1 μm after the doping of MnO_2 or CuO. All the samples also exhibit a single-phase orthorhombic structure, as revealed by the XRD patterns. The bandgap of the samples has been estimated from the transmittance and diffuse reflectance spectra based on Tauc's relation. Our results reveal that the bandgap of KNN-Mn is slightly larger than that of KNN. It is suggested that the increase in bandgap is attributed to the increase in the electronegativity difference between the B-site ions and oxygen after the substitution of Mn^{3+} to the B-site Nb^{5+}. The bandgap of KNN-Cu is similar to that of KNN, suggesting that the CuO additive has no significant improvement on optical properties. The direct bandgaps of KNN and KNN-Mn, both are 80 μm thick, estimated from the transmittance spectra are 3.16 eV and 3.21 eV, respectively, while their indirect bandgaps are 3.14 eV and 3.19 eV, respectively. On the other hand, the direct bandgaps of KNN, KNN-Mn and KNN-Cu estimated from the diffuse reflectance spectra are 3.34 eV, 3.41 eV and 3.35 eV, respectively, and their indirect bandgaps are 3.13 eV, 3.22 eV and 3.26 eV, respectively. The difference between the bandgaps estimated from the transmittance and diffuse reflectance spectra has been discussed based on their theoretical assumptions.

The ferroelectric photovoltaic responses of the samples have been studied by using solar simulator. For the KNN sample poled with a field of 5 kV/mm, the observed short-circuit current I_{sc} under an illumination of 40 mW/cm^2 is suggested to be originated form the electron-hole pairs excited by higher-than-bandgap photons and driven by the internal field (i.e. depolarization field). As expected, the observed I_{sc} increases with the poling field. It is suggested that the larger net polarization leads to a stronger depolarization field, which imposes a stronger effect on separating and drifting the photo-generated charges. However, it is noted that the observed I_{sc} decreases gradually with time after reaching a maximum value at the beginning of the illumination and becomes saturated afterwards. As confirmed by a controlled experiment, the decrease in I_{sc} during the illumination is not contributed by the thermal effect. The repeatability of the I_{sc} has been evaluated. It has been found that the observed I_{sc} exhibits similar variations with time in each cycle that consists of 20-min illumination and then 40-min darkness, but decreases slightly in the consecutive cycles. However, after keeping the sample short-circuited and in the dark for a long time (e.g., 85 hours), the I_{sc} increases and reaches almost the same maximum level as in the first illumination cycle, suggesting that the reduction in I_{sc} is reversible. Charged carriers may temporarily be trapped at the sample-electrode interfaces during the illumination, and thus weakening the depolarization field and then reducing the I_{sc}. The release of the temporarily trapped charges is a very slow process that requires a long period (e.g. 85 hours) for the completion.

The short-circuit photocurrent of KNN-Mn and KNN-Cu have also been studied and compared with that of KNN. Owing to the poor quality, the samples are only poled by a weaker field of 3 kV/mm. The observed I_{sc} for both ceramic samples exhibit similar variations with time as KNN, but their maximum values are about 30% lower than that of KNN. Nevertheless, the I_{sc} for all the three samples saturate at almost the same level, ~0.8 nA. The time required for the saturation is much longer in KNN as compared to KNN-Mn and KNN-Cu. It may be attributed to effect other than photovoltaic effect. KNN has higher defect density than KNN-Mn and KNN-Cu. The defects may temporarily be charged up when the sample is stored short-circuit and in the dark. Under the illumination, the trapped charges are excited and released slowly, and thus contributing to the observed I_{sc} in particular for the beginning of the illumination. It is suggested that, based on the similar bandgaps, the saturated Isc is mainly contributed by the photovoltaic effect.

The ferroelectric photovoltaic effect on KNN, KNN-Mn and KNN-Cu has been successfully demonstrated. For the future work, it is suggested to improve the optical properties (i.e. reducing the bandgap) of KNN via the doping of different types of dopants or other methods. By reducing the bandgap, the number of photo-excited electron-hole pairs would be increased and the photovoltaic response would thus be enhanced. Since KNN has been shown as a promising candidate for replacing the lead-based perovskites, studying the photovoltaic effect of it may open a window for it to become a multifunctional perovskite oxide.

Reference

[1] J. Curie and P. Curie, "Développement, par pression, de l'électricité polaire dans les cristaux hémièdres à faces inclinées," *Comptes rendus,* vol. 91, pp. 294-295, 1880.

[2] J. Valasek, "Piezo-electric and allied phenomena in Rochelle salt," *Physical review,* vol. 17, p. 475, 1921.

[3] S.-Y. Wu, "A new ferroelectric memory device, metal-ferroelectric-semiconductor transistor," *IEEE Transactions on Electron Devices,* vol. 21, pp. 499-504, 1974.

[4] S. Boyn, S. Girod, V. Garcia, S. Fusil, S. Xavier, C. Deranlot*, et al.*, "High-performance ferroelectric memory based on fully patterned tunnel junctions," *Applied Physics Letters,* vol. 104, p. 052909, 2014.

[5] S. Mohammadi, A. Khodayari, and P. Mohammadi, "Performance enhancement of cylindrical ferroelectric transducers," *Ceramics International,* vol. 40, pp. 87-91, 2014.

[6] S. T. Smith, S. C. Woody, and R. M. Seugling, "Closed loop control systems employing relaxor ferroelectric actuators," ed: Google Patents, 2004.

[7] A. Chynoweth, "Surface space-charge layers in barium titanate," *Physical Review,* vol. 102, p. 705, 1956.

[8] C. Government. (2012, 12 July). *Reduction of Carbon Dioxide Emissions from Coal-fired Generation of Electricity Regulations*. Available: http://laws-lois.justice.gc.ca/eng/regulations/SOR-2012-167/index.html

[9] U. Government. (2008, 12 July). *2010 to 2015 government policy: greenhouse gas emissions*. Available: https://www.gov.uk/government/publications/2010-to-2015-government-policy-greenhouse-gas-emissions/2010-to-2015-government-policy-greenhouse-gas-emissions#contents

[10] Chinadaily. (2004, 12 July). *China to adopt auto emission standard equal to Euro III in 2008*. Available: http://www.chinadaily.com.cn/english/doc/2004-07/07/content_346332.htm

[11] A. Shah, P. Torres, R. Tscharner, N. Wyrsch, and H. Keppner, "Photovoltaic technology: the case for thin-film solar cells," *science,* vol. 285, pp. 692-698, 1999.

[12] I. Grinberg, D. V. West, M. Torres, G. Gou, D. M. Stein, L. Wu*, et al.*, "Perovskite oxides for visible-light-absorbing ferroelectric and photovoltaic materials," *Nature,* vol. 503, pp. 509-12, Nov 28 2013.

[13] F. Zheng, Y. Xin, W. Huang, J. Zhang, X. Wang, M. Shen*, et al.*, "Above 1% efficiency of a ferroelectric solar cell based on the Pb (Zr, Ti) O 3 film," *Journal of Materials Chemistry A,* vol. 2, pp. 1363-1368, 2014.

[14] T. Zheng, H. Deng, W. Zhou, X. Zhai, H. Cao, L. Yu*, et al.*, "Bandgap modulation and magnetic switching in PbTiO3 ferroelectrics by transition elements doping," *Ceramics International,* vol. 42, pp. 6033-6038, 2016.

[15] S. Kumari, N. Ortega, A. Kumar, J. Scott, and R. Katiyar, "Ferroelectric and

photovoltaic properties of transition metal doped Pb (Zr0. 14Ti0. 56Ni0. 30) O3-δ thin films," *AIP Advances,* vol. 4, p. 037101, 2014.

[16] L. Pintilie, I. Vrejoiu, D. Hesse, G. LeRhun, and M. Alexe, "Ferroelectric polarization-leakage current relation in high quality epitaxial Pb (Zr, Ti) O 3 films," *Physical review B,* vol. 75, p. 104103, 2007.

[17] K. Uchino, Y. Miyazawa, and S. Nomura, "High-Voltage Photovoltaic Effect in PbTiO3-Based Ceramics," *Japanese Journal of Applied Physics,* vol. 21, p. 1671, 1982.

[18] V. Harshan and S. Kotru, "Influence of work-function of top electrodes on the photovoltaic characteristics of Pb0. 95La0. 05Zr0. 54Ti0. 46O3 thin film capacitors," *Applied Physics Letters,* vol. 100, p. 173901, 2012.

[19] J. Zhang, X. Su, M. Shen, Z. Dai, L. Zhang, X. He*, et al.*, "Enlarging photovoltaic effect: combination of classic photoelectric and ferroelectric photovoltaic effects," *Sci Rep,* vol. 3, p. 2109, 2013.

[20] U. Government. (2013, 13 July). *Waste Electrical and Electronic Equipment recycling (WEEE)*. Available: http://www.hse.gov.uk/waste/waste-electrical.htm

[21] S. L. T. Choi, * Y. J. Choi, V. Kiryukhin, S.-W. Cheong†, "Switchable ferroelectric diode and photovoltaic effect in BiFeO3," *Science,* vol. VOL 324, p. 63, 2009.

[22] S. Y. Yang, J. Seidel, S. J. Byrnes, P. Shafer, C. H. Yang, M. D. Rossell*, et al.*, "Above-bandgap voltages from ferroelectric photovoltaic devices," *Nat Nanotechnol,* vol. 5, pp. 143-7, Feb 2010.

[23] Y. Sun, X. Liu, J. Zeng, J. Yan, D. Shi, and H. Liu, "Photovoltaic effects in polarized polycrystalline BiFeO3 films," *Journal of Electronic Materials,* vol. 44, p. 4207, 2015.

[24] D. Wang, N. Chan, S. Li, S. Choy, H. Tian, and H. W. Chan, "Enhanced ferroelectric and piezoelectric properties in doped lead-free (Bi 0.5 Na 0.5) 0.94 Ba 0.06 TiO 3 thin films," *Applied Physics Letters,* vol. 97, p. 212901, 2010.

[25] M. Zeng, S. W. Or, and H. L. W. Chan, "First-principles study on the electronic and optical properties of Na 0.5 Bi 0.5 TiO 3 lead-free piezoelectric crystal," *Journal of applied physics,* vol. 107, p. 043513, 2010.

[26] M. Bousquet, J.-R. Duclère, E. Orhan, A. Boulle, C. Bachelet, and C. Champeaux, "Optical properties of an epitaxial Na 0.5 Bi 0.5 TiO 3 thin film grown by laser ablation: Experimental approach and density functional theory calculations," *Journal of Applied Physics,* vol. 107, p. 104107, 2010.

[27] E. Chernova, O. Pacherova, T. Kocourek, M. Jelinek, A. Dejneka, and M. Tyunina, "Optical Properties of Ferroelectric Epitaxial K0. 5Na0. 5NbO3 Films in Visible to Ultraviolet Range," *PloS one,* vol. 11, p. e0153261, 2016.

[28] K. Xu, J. Li, X. Lv, J. Wu, X. Zhang, D. Xiao*, et al.*, "Superior Piezoelectric Properties in Potassium–Sodium Niobate Lead-Free Ceramics," *Advanced Materials,* vol. 28, pp. 8519-8523, 2016.

[29] D. Damjanovic, "Ferroelectric, dielectric and piezoelectric properties of ferroelectric thin films and ceramics," *Reports on Progress in Physics,* vol. 61, p. 1267, 1998.

[30] N. A. Benedek and C. J. Fennie, "Why are there so few perovskite ferroelectrics?," *The Journal of Physical Chemistry C,* vol. 117, pp. 13339-13349,

2013.

[31] R. S. Roth, "Classification of perovskite and other ABO3-type compounds," *J. Res. Nat. Bur. Stand,* vol. 58, pp. 75-88, 1957.

[32] R. C. Smith, *Smart material systems: model development*: SIAM, 2005.

[33] R. E. Cohen, "Origin of ferroelectricity in perovskite oxides," *Nature,* vol. 358, pp. 136-138, 1992.

[34] T. Mitsui, I. Tatsuzaki, and E. Nakamura, *An introduction to the physics of ferroelectrics* vol. 1: Gordon & Breach Science Pub, 1976.

[35] C. B. Sawyer and C. Tower, "Rochelle salt as a dielectric," *Physical review,* vol. 35, p. 269, 1930.

[36] I. Chilibon and J. N. Marat-Mendes, "Ferroelectric ceramics by sol–gel methods and applications: a review," *Journal of sol-gel science and technology,* vol. 64, pp. 571-611, 2012.

[37] C. Bowen, H. Kim, P. Weaver, and S. Dunn, "Piezoelectric and ferroelectric materials and structures for energy harvesting applications," *Energy & Environmental Science,* vol. 7, pp. 25-44, 2014.

[38] G. Lippmann, "Principe de la conservation de l'électricité, ou second principe de la théorie des phénomènes électriques," *Journal de Physique Théorique et Appliquée,* vol. 10, pp. 381-394, 1881.

[39] W. Voigt, *Lehrbuch der kristallphysik (mit ausschluss der kristalloptik)*: Springer-Verlag, 2014.

[40] E. R. Caley and J. F. Richards, "Theophrastus on stones," 1956.

[41] W. Thomson, "II. On the thermoelastic, thermomagnetic, and pyroelectric properties of matter," *The London, Edinburgh, and Dublin Philosophical Magazine and Journal of Science,* vol. 5, pp. 4-27, 1878.

[42] W. Voigt, "Versuch zur Bestimmung des wahren specifischen electrischen Momentes eines Turmalins," *Annalen der Physik,* vol. 296, pp. 368-375, 1897.

[43] S. D. Brewster, *Observations on the pyro-electricity of minerals*: William Blackwood, 1824.

[44] P. Hersch and K. Zweibel, "Basic photovoltaic principles and methods," Solar Energy Research Inst., Golden, CO (USA)1982.

[45] A. Becquerel, "Mémoire sur les effets électriques produits sous l'influence des rayons solaires. Comptes Rendus 9: 561–567," *Originalarbeit zur Einwirkung von Licht auf Elektroden,* 1839.

[46] K. K. Chattopadhyay, *Introduction To Nanoscience And Nenotechnology*: PHI Learning Pvt. Ltd., 2009.

[47] D. Wolpert and P. Ampadu, "Temperature effects in semiconductors," in *Managing temperature effects in nanoscale adaptive systems*, ed: Springer, 2012, pp. 15-33.

[48] A. Sproul, "Understanding the pn Junction," *Solar Cells: Resources for the Secondary Science Teacher,* pp. 13-24, 2003.

[49] N. W. Ashcroft and N. D. Mermin, "Solid State Physics (Holt, Rinehart and Winston, New York, 1976)," *Google Scholar,* vol. 403, 2005.

[50] K. K. Ng, *Complete guide to semiconductor devices*: Wiley Online Library, 2002.

[51] S. M. Sze and K. K. Ng, *Physics of semiconductor devices*: John wiley & sons,

2006.

[52] R. Mehta, B. Silverman, and J. Jacobs, "Depolarization fields in thin ferroelectric films," *Journal of Applied Physics,* vol. 44, pp. 3379-3385, 1973.

[53] P. Wurfel and I. Batra, "Depolarization-field-induced instability in thin ferroelectric films—experiment and theory," *Physical Review B,* vol. 8, p. 5126, 1973.

[54] Y. Yuan, Z. Xiao, B. Yang, and J. Huang, "Arising applications of ferroelectric materials in photovoltaic devices," *Journal of Materials chemistry A,* vol. 2, pp. 6027-6041, 2014.

[55] W. Dong, Y. Guo, B. Guo, H. Liu, H. Li, and H. Liu, "Photovoltaic properties of BiFeO 3 thin film capacitors by using Al-doped zinc oxide as top electrode," *Materials Letters,* vol. 91, pp. 359-361, 2013.

[56] Z. Fan, K. Sun, and J. Wang, "Perovskites for photovoltaics: a combined review of organic–inorganic halide perovskites and ferroelectric oxide perovskites," *Journal of Materials Chemistry A,* vol. 3, pp. 18809-18828, 2015.

[57] V. Fridkin, "Bulk photovoltaic effect in noncentrosymmetric crystals," *Crystallography Reports,* vol. 46, pp. 654-658, 2001.

[58] A. Glass, D. Von der Linde, D. Auston, and T. Negran, "Excited state polarization, bulk photovoltaic effect and the photorefractive effect in electrically polarized media," *Journal of Electronic Materials,* vol. 4, pp. 915-943, 1975.

[59] V. M. Fridkin, *Photoferroelectrics* vol. 9: Springer Science & Business Media, 2012.

[60] J. Seidel, L. W. Martin, Q. He, Q. Zhan, Y. Chu, A. Rother*, et al.*, "Conduction at domain walls in oxide multiferroics," *Nature materials,* vol. 8, p. 229, 2009.

[61] J. Seidel, D. Fu, S.-Y. Yang, E. Alarcón-Lladó, J. Wu, R. Ramesh*, et al.*, "Efficient photovoltaic current generation at ferroelectric domain walls," *Physical review letters,* vol. 107, p. 126805, 2011.

[62] A. Bhatnagar, A. R. Chaudhuri, Y. H. Kim, D. Hesse, and M. Alexe, "Role of domain walls in the abnormal photovoltaic effect in BiFeO3," *Nature communications,* vol. 4, 2013.

[63] S. Nakashima, T. Uchida, D. Nakayama, H. Fujisawa, M. Kobune, and M. Shimizu, "Bulk photovoltaic effect in a BiFeO3 thin film on a SrTiO3 substrate," *Japanese Journal of Applied Physics,* vol. 53, p. 09PA16, 2014.

[64] M. Alexe and D. Hesse, "Tip-enhanced photovoltaic effects in bismuth ferrite," *Nature Communications,* vol. 2, p. 256, 2011.

[65] M. Alexe, "Local mapping of generation and recombination lifetime in BiFeO3 single crystals by scanning probe photoinduced transient spectroscopy," *Nano letters,* vol. 12, pp. 2193-2198, 2012.

[66] R. T. Tung and 董梓則, "The physics and chemistry of the Schottky barrier height," *Applied Physics Reviews,* vol. 1, p. 011304, 2014.

[67] M. Qin, K. Yao, and Y. C. Liang, "Photovoltaic characteristics in polycrystalline and epitaxial (Pb 0.97 La 0.03)(Zr 0.52 Ti 0.48) O 3 ferroelectric thin films sandwiched between different top and bottom electrodes," *Journal of applied physics,* vol. 105, p. 061624, 2009.

[68] J. Scott, "Device physics of ferroelectric thin-film memories," *Japanese journal*

of applied physics, vol. 38, p. 2272, 1999.

[69] A. Dhar and A. Mansingh, "Optical properties of reduced lithium niobate single crystals," *Journal of applied physics,* vol. 68, pp. 5804-5809, 1990.

[70] S. Wemple, "Polarization Fluctuations and the Optical-Absorption Edge in BaTi O 3," *Physical Review B,* vol. 2, p. 2679, 1970.

[71] S. Rühle, "Tabulated values of the Shockley–Queisser limit for single junction solar cells," *Solar Energy,* vol. 130, pp. 139-147, 2016.

[72] R. Nechache, C. Harnagea, S. Li, L. Cardenas, W. Huang, J. Chakrabartty, *et al.*, "Bandgap tuning of multiferroic oxide solar cells," *Nature Photonics,* vol. 9, pp. 61-67, 2015.

[73] M. Qin, K. Yao, and Y. C. Liang, "Photovoltaic mechanisms in ferroelectric thin films with the effects of the electrodes and interfaces," *Applied Physics Letters,* vol. 95, p. 022912, 2009.

[74] L. Wang, H. Ma, L. Chang, C. Ma, G. Yuan, J. Wang, *et al.*, "Ferroelectric BiFeO3 as an Oxide Dye in Highly Tunable Mesoporous All-Oxide Photovoltaic Heterojunctions," *Small,* vol. 13, 2017.

[75] M. Wu, X. Lou, T. Li, J. Li, S. Wang, W. Li, *et al.*, "Ni-doped SrBi2Nb2O9–Perovskite oxides with reduced band gap and stable ferroelectricity for photovoltaic applications," *Journal of Alloys and Compounds,* vol. 724, pp. 1093-1100, 2017.

[76] H. Han, D. Kim, K. Chu, J. Park, S. Y. Nam, S. Heo, *et al.*, "Enhanced Switchable Ferroelectric Photovoltaic Effects in Hexagonal Ferrite Thin Films via Strain Engineering," *ACS applied materials & interfaces,* vol. 10, pp. 1846-1853, 2018.

[77] J. Chakrabartty, C. Harnagea, M. Celikin, F. Rosei, and R. Nechache, "Improved photovoltaic performance from inorganic perovskite oxide thin films with mixed crystal phases," *Nature Photonics,* p. 1, 2018.

[78] L. Egerton and D. M. Dillon, "Piezoelectric and dielectric properties of ceramics in the system potassium—sodium niobate," *Journal of the American Ceramic Society,* vol. 42, pp. 438-442, 1959.

[79] C.-W. Ahn, H.-C. Song, S. Nahm, S.-H. Park, K. Uchino, S. Priya, *et al.*, "Effect of MnO2 on the piezoelectric properties of (1-x)(Na0. 5K0. 5) NbO3–xBaTiO3 ceramics," *Japanese journal of applied physics,* vol. 44, p. L1361, 2005.

[80] D. Lin, K. W. Kwok, H. Tian, and H. W. L. w. Chan, "Phase Transitions and Electrical Properties of (Na1− xKx)(Nb1− ySby) O3 Lead-Free Piezoelectric Ceramics With a MnO2 Sintering Aid," *Journal of the American Ceramic Society,* vol. 90, pp. 1458-1462, 2007.

[81] D. Lin, K. Kwok, and H. Chan, "Piezoelectric and ferroelectric properties of K x Na 1− x NbO 3 lead-free ceramics with MnO 2 and CuO doping," *Journal of alloys and compounds,* vol. 461, pp. 273-278, 2008.

[82] O. Johari and A. Samudra, "Scanning electron microscopy," in *Characterization of Solid Surfaces*, ed: Springer, 1974, pp. 107-131.

[83] S. C. Das, A. Shahee, N. Lalla, and T. Shripathi, "A simple and low cost Sawyer-Tower ferro-electric loop tracer with variable frequency and compensation circuit," in *Proceedings of the 54th DAE Solid State Physics Symposium Volume*, 2009, pp. 439-440.

[84] J. Tauc, "Optical properties and electronic structure of amorphous Ge and Si," *Materials Research Bulletin,* vol. 3, pp. 37-46, 1968.

[85] J. R. Bakke, J. T. Tanskanen, H. J. Jung, R. Sinclair, and S. F. Bent, "Atomic layer deposition of Cd x Zn 1− x S films," *Journal of Materials Chemistry,* vol. 21, pp. 743-751, 2011.

[86] G. Li, L. Zheng, Q. Yin, B. Jiang, and W. Cao, "Microstructure and ferroelectric properties of Mn O 2-doped bismuth-layer (Ca, Sr) Bi 4 Ti 4 O 15 ceramics," *Journal of applied physics,* vol. 98, p. 064108, 2005.

[87] J. Rani, P. K. Patel, N. Adhlakha, H. Singh, K. Yadav, and S. Prakash, "Mo 6+ Modified (K 0.5 Na 0.5) NbO 3 Lead Free Ceramics: Structural, Electrical and Optical Properties," *Journal of Materials Science & Technology,* vol. 30, pp. 459-465, 2014.

[88] E. J. Little Jr and M. M. Jones, "A complete table of electronegativities," *Journal of Chemical Education,* vol. 37, p. 231, 1960.

[89] R. López and R. Gómez, "Band-gap energy estimation from diffuse reflectance measurements on sol–gel and commercial TiO2: a comparative study," *Journal of sol-gel science and technology,* vol. 61, pp. 1-7, 2012.

[90] SHIADZU. (30th April 2018). *ABC's of the Diffuse Reflection Method*. Available: https://www.shimadzu.com/an/ftir/support/ftirtalk/talk1/intro.html

[91] J. Park, S. S. Won, C. W. Ahn, and I. W. Kim, "Ferroelectric Photocurrent Effect in Polycrystalline Lead-Free (K0. 5Na0. 5)(Mn0. 005Nb0. 995) O3 Thin Film," *Journal of the American Ceramic Society,* vol. 96, pp. 146-150, 2013.

[92] I. Izzuddin, M. H. H. Jumali, and Z. Zainuddin, "Structural and electrical evaluation of KNN ceramic," in *AIP Conference Proceedings*, 2014, pp. 90-93.

[93] W. Ji, K. Yao, and Y. C. Liang, "Evidence of bulk photovoltaic effect and large tensor coefficient in ferroelectric BiFeO 3 thin films," *Physical Review B,* vol. 84, p. 094115, 2011.

[94] Z. Wang, R. Yu, C. Pan, Z. Li, J. Yang, F. Yi*, et al.*, "Light-induced pyroelectric effect as an effective approach for ultrafast ultraviolet nanosensing," *Nat Commun,* vol. 6, p. 8401, Sep 25 2015.

[95] J. Park, C. Won Ahn, and I. Won Kim, "Photocurrent of lead-free (K0. 5Na0. 5)(Mn0. 005Nb0. 995) O3 ferroelectric nanotubes," *Journal of Applied Physics,* vol. 112, p. 014312, 2012.

[96] L. Chen, B. Luo, N. Chan, J. Dai, M. Hoffman, S. Li*, et al.*, "Enhancement of photovoltaic properties with Nb modified (Bi, Na) TiO3–BaTiO3 ferroelectric ceramics," *Journal of alloys and compounds,* vol. 587, pp. 339-343, 2014.

[97] W. S. Woo, S. S. Won, C. W. Ahn, S. A. Chae, A. Ullah, and W. Kim, "Photovoltaic effect of lead-free (Na0. 82K0. 18) 0.5 Bi4. 5Ti4O15 ferroelectric thin film using Pt and indium tin oxide top electrodes," *J. Appl. Phys,* vol. 115, 2014.